
The Role of Four-Quark States in the Nature of Exotic Hadrons from Bethe-Salpeter Equations

DISSERTATION

zur Erlangung des Doktorgrades der Naturwissenschaften

Dr. rer. nat.

NICO GIDEON SANTOWSKY^{1,2}

Institut für Theoretische Physik
Justus-Liebig-Universität Gießen
Juli 2021

Erstgutachter: Prof. Dr. Christian S. Fischer
Zweitgutachter: Prof. Dr. Marc Wagner

Abstract

In this work we use the framework of Dyson-Schwinger and Bethe-Salpeter equations (DSEs and BSEs) to describe candidates of exotic hadrons in a four-quark (tetraquark) picture. Specifically, we calculate mass spectra on the energy levels of light scalar mesons, ordinary charmonia and fully-charmed tetraquark states. For that, we solve the quark DSE and several two-quark meson and diquark BSEs for different quark masses and quantum numbers in order to use the corresponding propagators and bound state amplitudes for a description of tetraquarks in a reduced two-body approximation of the full four-body BSE that is able to distinguish between different internal structures. Beyond that, we introduce a novel method to couple the two-body tetraquark BSE with the two-quark meson BSE in order to be able to describe mixing effects of tetraquark components with ordinary quarkonia.

In the energy region of ordinary charmonia, we observe that the candidates of the $\chi_{c1}(3872)$ and $Z_c(3900)$ are both dominated by a mesonic $D\bar{D}^*$ component, whereas the diquark-antidiquark and the hadro-charmonium component are negligible for the description of those states. The same mostly holds for other hidden and open charm heavy-light ground states. A mixing with ordinary quarkonia was not considered in those channels for technical reasons. Moreover, we observe that the light scalar mesons $f_0(500)$ and $a_0/f_0(980)$ are dominated by meson-meson correlations ($\pi\pi$ and $K\bar{K}$) as well, whereas the diquark-antidiquark and even the $q\bar{q}$ components appear to be irrelevant for a description of the ground states. We further show that this is an effect of chiral symmetry breaking as this four-quark dominance is only present for light quark masses. In course of all-charm calculations we are able to extract a whole spectrum for quantum numbers 0^+ and 1^+ , where we find possible candidates for the recently discovered $X(6900)$ in the excitation spectra for both quantum numbers. The 1^+ candidates are pure mesonic composite states, whereas the 0^+ candidates also have a non-negligible diquark-antidiquark component.

Kurzzusammenfassung

In dieser Arbeit nutzen wir Dyson-Schwinger- und Bethe-Salpeter-Gleichungen (DSEs und BSEs), um Kandidaten für exotische Hadronen in einem Vier-Quark/Tetraquark-Bild zu beschreiben. Im Speziellen berechnen wir Massenspektren auf den Energieniveaus von leichten Mesonen, gewöhnlichen Charmonia und Full-Charm-Tetraquarks. Dafür lösen wir die Quark-DSE und mehrere Zwei-Quark-BSEs für verschiedene Quarkmassen und Quantenzahlen, um mit den entsprechenden Propagatoren und Bindungszustandsamplituden Vier-Quark-Zustände in einer reduzierten Zweikörperapproximation der vollen Vierkörpergleichung zu beschreiben. Darüber hinaus führen wir eine neuartige Methode zur Kopplung der Zweikörper-Tetraquark-BSE mit der Zwei-Quark-Meson-BSE ein, um Mischungseffekte von Tetraquarks mit gewöhnlichen Quarkonia zu beschreiben. Im Energiebereich gewöhnlicher Charmonia sehen wir, dass die Kandidaten des $\chi_{c1}(3872)$ und des $Z_c(3900)$ beide von der mesonischen DD^* -Komponente dominiert sind, während die Diquark-Antidiquark- und Hadro-Charmonium-Komponenten vernachlässigbar für eine Beschreibung dieser Zustände sind. Zumeist gilt dies auch für andere Heavy-Light-Grundzustände sowohl mit Hidden-, als auch mit Open-Charm-Quantenzahlen. Eine Mischung mit gewöhnlichen Quarkonia wurde in diesen Kanälen aus technischen Gründen nicht berücksichtigt. Außerdem beobachten wir, dass die leichten, skalaren Mesonen $f_0(500)$ und $a_0/f_0(980)$ ebenfalls von Meson-Meson-Korrelationen ($\pi\pi$ und $K\bar{K}$) dominiert werden, während die Diquark-Antiquark- und sogar die $q\bar{q}$ -Komponente für die Beschreibung der Grundzustände irrelevant zu sein scheinen. Wir zeigen weiter, dass die $\pi\pi$ -Dominanz für das $f_0(500)$ auf chirale Effekte rückführbar ist, da diese lediglich bei leichten Quarks präsent ist. Im Zuge von All-Charm-Rechnungen können wir ein ganzes Spektrum für die Quantenzahlen 0^+ und 1^+ extrahieren und finden mögliche Kandidaten für das erst kürzlich entdeckte $X(6900)$ in den Anregungsspektren beider Quantenzahlen. Während die 1^+ -Kandidaten rein mesonische Zustände sind, haben die 0^+ -Kandidaten nicht-vernachlässigbare Diquark-Antidiquark-Komponenten.

TABLE OF CONTENTS

1	Introduction	9
1.1	Elementary Particle Physics	9
1.2	Quarks and Multiquark States	10
1.3	Motivation	11
1.4	Theory and Experiment	15
1.5	Theoretical Status on Exotic Four-Quark Candidates	19
1.6	Goal of this Work & Outline	20
2	The Dyson-Schwinger Framework	21
2.1	Functional Derivation from QCD	21
2.2	The Quark Dyson-Schwinger Equation	25
2.2.1	The Equation	26
2.2.2	The Need for Truncations	27
2.2.3	Effective Gluon	27
2.2.4	Charge Conjugation	29
2.2.5	Singularities and Branch Cuts	30
2.2.6	Solution	31
3	Bethe-Salpeter Equations	34
3.1	Derivation	34
3.2	The Two-Quark BSE	37
3.3	Truncations	38
3.4	Quantum Numbers	39
3.4.1	(Pseudo-)Scalar $q\bar{q}$ Mesons	39
3.4.2	(Axial-)Vector $q\bar{q}$ Mesons	42
3.5	Normalization and Decay Constants	42
3.6	Diquarks	46
3.7	Two-Quark Properties in the Maris-Tandy Model	48
3.7.1	Full Basis	48
3.7.2	Truncated Basis	48
3.7.3	Dynamic Interaction Model	50
3.8	Pole Restrictions	52
3.9	Heavy(-Light) Mesons and Diquarks	54
3.10	Bethe-Salpeter Amplitudes in the Complex Plane	56
3.11	Meson and Diquark Propagators	57

3.12	Off-shell Meson and Diquark Amplitudes	59
4	Tetraquarks	60
4.1	The Two-Body Equation	61
4.2	Quantum Numbers	66
4.3	Amplitude Construction	67
4.4	Poles and Thresholds	71
4.5	Quarkonium Mixing	72
4.6	Resonances and the Complex Q^2 Plane	75
5	Results	80
5.1	Pure Heavy-Light Tetraquarks	80
5.1.1	Hidden Charm	80
5.1.2	Open Charm	84
5.1.3	Comparison between Hidden- and Open-Charm Candidates	86
5.2	Quarkonium Mixing in the Light Quark Sector	87
5.2.1	Real Momenta	87
5.2.2	Complex Momenta	90
5.3	All-Charm Four-Quark Resonances	100
6	Conclusion and Outlook	104
A	Conventions	108
B	Solving the Quark DSE	111
B.1	Solving on the Real Axis	111
B.2	Continuation into the Complex Plane: The “Shell Method”	113
C	BSEs	115
C.1	Two-Quark Case	115
C.1.1	Index Structure of a Two-Quark BSE	115
C.1.2	Flavour- and Colour-Space Conventions	116
C.1.3	Solving the Two-Quark BSE in Maris-Tandy Interaction	117
C.2	Four-Quark Case	122
C.2.1	Precalculations	122
C.2.2	Structure	124
C.2.3	Complications	125
D	Numerical Toolkit	127
E	Technical Tools	132
	Bibliography	133
	Acknowledgements	142

CHAPTER 1

INTRODUCTION

1.1 Elementary Particle Physics

The search for the tiniest structures and the associated mechanisms in nature has a long history. Nowadays, we believe that there exist four fundamental forces which are responsible for the phenomena we observe in our universe:

- electromagnetism: the force between electrically charged particles such as electrons and protons in an atom. In principle, it's acting on arbitrarily long distances, but its strength is decreasing quickly with increasing distance.
- weak interaction: it's responsible e.g. for nuclear decays. The radius of action is extremely small – only on subatomic scales, this interaction can be observed.
- strong interaction: it's binding together atomic nuclei, generates the majority of mass in our universe and acts only on subatomic scales. With increasing distance, this force is not asymptotically approaching zero strength as it is the case for the electromagnetic interaction, but rather approaches a non-zero value. In its radius of action, it is more than 100 times stronger than the electromagnetic force.
- gravitation: this force is by far the weakest, but the most influential force in the universe. It cannot be shielded and is responsible for planetary and stellar trajectories. The radius of action is infinitely large such that this force dominates the behaviour of the largest structures we have knowledge about; for example, the orbit of our solar system in the Milky Way is influenced by forces acting over thousands of light years.

The first three forces are described by the so-called Standard Model of elementary particle physics. Attractions and repulsions between interacting particles are described via the exchange of bosonic particles, called exchange bosons. It is broadly desired that the behaviour of particles is mathematically described by well-formulated quantum field theories. The electromagnetic interaction for instance is described by a quantum field theory called quantum electrodynamics (QED) and can be generalized together with the weak interaction to the theory of electroweak interaction. While the small coupling of the electromagnetic force allows us to treat QED as a perturbation theory, it can be solved that

way as it is. That makes a vital difference to the treatment of strong interaction, which is described by quantum chromodynamics (QCD) and cannot be treated as a perturbation theory at low energies (or large distances, respectively) due to its strong coupling. Until this day, QCD cannot be considered as solved; while trying, theoretical physicists all over the world are faced with enormous technical and conceptual challenges. This does not hold for the behaviour on small distances (or high energies, respectively), where the coupling is approaching zero and the theory could be solved perturbatively (“asymptotic freedom”).

The fourth force, gravitation, is not part of the standard model and the formulation of a robust quantum theory is still a subject of intense research. On large scales, phenomena are successfully described by general relativity, but the behaviour on small distances is still puzzling because there is no clear perspective to extract information from experiment due to its weak strength compared to the other forces, which clearly dominate physics on small scales. Theorists all over the world search for generalizing “beyond-standard-model” (BSM) theories in the field of quantum gravity. However, it is yet unknown, on which energy scale the relevant effects of BSM physics could be measured. At some point in time, the development of a proper theory for quantum gravity could lead to a more general description of the unsolved mysteries in our universe such as dark matter or dark energy.

1.2 Quarks and Multiquark States

In this thesis, we focus on the strong interaction/QCD and the production of bound states and resonances. While the electromagnetic force describes interactions between particles with electric charge, the interacting particles in QCD carry a “strong” charge, which we characterize by three colours (and the corresponding anticolours). Based on this, QCD is a non-Abelian gauge theory with $SU(3)$ as the associated symmetry group. The colour-carrying fermions in this theory are quarks and the exchange bosons are gluons, which carry a colour charge as well. To this day, we know about six sorts of quarks (and their antiparticles) and distinguish between them by a property called flavour. Only composite states of colour-carrying particles for which the colours “add up” to zero – a “colourless” or “white” state, which we call hadron – could be observed in nature. The potential energy resulting from separating a quark from a colourless state results in quark-antiquark productions, ensuring colourless separations. This principle is called “confinement” and is fundamental for our understanding of the strong interaction. It leads to bound state spectra including quarks and gluons, but only in specific configurations. The simplest ones are mesons, compositions of a quark and an antiquark ($q\bar{q}$) and baryons, compositions of three quarks (qqq) or three antiquarks, respectively. Prominent representatives for the latter configurations are protons and neutrons, the building blocks of atomic nuclei. Though, these are not the only ones; one can imagine of other compositions, which we call exotic:

- tetraquarks: bosonic particles containing two quarks and two antiquarks ($qq\bar{q}\bar{q}$)
- hybrids: bosonic particles containing a quark, an antiquark and a gluon ($q\bar{q}g$)

- glueballs: bosonic particles containing two or more gluons ($gg[g]$)
- and even higher multiquark states (fermionic pentaquarks, hexaquarks, ...)

The attribute “exotic” originally stems from the non-explainability of certain quantum numbers from the non-relativistic quark model of conventional $q\bar{q}$ mesons – thus, either the inclusion of relativistic effects or the consideration of deviating “exotic” compositions provide the possibility to realize an appropriate description of those states. In principle, there is no upper limit set for the own imagination regarding the construction of exotic states, but since a physical system always aspires a state of minimal energy, the hadronic reality should be dominated by low-energy states.

It is conceivable to consider also coloured particles such as diquarks – states with two quarks (qq) or two antiquarks, respectively – as particles which occur only internally in higher bound states or resonances. Although they may have this “building block character”, they have to be understood more as auxiliary tools than as standalone bound states due to the lacking observability. An extensive overview over multiquark states from a theoretical and an experimental view is provided by the review articles [1, 2].

In this thesis, we investigate the properties of colourless two- and four quark states – mesons and tetraquarks¹. The principles of quantum mechanics allow us to overlap the wave functions of different states as long as they have the same quantum numbers and thus, the full wave function of a hadronic state could potentially be a sum of wave functions including different structures. In that sense, a bosonic hadron may have non-vanishing meson *and* tetraquark components if the quantum numbers allow, and even the tetraquark component might be decomposable into different substructures. Additional hybrid and glueball components for instance are possible as well, but we will particularly concentrate on mesons and tetraquarks in this work.

1.3 Motivation

The light scalars. The lowest-lying state consisting of two light quarks (u/d) is the pion with quantum numbers 0^- : a pseudoscalar. It is the pseudo Goldstone boson of QCD as a consequence of spontaneous chiral symmetry breaking. Hence, according to the Goldstone theorem [3], it would be massless if chiral symmetry was not explicitly broken (which would be the case for vanishing quark masses). The chiral partner of the pion with opposite parity, i.e. with quantum numbers 0^+ , is called σ or $f_0(500)$ and has a puzzling property: its mass. With 400 – 550 MeV, it is far lighter than predicted by the quark model. Especially, it should be heavier than the vector (1^-) partner, which we can trace back to group theoretical aspects: non-relativistically, the relation $P = (-1)^{L+1}$ holds and we conclude that the 0^+ ground state is a p -wave ($L = 1$). That however indicates a contribution from angular momentum that should raise the mass above its 1^- partner, the ρ , which is an s -wave in the non-relativistic picture. But since $m_\rho > m_\sigma$, we get what we call *inverse mass ordering*. Considering the whole multiplet of scalar states, which is

¹As bosonic hadrons, tetraquarks are often called mesons as well in literature, mostly with the attribute “exotic”. For the sake of understandability, we will call $(q\bar{q})$ states mesons and $(qq\bar{q}\bar{q})$ states tetraquarks throughout this work.

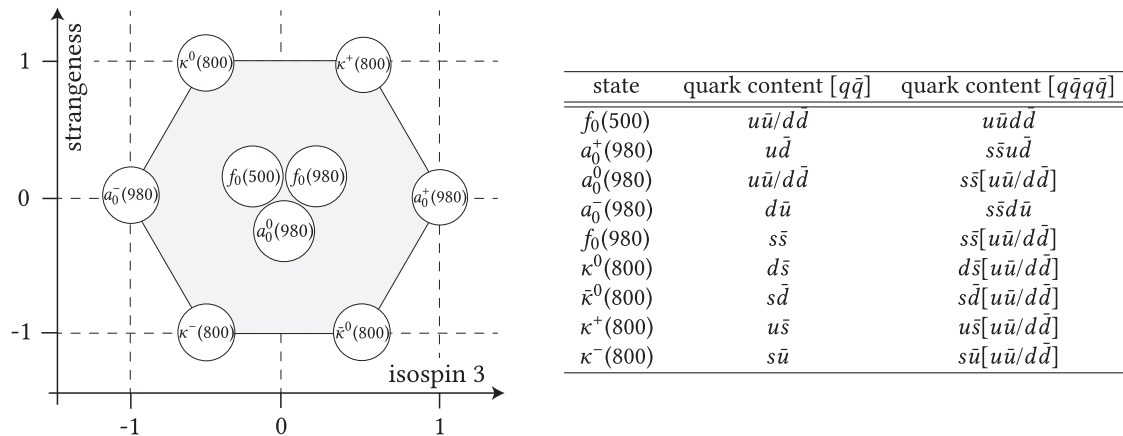


Figure 1.1: *Left panel:* The scalar meson ground state multiplet its typical graphical form. f_0 states are isoscalars ($I = 0$) and a_0 states are isovectors ($I = 1$). *Right panel:* All states from the multiplet put into a table with their respective quark content in a $q\bar{q}$ description and in a $qq\bar{q}\bar{q}$ description.

shown in Fig. 1.1, we notice further inconsistencies with a $q\bar{q}$ interpretation if we take a closer look at the hidden-strange states. In the $q\bar{q}$ interpretation, the lightest isoscalar $f_0(500)$ should be almost mass-degenerate with the three $a_0(980)$ states in the isotriplet due to the light quark content and the (approximate) isospin symmetry, whereas the second lightest isoscalar, the $f_0(980)$, should be much heavier as it would consist of two strange quarks. But the numbers in parentheses entail that this is not what we find in nature: contrary, the $a_0(980)$ states and the second-lightest $f_0(980)$ are almost mass-degenerate mysteriously, whereas the $f_0(500)$ is by far the lightest state. These arguments lead to the conclusion that a $q\bar{q}$ description may not be the correct way of describing this multiplet.

All these putative inconsistencies could be resolved by taking two more quarks into consideration and thus, describing the light scalars four-quark states with quark content $qq\bar{q}\bar{q}$. Recalling the parity argument from non-relativistic quark models, it now states $P = (-1)^L$ and we get a 0^+ ground state for vanishing angular momentum $L = 0$, which resolves the existence of a scalar state in the spectrum below the vector mesons. Furthermore, the mass-degeneracy between the $a_0(980)$ and the $f_0(980)$ could naturally be explained by the quark content alone: as the $f_0(500)$ only carries light quarks, the $f_0(980)$ and the $a_0(980)$ carry a heavy strange-antistrange quark pair. All this could be seen in the table on the right hand side of Fig. 1.1. This idea of describing the lightest scalars as four-quark states was firstly motivated by Jaffe in the 70s [4].

In addition to that, we could explain the low mass of the $f_0(500)$ when we consider pions as effective degrees of freedom. Compared to a constituent quark model with effective quark masses of ~ 350 MeV, it might be energetically favourable to bind two pions of $m_\pi \approx 140$ MeV together than two constituent quarks. Similarly, the $f_0/a_0(980)$ might be built-up molecularly by $K\bar{K}$ [5]. These arguments provide strong reasons to examine the nature of the light scalars with a dynamic quark content. Note that a few of these arguments are not exactly transferable to QCD, which is formulated relativistically so that $P = (-1)^{L+1}$ is not true any more for pure $q\bar{q}$ states, and since the lightest quarks in mesons should definitely not be considered as non-relativistic particles, we cannot

make reliable, quantitative statements on this level. Because of that, we will pursue an investigation in a covariant framework in this work.

The charmonium spectrum. Until 2003, charmonium spectroscopy was truly satisfying. Experiments were able to confirm many predictions of quark model calculations for charmonium states and the $q\bar{q}$ picture seemed to be a complete description, but the discovery of the $\chi_{c1}(3872)$ by the Belle Collaboration [6] was the birth of what we call exotic spectroscopy today: it has quantum numbers 1^{++} and does not fit into the quark model of ordinary charmonia. The low width and the closeness to the DD^* threshold indicates a four-quark structure with two charm and two light quarks. In the following years, parallel to novel theoretical predictions, more of those exotic states were measured. Traditionally¹, we classify these states with the letters X, Y and Z:

- Z for a state with non-zero electric charge,
- Y for 1^- states and
- X for the rest.

The charmonium-like exotic states along with the ordinary charmonia are embedded in the charmonium spectrum, which is shown in Fig. 1.2. Refs. [2, 8–11] together give a nice overview about all the different four-quark candidates and their properties.

With the discovery of charged Z states, any doubts on the existence of composite states with a content of at least four quarks were eliminated due to the fundamental principle of electrical charge conservation. Over the years, the internal structures of many XYZ states have been continuously discussed, and yet, there are no final agreements between different theoretical and experimental approaches. PANDA will be a promising experiment in order to measure line shapes – these will provide useful information to make experimentally founded statements about the inner structure [12]. In the paragraph after next we will briefly summarize which models are proposed in order to describe the inner structure of exotic tetraquark candidates.

All-charm tetraquark candidates. In 2020, the discovery of a state with a mass at around 6.9 GeV in the di- J/ψ mass spectrum was the first experimental evidence of a four-quark state with a quark configuration of $c\bar{c}c\bar{c}$ [13]. Due to its mass and the yet unknown quantum numbers it received the name X(6900). Different from X states in the charmonium region it is pretty unquestionable that this state is definitely a four-quark state due to its energy which is far away from the ones we expect from conventional $q\bar{q}$ states. The discovery of the X(6900) is very young and only little information is available yet, which makes it an attractive candidate to investigate theoretically. Such investigations could e.g. predict the quantum numbers or whether this state is a ground state or an excited one. Such a determination could be helpful in understanding how physics on this energy level works and might give hints about possible other, yet unobserved states.

¹Although this scheme has been abandoned by the PDG a few years ago, it is worth to name the traditional one here as it is still the one the majority of people is familiar with. The new scheme distinguishes between isospin, flavour and quantum numbers P and C ; an overview is provided e.g. in Ref. [7]. In this thesis, we will consistently stick to the new one when talking about experimentally confirmed states.

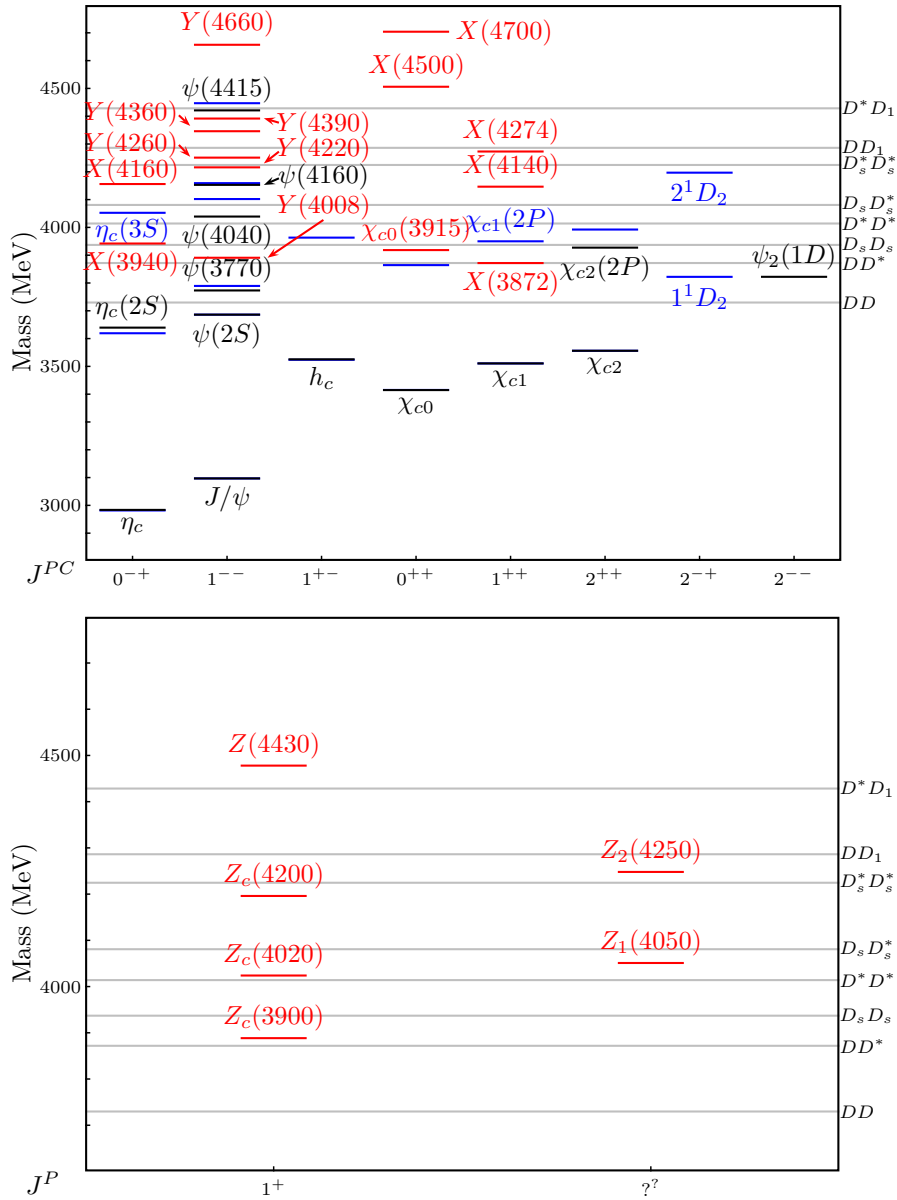


Figure 1.2: The charmonium spectrum. Black bars denote observed charmonium states; blue bars are predicted from quark model, but not yet unobserved states; red bars are exotic XYZ states. We distinguish between uncharged states (left panel) and charged states (right panel) because the latter ones are no eigenstates of the charge conjugation operator, in contrast to the former one. The spectra as shown are taken from [2].

Inner structure. Besides ordinary quarkonia, we distinguish between four four-quark structures. We will assume a heavy-light structure with quark content $Q\bar{Q}q\bar{q}$ for the following definitions as it provides the most general distinction for the states of interest in this work:

1. heavy-light meson-meson: Two mesons constitute a composite state with quark content $[Q\bar{q}][\bar{Q}q]$. States like this could be either bound or resonant. If the binding energy of such a bound state is small (\Leftrightarrow has a mass closely below the two-meson threshold), we talk about a meson molecule. For an overview about the nature of these kinds of states, see [1, 9, 14, 15].
2. hadro-quarkonium: This classification is meaningful only for heavy-light $Q\bar{Q}q\bar{q}$ states. The light $q\bar{q}$ state is surrounding the heavy $Q\bar{Q}$ similar to an electron which surrounds a proton with quark content $[Q\bar{Q}][q\bar{q}]$. If there are four quarks of equal mass, this configuration is equal to the meson-meson one (see the latter bullet). A discussion about the importance of this structure in the charmonium spectrum is provided by [16].
3. diquark-antidiquark: a diquark (Qq) and an antidiquark ($\bar{Q}\bar{q}$) are tightly bound and form a compact four-quark state, see [17] for an elucidation of the potential importance of this kind of structure. Often, this configuration is generally referred as *tetraquark* to differentiate the other two configurations from this one. In this thesis however, we will call every 4-quark composite state a tetraquark.
4. compact tetraquark: the four quarks are closely arranged with no assignable order.

These namings correspond to very common nomenclature in literature, so we will use them throughout this thesis consistently. In this work we will not consider the last configuration (4); we will later see why. A comprehensive overview over the whole topic is given by the review [18].

Theoretical perspective. The strength of theoretical calculations is to be able to vary parameters such as the quark mass or the coupling systematically. Treating hadronic states, there are many possible approaches, and comparisons between the different methods are a promising tool in order to confirm or disconfirm different results. However, as stressed before, there is still no final agreement between different approaches for many experimentally observed states. Nevertheless, findings in one approach could lead to enhanced efforts in other ones, and compliant findings could give hints for experimentalists to search for states in specific energy regions. Altogether, this makes theoretical calculations a powerful, yet reviewable tool in order to acquire knowledge.

1.4 Theory and Experiment

Gaining knowledge about the structure of hadronic matter is the central research emphasis of experimental and theoretical hadron physics. The development of theories and the search for experimental evidence are subject of nowadays research and a full understanding of the hadronic reality can only happen in an effective interplay between those

two disciplines. While experimentalists are planning experiments at particle accelerators and performing analyses of the extracted data in the first place, the task of theorists is to develop models and refine theories not only to reproduce the data that experimentalists already extracted from measurements at detectors, but also to do predictions which can be verified or rejected later on. Also, theoretical considerations may suggest, at which energy scales experimentalists should particularly look when searching e.g. for multi-quark states such as tetraquarks.

Theoretical approaches

In the following, selected theoretical approaches to deal with hadronic bound states and resonances are described. It should only serve as a short and non-technical overview – a more detailed summary of many approaches is given by [7, 19]; furthermore, we will refer on numerous review articles.

Quark Models. Quark model calculations mostly treat the fermions of strong interaction, the quarks, as constituent quarks with an effective mass i.e. to solve the Schrödinger equation based on spin-spin interactions. While this does not include phenomena like dynamical chiral symmetry breaking and pair creation/annihilation (some of the associated effects such as dynamical mass are stored in model parameters like the constituent quark mass), it is a comparably simple approach, which proved to be a good phenomenological tool to reproduce and predict many of the states in hadronic spectra on the basis of group theoretical aspects. The strength is especially the treatment of heavy quarks, where a non-relativistic approach is reasonable. By construction, quark models are limited and it is not possible to deal with certain exotic states such as glueballs and hybrids unless one extends the model by “constituent gluons” [20]. However, in principle, tetraquark calculations are possible, e.g. by choosing diquarks and antidiquarks as effective degrees of freedom as the authors did e.g. in [21–23] on the basis of the well-known $\chi_{c1}(3872)$.

Lattice QCD. The treatment of QCD on a lattice is one of the most widespread approaches to perform non-perturbative computations in QCD, for reviews cf. [24–26]. The idea is to introduce a minimal distance a as a regularization to discretize the spacetime on a lattice of finite volume. Spacetime integrals are substituted with sums over lattice sites. As a approaches zero (“continuum limit”), the original theory is restored. It is advantageous that conceptually, this approach yields well-determined statistical errors, which depend e.g. on the lattice spacing and the finite volume. Computations are done from first principles since correlation functions are directly extracted from Path integrals via Monte-Carlo methods. While this sounds promising, it turns out to be extremely difficult to overcome technical complexities. Auspicious progress in describing exotic four-quark candidates was made within the last decade [27–37]. In a gauge fixed formalism, correlation functions represent an important interface between the lattice approach and functional methods such as Dyson-Schwinger equations, which are briefly described in the following.

Dyson-Schwinger Equations. The Dyson-Schwinger framework is a functional approach based on the equations of motion for the one-particle irreducible Green's functions from QCD's effective action, for reviews cf. [38–42]. The Dyson-Schwinger equations (DSEs) of different Green's functions are coupled and include the full dynamics of QCD as an infinite tower of integral equations. In practice, solutions are either obtained via an iterative solution of the coupled system of self-consistent DSEs by using suitable truncations or via effective models. In combination with the formalism of Bethe-Salpeter equations (BSEs), which can be derived from the full $2n$ -quark Green's function and thus, from the effective action as well, DSEs have proven to be powerful tools to extract information about bound states, resonances [43–45] and even exotica [46–48]. A major weakness of this approach are uncertainties in the error estimate of the applied truncations and models.

Effective Field Theories. Effective field theories play an important role for the understanding of how exotic states are generated and constitute a tool which substitutes the dependence on the strong coupling at low energies with weakly interacting hadrons. In the low energy sector, it is possible to form an effective chiral Lagrangian which depends not on fundamental quark fields, but rather on the fields of QCD's lowest-lying colour singlet hadrons, e.g. the Goldstone bosons. This leads to the idea of chiral perturbation theory (ChPT), see [49] for a pedagogical introduction. Such theories in an interplay e.g. with lattice results provide a suitable tool to calculate observables from first principles [50]. Furthermore, it serves as an input for model-independent studies about the inner structure of candidates for hadronic molecules based on Weinberg's compositeness criterion [51, 52]. Also based on chiral effective Lagrangians, many features of QCD could be understood by studying the large- N_c limit of QCD [53–55]. In the low-energy region, leading-order large- N_c descriptions from chiral Lagrangians [56–59] and linear sigma models [60, 61] serve as strong tools to disentangle the nature of the light scalar mesons, which are doubtlessly not conventional $q\bar{q}$ states [62].

QCD Sum Rules. Apart from the approaches given above, it is worth to mention that exotic states could also be described by QCD Sum Rules [63, 64] – a method where masses, widths and decay constants are extracted by the computation of correlation functions from fundamental degrees of freedom *and* from mesonic ones. This method works under the assumption that in a certain energy region the two calculations give the same result [2]. In the last decade, the applicability of this approach became apparent especially for the description of the XYZ states with heavy quarks, see e.g. [65] for an overview.

Dispersion Theory. In contrast to many other approaches, dispersion theory provides a model independent method to extract physical observables from dispersion relations on the basis of scattering amplitudes, see e.g. [66, 67]. A partial wave from a relativistic quantum field theory has a certain analytic structure in the complex plane and establishes cuts and poles. From the reaction threshold in a scattering experiment comes a right hand cut and another left hand cut is a consequence of crossing symmetry. Based on Cauchy's theorem applied on the complex scattering amplitudes, one obtains integral

equations which can be used to identify resonance poles in the complex s plane. Thereby, the inclusion of the left hand cut constitutes the main difficulty; theoretically, this could be achieved by solving the so-called Roy equations [68]. The data in order to evaluate the dispersive integrals could be taken either from theory, e.g. from ChPT calculations, or from experiment (“dispersive analyses”). The latter ones then provide a truly model-independent extraction of physical observables. Today, the most advanced determinations of the pole positions of the light scalar mesons stem from dispersive analyses [62].

Experiments

In this section, a few relevant big experiments for doing investigations of exotic hadrons will be mentioned very briefly. For further details, I refer to the conception drafts of the respective collaborations.

LHCb. The LHCb (Large Hadron Collider beauty) is an experiment which is suitable for investigating decays of hadrons with heavy quarks (charm and bottom) through productions of $b\bar{b}$ pairs [69]. It contributed to huge progress in search for exotic states within the last decade with the discovery of tetraquark resonances as excited states of the $X(4140)$ [70, 71] and the pentaquarks $P_c(4380)^+$, $P_c(4450)^+$ [72]. Furthermore, it was able for the first time to determine the quantum numbers of the $\chi_{c1}(3872)$ in 2013 [73]. In 2020, the first all-charm tetraquark state, the $X(6900)$, was discovered [74, 75]. Today, the LHCb collaboration counts 68 institutions from 15 countries. [76]

BESIII. BESIII (Beijing spectroscopy III) is an experiment with an e^+e^- collider, which is active since 2009 in Beijing, China. The international collaboration consists of 72 institutions from 15 countries [77]. Amongst other things, it is set up for light hadron and charmonium spectroscopy and provides decent high-precision experiments for charmonium physics due to its high luminosity [78].

BELLE / BELLE II. BELLE (II) is an experiment that does high precision physics in the beauty sector through B decays [79]. It was the first experiment in 2003 that detected the first exotic particle, the $\chi_{c1}(3872)$ [6], and thereby initiated a new era of hadron physics. The current flagship collider SuperKEKB performs e^+e^- collisions at extraordinary high luminosity [80]. Currently, the international collaboration consists of 115 institutions from 26 countries. [81]

PANDA. PANDA (antiProton Annihilation in Darmstadt) is an experiment under construction in Darmstadt which is worth to mention here due to its huge potential to gain knowledge about the nature of the strong interaction [12, 82]. As a $p\bar{p}$ machine, the hadron collider will be particularly important in order to investigate the structure of exotic states like tetraquarks, glueballs and hybrid mesons. With the measurement of line shapes e.g. of the $\chi_{c1}(3872)$ it will be instructive to reveal whether this state is a compact state or a hadronic molecule [83].

1.5 Theoretical Status on Exotic Four-Quark Candidates

Over the years, many theoretical approaches were established for doing investigations to describe tetraquarks and yet, we are far away from claiming that there are final agreements. Many publications from the last years described exotic states for different quark compositions: the ones in the light quark sector, heavy-light hidden-charm tetraquarks, open-charm and open-bottom, all-charm states and others. The findings presented in various publications show that conclusions about the inner structure strongly depend on the applied methods and models.

Take the mysteriously degenerated states $a_0(980)$ and $f_0(980)$ for example; we find a whole spectrum of conclusions about the inner composition of the a_0 : a strong dominance of a molecular $K\bar{K}$ component [84], a dominant $q\bar{q}$ with coupling to diquark-antidiquark fields [36], a pure diquark-antidiquark state [85] or a mixture of $K\bar{K}$ and $\eta\pi$ [47, 86].

Similar uncertainties could be found by looking at the charmonium-like candidates. For instance, it is highly debated what the popular $\chi_{c1}(3872)$ actually is – a four-quark state, and if so, it is unclear what it's composed of internally. It is often the case that certain studies are only considering one specific internal configuration at once to describe the states in question – for example, most quark model calculations, e.g. [21, 87, 88], are based on a diquark-antidiquark description that supposes that a certain input state like the $\chi_{c1}(3872)$ is a diquark-antidiquark state in order to gauge the model parameters. Similarly, studies like [89] from QCD sum rules also consider only a diquark-antidiquark structure a priori. Conversely, Ref. [90] states that the sum rule approach favours a molecular picture. A more cautious statement about the findings in this approach was given in [64], where the authors state that the χ_{c1} is at least neither a pure $c\bar{c}$ state, nor a pure molecule.

Contrary to that, a complete description of four-quark candidates with strong conclusions have to happen by considering an overlap of all possible substructures. This has been done for specific charmonium-like four-quark candidates from Dyson-Schwinger/Bethe-Salpeter equations [46, 91] by considering three possible tetraquark configurations. The resulting statement was e.g. that the χ_{c1} is predominantly a $D\bar{D}^*$ molecule. However, the inclusion of an ordinary $c\bar{c}$ component is still missing. Further problems are given by technical difficulties. Lattice QCD for example is generally a strong tool to extract observables from first principles, but charmonium-like states like the $\chi_{c1}(3872)$ are still hard to describe – descriptions of heavy-light four-quark states using a Born-Oppenheimer static-light approximation in non-relativistic lattice QCD are by now limited to $\bar{b}bqq$ systems, see e.g. [30–32]. A positive description of the $\chi_{c1}(3872)$ from the lattice is given by [28]; the authors see a candidate for the χ_{c1} below the DD^* threshold, but without being able to make definite statements about the inner composition. Moreover, the corresponding energy level still has to be confirmed as it is quite sensitive to lattice artefacts [8]. Ref. [35] emphasizes especially the importance of the $c\bar{c}$ component on the lattice, but also these results require confirmation [7].

We see that several theoretical frameworks are driven by technical and conceptual caveats and the results are diverse – many years may lie ahead of us in order to improve different methods to make them comparable on a quantitative level.

1.6 Goal of this Work & Outline

Judging from the insight given in the last section 1.5, we notice that the ensemble of theoretical descriptions for four-quark states is highly incomplete by now. The central goal of this thesis is to provide differentiated results for the properties of bound states and resonances in a framework which is able to describe an *entirety* of four-quark configurations in order to gain knowledge about the nature of exotic hadrons. This is especially valuable since most methods apart from ours are currently *not* considering the mixing between all three important four-quark compositions (meson-meson, hadro-charmonium, diquark-antidiquark) at once.

Moreover, these four-quark compositions are not necessarily the only ones that could describe a specific state with quantum numbers $I(J^{PC})$. Depending on the isospin I , quark-antiquark composite state poles should enter the 8-point Green function,

$$G_{\alpha_1 \dots \alpha_8}^{(8)}(x_1, \dots, x_8) = \langle 0 | T \psi_{\alpha_1}(x_1) \bar{\psi}_{\alpha_2}(x_2) \dots \psi_{\alpha_7}(x_7) \bar{\psi}_{\alpha_8}(x_8) | 0 \rangle, \quad (1.1)$$

as well (along with many other ones, coming from hybrids, glueballs and other exotic candidates) – we will further intensify this concern in chapter 3.

In this work we will present a method which makes it possible to calculate such an overlap of different tetraquark components with ordinary quarkonia. To our knowledge, the formalism presented in this work is the only one that is implementing a mixing on this level so far with functional methods. With that, we wish to make a valuable contribution to the community of theoretical exotic hadron physics.

Outline. First, we will briefly summarize the theoretical background of the Dyson-Schwinger framework. After this, the quark Dyson-Schwinger equation (DSE) and Bethe-Salpeter equations (BSEs) are covered. We discuss the solutions of the quark DSE and two-quark BSEs along with the corresponding complexities and the most important techniques in order to solve these. After that, we derive and discuss the coupled two-body tetraquark BSE which we solve in order to insert them into the four-quark equation. Then, results are shown for different candidates of pure four-quark states and mixed ones between four- and two-quark states. These are

- heavy-light, hidden- and open-charm XYZ tetraquark candidates in the charmonium sector (e.g. $\chi_{c1}(3872)$ and $Z_c(3900)$),
- light scalar states ($\sigma/f_0(500)$, $a_0(980)$, $f_0(980)$) as tetraquark states with quarkonium mixing and
- the recently discovered resonance X(6900) as a tetraquark state.

In the end, final conclusions will be drawn.

CHAPTER 2

THE DYSON-SCHWINGER FRAMEWORK

2.1 Functional Derivation from QCD

Similar to classical systems, it is helpful to know the equations of motion from the underlying theory to determine the properties of elementary particles. In QCD, the important processes such as particle propagations and interactions are described by fully dressed Green's functions which can be expressed as derivatives of QCD's effective action. In this chapter we will briefly sketch how to arrive there and in the end we will derive the quark Dyson-Schwinger equation (DSE), the equation of motion for the (inverse) quark propagator. Other Green's functions such as further propagators or interaction vertices can be derived analogously. An extensive review about numerous concepts we cover in this chapter (and much more) is given by [92]; further details can be found in various text books, e.g. [93, 94].

The most basic quantity of QCD is its Lagrange density, which we give in the Euclidian space:

$$\mathcal{L}_{\text{QCD}} = \sum_i \bar{\psi}_i (-\mathcal{D} + m_i) \psi_i + \frac{1}{4} \cdot F_{\mu\nu}^a F_{\mu\nu}^a. \quad (2.1)$$

The operator $D_\mu = \partial_\mu + ig t^a A_\mu^a$ is the covariant derivative which ensures local gauge invariance; A_μ^a and ψ_i are the gluon and quark fields and $F_{\mu\nu}^a = \partial_\mu A_\nu^a - \partial_\nu A_\mu^a - gf^{abc} A_\mu^b A_\nu^c$ is the gluon field strength tensor. The index i denotes the quark flavour.

The integral of the Lagrange density then defines the QCD action,

$$S_{\text{QCD}}[\psi, \bar{\psi}, A_\mu] = \int d^4x \mathcal{L}_{\text{QCD}}(\psi, \bar{\psi}, A_\mu), \quad (2.2)$$

which in turn defines the generating functional, the field theoretic equivalent to the partition function of a statistical mechanical system through a Legendre transformation,

$$Z[\eta, \bar{\eta}, j_\mu] = \int \mathcal{D}[q, \bar{q}, A_\mu] \exp \left(-S[\psi, \bar{\psi}, A_\mu] + \int d^4x \left(A_\mu^a j_\mu^a + \bar{\eta}_i \psi_i + \bar{\psi}_i \eta_i \right) \right). \quad (2.3)$$

The quantities j_μ^a , η_i and $\bar{\eta}_i$ are introduced source terms which we set zero when computing correlation functions.

To ensure that the integral (2.3) does not integrate over many equivalent paths in configuration space¹, one introduces Faddeev-Popov ghosts, non-physical particles which come into the Lagrangian by a delta function while gauge fixing:

$$\delta(\partial_\mu A_\mu^a) \rightarrow \exp\left(-\frac{1}{2\xi} \int d^4x (\partial_\mu A_\mu^a)^2\right) = \int \mathcal{D}C \exp\left(-\int d^4x \left(iC^a \partial_\mu A_\mu^a + \frac{\xi}{2} C^a C^a\right)\right) \quad (2.4)$$

The parameter ξ is the gauge parameter – throughout this work we will choose Landau gauge, which is defined by the limit $\xi \rightarrow 0$. An advantage of this is that the gluon propagator gets fully transversal which reduces complexity. The additional fields c_a and \bar{c}_a , are the ghost fields with which the resulting (expanded) Lagrangian is then given by

$$\begin{aligned} \mathcal{L}_{\text{eff}} = & \frac{1}{2} \cdot A_\mu^a \left[-\partial^2 \delta_{\mu\nu} - \left(\frac{1}{\xi} - 1\right) \partial_\mu \partial_\nu \right] A_\nu^a + \bar{c}^a \partial^2 c^a + g f^{abc} \bar{c}^a \partial_\mu (A_\mu^c c^b) \\ & - g f^{abc} (\partial_\mu A_\nu^a) A_\mu^b A_\nu^c + \frac{1}{4} \cdot g^2 f^{abc} f^{cde} A_\mu^a A_\nu^b A_\mu^c A_\nu^d \\ & + \sum_i \bar{\psi}_i (-\not{\partial} + m) \psi_i - i g \bar{\psi}_i \gamma_\mu t^a \psi_i A_\mu^a \end{aligned} \quad (2.5)$$

with the generating functional

$$\begin{aligned} Z[\eta, \bar{\eta}, \sigma, \bar{\sigma}, j_\mu] = & \int \mathcal{D}[\psi, \bar{\psi}, c, \bar{c}, A_\mu] \\ & \exp\left(-S[\psi, \bar{\psi}, c, \bar{c}, A_\mu] + \int d^4x \left(A_\mu^a j_\mu^a + \bar{\eta}_i \psi_i + \bar{\psi}_i \eta_i + \bar{\sigma} c + \bar{c} \sigma\right)\right). \end{aligned} \quad (2.6)$$

From Eq. (2.5) one can immediately see which kinds of Green's functions, including the ones with ghost contributions, can be obtained by taking the derivatives with respect to quark, ghost and gluon fields:

- propagators: quark, gluon, ghost
- vertices: quark-gluon, 3-gluon, 4-gluon, ghost-gluon

While a differentiation of the effective Lagrangian in the form of (2.5) only yields the tree level Green's functions, the fully dressed one-particle irreducible (1PI) versions could be derived by considering all quantum effects of QCD. The generating functional for those 1PI Green's functions, the effective action Γ , is defined by

$$i\Gamma[\psi, \bar{\psi}, c, \bar{c}, A_\mu] = \mathcal{G}[\eta, \bar{\eta}, \sigma, \bar{\sigma}, j_\mu] + \int d^4x \left(\bar{\psi}_i \eta_i + \bar{\eta}_i \psi_i + \bar{c} \sigma + \bar{\sigma} c + A_\mu j^\mu\right) \quad (2.7)$$

¹In non-Abelian gauge theories like QCD there is the problem of Gribov copies while gauge fixing [40, 95]. That means, it is not necessarily guaranteed that one truly integrates over a specific field configuration only once, and not over other equivalent ones as well. However, lattice studies on the gluon and ghost propagators indicate that the effects of Gribov copies are negligibly small [96, 97] in the energy regions of interest for us. Based on this, we will neglect their importance throughout this work.

as the Legendre transformation of the functional \mathcal{G} :

$$\mathcal{G}[\eta, \bar{\eta}, \sigma, \bar{\sigma}, j_\mu] := -i \ln Z[\eta, \bar{\eta}, \sigma, \bar{\sigma}, j_\mu]. \quad (2.8)$$

The effective action contains all quantum fluctuations, as it originates from the functional \mathcal{G} , which in turn includes Z and thus, the integration over all field configurations. At this point we introduce a few identities which result from the fact that \mathcal{G} and Γ are generating functionals for the fields and sources, respectively. Eq. (2.7) yields (flavour-index i explicit):

$$\begin{aligned} A_\mu(x) &= -\frac{\delta \mathcal{G}}{\delta j^\mu(x)} & \psi_i(x) &= -\frac{\delta \mathcal{G}}{\delta \bar{\eta}_i(x)} & \bar{\psi}_i(x) &= -\frac{\delta \mathcal{G}}{\delta \eta_i(x)} \\ j_\mu(x) &= \frac{\delta \Gamma}{\delta A^\mu(x)} & \eta_i(x) &= \frac{\delta \Gamma}{\delta \bar{\psi}_i(x)} & \bar{\eta}_i(x) &= -\frac{\delta \Gamma}{\delta \psi_i(x)} \end{aligned} \quad (2.9)$$

Derivatives of \mathcal{G} and Γ are reciprocal:

$$\int_y \frac{\delta^2 \mathcal{G}[j_i]}{\delta j_1(x) \delta j_2(y)} \frac{\delta^2 \Gamma[\varphi_i]}{\delta \varphi_1(y) \delta \varphi_2(z)} = -\delta(x-z) \Leftrightarrow \frac{\delta^2 \mathcal{G}[j_i]}{\delta j_2(x) \delta j_1(x)} = \left(\frac{\delta^2 \Gamma[\varphi_i]}{\delta \varphi_1(y) \delta \varphi_2(x)} \right)^{-1} \quad (2.10)$$

A derivative of the effective action can then be written down in terms of the QCD action with the fields φ shifted by a derivative term. This is often referred as the ‘‘master DSE’’ as it describes how the Green’s functions could be obtained on the basis of the QCD action S .

$$\frac{\delta \Gamma}{\delta \varphi(x)}[\varphi] = \frac{\delta S}{\delta \varphi(x)} \left[\varphi(x) + i \int_y \left(\frac{\delta^2 \Gamma}{\delta \varphi(x) \delta \varphi(y)} \right)^{-1} \frac{\delta}{\delta \varphi(y)} \right] \quad (2.11)$$

We made use of the identity

$$\frac{\delta}{\delta j(x)} = \int_y \frac{\delta^2 \mathcal{G}}{\delta j(x) \delta j(y)} \frac{\delta}{\delta \varphi(y)} \Leftrightarrow \frac{\delta}{\delta \varphi(x)} = \int_y \frac{\delta^2 \Gamma}{\delta \varphi(x) \delta \varphi(y)} \frac{\delta}{\delta j(y)}, \quad (2.12)$$

which transforms between derivatives with respect to the fields and derivatives with respect to the sources. With that it is possible to differentiate the effective action Γ to derive Dyson-Schwinger equations for 1PI Green’s functions. In this section we will do so for the quark DSE as it will be the most important one in this thesis. In the end we will make a short remark about other DSEs.

The quark DSE from the effective action. As a derivative of the effective action, the (inverse) quark propagator S_i reads

$$S_i^{-1}(x, y) = \frac{\delta^2 \Gamma[\psi, \bar{\psi}, A_\mu]}{\delta \bar{\psi}_i(x) \delta \psi_i(y)} \Big|_{\bar{\psi}_i = \psi_i = 0}. \quad (2.13)$$

The explicit form is derived via two differentiations of the effective action. We start by performing the first derivative,

$$\frac{\delta \Gamma}{\delta \bar{\psi}_i(x)}[\psi, \bar{\psi}, A_\mu] = \frac{\delta S}{\delta \bar{\psi}_i} \left[-\frac{\delta \mathcal{G}}{\delta \eta_i(x)}[\eta] + \frac{i\delta}{\delta \eta_i(x)} \right] \quad (2.14)$$

$$= (-\not{\partial} + m_i)\psi_i(x) + ig\gamma_\mu A_\mu(x)\psi_i(x) + ig\gamma_\mu \frac{\delta^2 \mathcal{G}}{\delta j_\mu(x) \delta \bar{\eta}_i(x)} \quad (2.15)$$

and continue by taking the second derivative to obtain the inverse quark propagator in position space:

$$\frac{\delta^2 \Gamma}{\delta \bar{\psi}_i(x) \delta \psi_i(y)} = (-\not{\partial} + m_i)\delta(x - y) + ig\gamma_\mu \frac{\delta}{\delta \psi_i(y)} \frac{\delta^2 \mathcal{G}}{\delta j_\mu(x) \delta \bar{\eta}_i(x)} \quad (2.16)$$

$$= S_{i,0}^{-1}(x - y) + ig\gamma_\mu \int_{s,t} D_{\mu\nu}(x - t) \Gamma_\nu^{\text{qg}}(t, y, s) S(s - x) \quad (2.17)$$

With Eq. (2.13), this is the quark DSE, the exact quantum equation of motion for the (inverse) quark propagator. As can be seen, it includes further Green's functions – the ones for the full gluon propagator and the quark-gluon vertex, which have to obey their own DSEs. Thus, solving the quark propagator in full requires the solution of a coupled system of DSEs. The DSEs for other Green's functions, e.g. for the gluon propagator $D_{\mu\nu}$ and the quark-gluon vertex Γ_μ^{qg} are derived similarly:

$$D_{\mu\nu}^{-1}(k) = \frac{\delta^2 \Gamma[\psi, \bar{\psi}, A_\mu]}{\delta A_\mu \delta A_\nu} \quad \Gamma_\mu^{\text{qg},i} = \frac{\delta^3 \Gamma[\psi, \bar{\psi}, A_\mu]}{\delta \bar{\psi}_i \delta A_\mu \delta \psi_i} \quad (2.18)$$

In the end, even these DSEs include ghost contributions and n -gluon vertices [40], which would have to be calculated simultaneously. It is common practice to apply models for Green's functions in order to reduce the computational effort in numerical calculations, although it is possible to approach the self-consistent system of DSEs as it is, albeit in a truncated form.

Renormalization. In quantum field theories like QCD it is natural that loop integrals diverge if they are not regularized somehow. Quantities like the coupling constant or the propagators can be determined at a specific energy scale, at which observables are fixed. With that we bypass the caveat that the unrenormalized Lagrangian yields quantities which are dependent on a certain regulator, e.g. an ultraviolet cutoff Λ .¹ In a

¹Other schemes are possible, e.g. dimensional [98] or Pauli-Villars regularization [99], to name but a few. However, we restrict ourselves to an ultraviolet cutoff here. Everything is simply transferable to other schemes by replacing the cutoff Λ by a regularization parameter of another kind, e.g. ε or Λ_{PV} .

renormalization scheme, one replaces the dependence on the cutoff with a dependence on the energy scale, the renormalization point. The renormalized quantities are related to the unrenormalized ones via renormalization constants, functions of the cutoff Λ and the renormalization point μ as follows:

$$X_i(\Lambda) = Z_i(\Lambda, \mu) X'_i(\mu) \quad (2.19)$$

By defining the renormalization constants, the relations between the (cutoff-dependent) fields and the renormalized (primed) ones are

$$\psi_i = \sqrt{Z_2^i} \psi'_i \quad A^\mu = \sqrt{Z_3} A'_\mu \quad g = Z_g g' \quad c = \sqrt{\tilde{Z}_3} c' \quad m_i = Z_{m_i} m'_i \quad (2.20)$$

and we define $Z_{1i} = Z_2^i Z_g \sqrt{Z_3}$. Further relations could be deduced via Slavnov-Taylor identities (STIs) [92]:

$$Z_1 = Z_g Z_3^{3/2} \quad \tilde{Z}_1 = Z_g \tilde{Z}_3 Z_3^{1/2} \quad Z_4 = Z_g^2 Z_3^2 \quad (2.21)$$

Consequently, the renormalized QCD action reads¹

$$\begin{aligned} S_{\text{QCD}}[\bar{\psi}, \psi, \bar{c}, c, A_\mu] \\ = \int d^4x \left[\sum_i (Z_2^i \bar{\psi}_i (-\not{\partial} + m_i) \psi_i - Z_{1i} g \bar{\psi}_i A \psi_i) + \frac{Z_3}{4} F_{\mu\nu}^a F_{\mu\nu}^a - \frac{Z_3}{2\xi} (\partial_\mu A_\mu)^2 \right] \end{aligned} \quad (2.22)$$

By calculating correlators, it turns out that every expression gets a renormalized version in quite a simple way via (2.20); for instance, the inverse renormalized tree-level quark propagator in momentum space reads

$$S_{i,0}^{-1}(p, \mu) = Z_2^i(\Lambda, \mu) (\not{p} - Z_m(\Lambda, \mu) m_i(\Lambda)). \quad (2.23)$$

Similarly, this can be applied to other Green's functions, and solving the associated DSEs yields to renormalized versions of the 1PI Green's functions as derivatives of the effective action. The renormalized *physical* quantities m_i and g then have to be extracted from experiment to describe physics at the renormalization scale properly.

2.2 The Quark Dyson-Schwinger Equation

QCD is the theory of quarks and gluons. While gluons are responsible for the actual forces that bind hadronic matter, quarks can be considered as *the* central objects that bound states and resonances consist of. All the information about the behaviour of a quark is encoded in its propagator. Since it will occur as a building block in larger diagrams, e.g. the bound state equations which we will introduce in chapter 3, it will be mandatory to calculate it by solving its equation of motion: the quark DSE. This section is dedicated to discuss the quark DSE and its ingredients along with how we deal with it in practice and how the solutions look like.

¹The prime symbols were dropped for convenience.

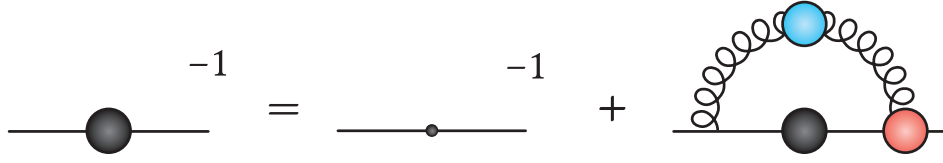


Figure 2.1: The quark DSE in its diagrammatic form. The black blobs represent the fully dressed quark propagator, the blue one the gluon propagator and the red one the quark-gluon vertex. The small black dot is the bare, interaction free quark propagator.

2.2.1 The Equation

The quark DSE is the exact equation of motion for the quark propagator $S(p)$. It is also referred as the “gap equation” and diagrammatically shown in Fig. 2.1. The momentum space representation is convenient for our purposes because we are interested in physics on particular energy scales in the first place. It is given by the Fourier transform of Eq. (2.17):

$$S^{-1}(p, \mu) = S_0^{-1}(p, \mu) + \Sigma(p, \mu) \quad (2.24)$$

Note that all indices – Dirac, colour and flavour – are suppressed for convenience. S_0 is the renormalized, bare quark propagator,

$$S_0^{-1}(p, \mu) = Z_2(\mu^2, \Lambda^2)(i\not{p} + Z_m(\mu^2, \Lambda^2)m_{\text{ren}}(\mu^2)), \quad (2.25)$$

and Σ is the quark self energy, given by

$$\Sigma(p, \mu) = -Z_1(\mu^2, \Lambda^2) \int_q g^2 D_{\mu\nu}^{ab}(k) \Gamma_a^\mu(q, p) S(q) i\gamma^\nu \tau_b, \quad (2.26)$$

where, g is the QCD coupling constant, $D_{\mu\nu}^{ab}$ is the gluon propagator, $k = q - p$ is the gluon momentum, $\Gamma_a^\mu(q, p)$ is the quark gluon vertex and τ_i are the generators of $SU(3)$, the colour gauge group, typically represented by using the eight Gell-Mann matrices λ_i :

$$\tau_i = \frac{\lambda_i}{2} \quad (2.27)$$

It is important to note that Eq. (2.24), due to renormalization, does not depend on the ultraviolet cutoff Λ^2 any more, but on the renormalization scale μ^2 . At this scale, the physical quantities are fixed, which is reflected by the renormalization condition

$$S^{-1}(p, \mu)|_{p^2=\mu^2} = i\not{p} + m_{\text{ren}}(\mu^2)|_{p^2=\mu^2}. \quad (2.28)$$

We see that the quark propagator in the vacuum¹ can be written by using two Dirac tensor structures, \not{p} and $\mathbb{1}$. By attaching two dressing functions $A(p^2)$ and $B(p^2)$ for the

¹By putting the quark into a medium one has to consider that the medium itself has a certain orientation in space-time. Then, the quark gets a further tensor structure proportional to γ^4 [100].

general solution as follows,

$$S^{-1}(p, \mu) = i\not{p}A(p^2, \mu^2) + B(p^2, \mu^2), \quad (2.29)$$

or equivalently

$$S(p, \mu) = -i\not{p}\sigma_v(p^2, \mu^2) + \sigma_s(p^2, \mu^2) \quad (2.30)$$

with

$$\sigma_v = \frac{A}{p^2 A^2 + B^2} \quad \text{and} \quad \sigma_s = \frac{B}{p^2 A^2 + B^2}, \quad (2.31)$$

this makes the full Dirac structure of the quark propagator. All the non-trivial, energy-dependent information is now stored in the two dressing functions A and B . The effective, renormalization point independent quark mass is then given by

$$M(p^2) = \frac{B(p^2, \mu^2)}{A(p^2, \mu^2)}. \quad (2.32)$$

2.2.2 The Need for Truncations

Although the quark DSE looks like a closed equation at a first glance, this is only true if every other occurring quantity is known a priori. Unfortunately, this is generally not the case – the gluon propagator and the quark-gluon vertex obey their own DSEs, and these DSEs contain further Green functions like 3- and 4-gluon vertices or ghost contributions [40]. Altogether, these form an infinite tower of coupled integral equations, which cannot be solved entirely in a finite amount of time by using numerical methods. For that reason, we need to truncate the DSEs at some point to be able to make a self consistent, iterative treatment numerically feasible. We distinguish between a Rainbow(-Ladder) (RL) truncation and beyond Rainbow(-Ladder) (BRL) truncations. RL means that we absorb the non-trivial structure of the full quark-gluon vertex Γ^μ into the gluon dressing [38, 101]. Then, the self energy term of the quark DSE expands into a sum of rainbow-like diagrams. RL truncations have the obvious caveat that they omit important dynamics which are generally stored in the dressed vertex – consequently, one might have to model them. Doing this reduces the complexity of the equation because (especially if the gluon propagator is modelled as well) the equation turns into a closed one as it decouples from the other DSEs. In contrast to that, BRL truncations take the quark-gluon vertex, or at least parts of its non-trivial structure, into account, but conversely, numerical computations may become more expensive. A comparison of different truncations, RL and BRL, on the level of light meson observables is given in [102]. In this work however, we use RL truncated equations along with an effective model which is described in the following section.

2.2.3 Effective Gluon

In course of this work, the idea in order to solve the quark DSE in RL truncation is to model the combination of the gluon propagator and the quark-gluon vertex to bring Eq. (2.24) in a closed form that could be solved with manageable numerical effort. The interaction model we used throughout this thesis is based on the works of Maris and

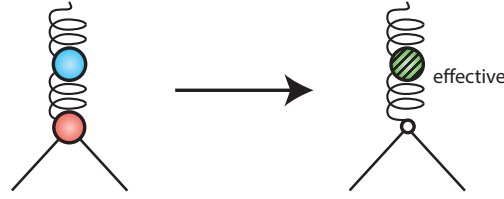


Figure 2.2: The Maris-Tandy model in a pictorial representation via Feynman diagrams. We absorb the dynamics of the full gluon propagator and the quark-gluon vertex *combined* by a bare quark-gluon vertex and an *effective gluon*. It contains the effective coupling \mathcal{G} , the centrepiece of the model.

Tandy [103, 104] – therefore, we will call it the “Maris-Tandy model” or simply “MT model” from here on.

We do the following replacement in the quark DSE,

$$Z_1 g^2 D_{\mu\nu}^{ab} \Gamma_a^{\nu} \rightarrow Z_2^2 \cdot \left(\delta_{\mu\nu} - \frac{k_\mu k_\nu}{k^2} \right) \frac{\mathcal{G}(k^2)}{k^2} \gamma^\nu \tau^b, \quad (2.33)$$

which is also shown in a pictorial representation in Fig. 2.2. $\mathcal{G}(k^2)$ is renormalization group invariant, which can be made plausible by counting the renormalization constant occurrences along with using the Slavnov-Taylor identity $Z_1 \tilde{Z}_3 = Z_2$ and the fact that $\tilde{Z}_1 = \tilde{Z}_3 Z_g \sqrt{Z_3} = 1$ is a valid choice¹ [105]:

$$Z_1 g^2 D\Gamma \sim Z_1 \cdot Z_g^{-2} \cdot Z_3^{-1} \cdot Z_1 = \frac{Z_2^2}{\underbrace{\tilde{Z}_3^2 Z_g^2 Z_3}_{=1}} = Z_2^2 \quad (2.34)$$

The *effective gluon* receives its name as it carries the *effective coupling*² \mathcal{G} – it is defined by an ultraviolet and an infrared part [103, 104]:

$$\frac{\mathcal{G}(k^2)}{k^2} = \mathcal{G}_k^{\text{uv}} + \mathcal{G}_k^{\text{ir}} = \frac{8\pi^2 \gamma_m \cdot \left[1 - \exp\left(-\frac{k^2}{\Lambda_t^2}\right) \right]}{\ln \left[e^2 - 1 + \left(1 + \frac{k^2}{\Lambda_{\text{QCD}}^2} \right)^2 \right]} + \frac{4\pi^2 \eta^7 k^4}{\Lambda^4} \exp\left(-\frac{\eta^2 k^2}{\Lambda^2}\right) \quad (2.35)$$

Whereas the ultraviolet part is determined by perturbation theory (note the logarithmic behaviour), the infrared part is the one which is actually modelled. Motivated by pion physics (cf. section 3.3), we use $\eta = 1.8$ and $\Lambda = 0.71$ GeV along with $\gamma_m = 12/(33-2N_f)$

¹That is because the ghost-gluon vertex fulfils $\Gamma^{\tilde{g}g} = \text{const.} \cdot \Gamma_0^{\tilde{g}g}$ due to the transversality of the gluon propagator in Landau gauge. The bare vertex is renormalization point independent, thus we can set $\tilde{Z}_1 = 1$.

²Note that we not only replace the dressed gluon propagator and the quark-gluon vertex, but also the running coupling g .

$$[S_{\alpha\beta}(p)]^c = \left(\text{---} \xrightarrow{p} \text{---} \right)^c = \text{---} \xleftarrow{p} \text{---} = S_{\beta\alpha}(-p)$$

Figure 2.3: The charge conjugation of a quark diagrammatically. The momentum flow direction inverts as well as the order of the Dirac indices does. The latter effect is nothing but a transposition of the whole quark propagator.

and $\Lambda_{\text{QCD}} = 0.234 \text{ GeV}$.¹ For light quarks u/d in the isospin symmetric limit, we set $m_q = 3.8 \text{ MeV}$ for the quark mass at the renormalization point. For numerical translation invariance of the radial integral it is possible to multiply $\mathcal{G}(k^2)$ with a regularization function, e.g. a Pauli-Villars regulator for some large scale Λ_{PV}^2 :

$$R_{\text{PV}}(k^2) = \frac{\Lambda_{\text{PV}}^2}{\Lambda_{\text{PV}}^2 + k^2} \quad (2.36)$$

The renormalization point, where “physical” quantities are fixed, is consistently set to $\mu = 19 \text{ GeV}$ in this work. This interaction allows us to set the cutoff $\Lambda \rightarrow \infty$ or, in numerical calculations, as high as necessary. Altogether, the quark DSE then has the following closed form

$$S^{-1}(p) = S_0^{-1}(p) + Z_2^2 C_F \int_q^\Lambda \frac{\mathcal{G}(k^2)}{k^2} T_{\mu\nu}(k) \gamma^\mu S(q) \gamma^\nu, \quad (2.37)$$

where Λ is the ultraviolet momentum cutoff and $T_{\mu\nu}(k)$ denotes the transverse projector. $C_F = 4/3$ is the colour Casimir. In appendix B.1 we briefly sketch how to approach this equation numerically.

2.2.4 Charge Conjugation

From the Lagrangian and the charge conjugation of quark spinors ($q \rightarrow Cq$), which exchanges a quark with its associated antiquark, we can read off the transformation behaviour for the quark propagator:

$$\mathcal{L}_{\text{quark}} = \bar{\psi}(i\not{p} + m)\psi \xrightarrow{\text{C.C.}} \bar{\psi} C^\dagger(i\not{p} + m)C \psi \quad (2.38)$$

With $C^\dagger = C^T = C^{-1}$ in our Euclidean convention, the charge conjugated quark $(S_{\alpha\beta})^c$ calculates via

$$(S_{\alpha\beta}(p))^c = C_{\alpha\eta}^\dagger S_{\eta\sigma}(p) C_{\sigma\beta} = S_{\beta\alpha}(-p) = S_{\alpha\beta}^T(-p). \quad (2.39)$$

The superscript T denotes the transposition of the Dirac structure; Greek indices are Dirac indices. Graphically, the charge conjugation of the quark propagator is displayed in Fig. 2.3 as a Feynman diagram.

¹Instead of (η, Λ) , the interaction can be rewritten by using other parameters, e.g. (ω, D) , which can be found in other publications. It is possible to convert between those parametrizations one-by-one [38].

2.2.5 Singularities and Branch Cuts

We assume the quark propagator to be holomorphic as well as the whole self energy integrand on the r.h.s. of Eq. (2.37). Due to singularities in the complex plane of the angular variable $z = \hat{p} \cdot \hat{q}$ which have a dynamic position depending on p^2 and q^2 , branch cuts inside the complex q^2 plane occur for fixed p^2 . For those q^2 , for which a singularity occurs at some $z \in [-1, 1]$, the angular integral is not defined and the resulting function of q^2 shows a non-removable discontinuity at this point. Blindly integrating over this discontinuity leads to numerical artefacts – the heavier the quark is, the more significant these artefacts get. Thus, strictly speaking, the q^2 integration path running from 0 to ∞ has to be deformed in a way that it doesn't hit any branch points. To give an example, a branch cut for $k^2 = (p - q)^2 = 0$ in the complex q^2 plane with an external momentum p^2 is parameterized by

$$c(p^2) = \left\{ p^2 (2z^2 - 1) \pm \sqrt{4p^4 z^2 (z^2 - 1)} : z \in [-1, 1] \right\} \subset \mathbb{C} \quad (2.40)$$

and has a circular shape with a single opening at $p^2 = q^2$. According to the integration rules of complex analysis, only those integration paths going through such an opening are properly defined. A pedagogical introduction into the topic of branch cuts in correlators along with simple examples is given by [108].

In practice, there are at least three possibilities to perform the radial integration:

- One can integrate *over* the branch cut on the real positive q^2 -axis naively, which yields a numerical error. If this error is acceptably small, this makes a proper way to calculate the quark propagator. Furthermore, it is the simplest one due to the low numerical effort. This method is well-applicable for the three light quarks: up, down and strange in our truncation and model.
- One can set the gluon momentum k as the integration variable, whose square is held in a real domain from 0 to ∞ . It is advantageous here that branch cuts are never hit, because the gluon propagator is not affected by the angular integral. The snag is given by the numerical effort, because the quark propagator inside the self energy integral has to be given in a domain, which is not known a priori during the iteration steps. E.g., for negative external p^2 , one requires knowledge about the quark propagator in the interior of a parabola in the complex plane, which could be accessed approximately by a mix of guessing and interpolating. It is worth to note that such a change of momentum routing requires a translation invariant integral, which is (numerically) ensured by a regularization procedure, e.g. the insertion of a Pauli-Villars regulator. It is possible to compute the quark propagator in the complex plane by setting up “shell parabolas” which become greater and greater, characterized by the apex and the opening, given by the quark momentum $q^2 = (p + k)^2$. We call this the *shell method* [109] which is described in appendix B.2 in greater detail. Other strategies of solving the quark propagator with k as an integration variable are possible as well, e.g. the direct iteration on complex parabolas in connection with the *Cauchy method* [110].
- Moreover, it is possible not to change the momentum routing inside the self energy

integral. Then, we have to deform the integration path such that no branch cut will be hit. Under the assumption that the integrand is holomorphic, this is possible as long as we do not overstep a pole. For this, one has to know the details about the branch cut structure. For Maris-Tandy interaction, two cuts occur due to the divergences from the logarithmic part of the function $\mathcal{G}(k^2)$. A possible integration path that avoids overstepping the cuts is given by

$$q^2(p^2, t) = \begin{cases} \exp [\ln(\varepsilon^2) + t (\ln(p^2) - \ln(\varepsilon^2))] & t \in [0, 1] \\ |p^2|t \cdot \exp (i \arg(p^2) \cdot (2 - t)) & t \in (1, 2] \\ \exp [\ln(2|p^2|) + (t - 2) (\ln(\Lambda^2) - \ln(2|p^2|))] & t \in (2, 3]. \end{cases} \quad (2.41)$$

Additionally, from a numerical point of view, this integration path is a sophisticated one, because a possible grid of integration sampling points set up for the domain $t \in [0, 3]$ ensures a proper logarithmic integration with respect to q^2 .

Those three methods allow us to access the quark propagator in the complex plane, but there are important remarks to be done: For a proper description of quarks in general, the latter two methods are the way to go; especially for heavy quarks, where the “naive” method (the first one) fails because of the problematic integration over the branch cut. For the third method it is necessary to know the location of all poles occurring in the self energy integral. Dynamically generated poles are extremely hard to catch – in practice, an *assumption* has to be made that there are no additional poles apart from the analytic one “disturbing” the path deformation. The second method is not driven by any of those problems; the numerical bottleneck is given by the distance between the shell parabolas and the interpolation routine for any point in between. However, one can investigate systematically, at which point the solution converges and fix the setup at a configuration where this convergence is reached sufficiently well.

2.2.6 Solution

The solution of the quark propagator is shown in Fig. 2.4 with A , B and M as functions of p^2 on the real axis. It is presented for a small current quark mass $m = 3.8$ MeV (left) and for the chiral limit (right) where the quark mass is zero. We see that the effects of dynamical mass generation get more and more suppressed in the ultraviolet, whereas these effects are distinct in the infrared. So, in the chiral limit, the quark indeed becomes massless for large p^2 , where the QCD running coupling is also vanishing asymptotically. In the infrared limit, where chiral physics are manifested, the effective mass of a chiral quark is given by around 470 – 480 MeV and for $m_{\text{ren}}(\mu^2) = 3.8$ MeV (realistic u - and d -quarks), the effective quark mass is given by 480 – 490 MeV. Treating heavier quarks like strange and charm quarks consequently leads to higher quark masses and the effects of dynamical mass generation are not as significant as in the light quark case. A deeper analysis of the quark propagator in the complex p^2 plane entails symmetries, especially under a sign flip in the imaginary part of p^2 . The real parts of the dressing functions are symmetric whereas the imaginary parts are antisymmetric as we complex conjugate the momentum $p^2 =: z$,

$$A(z^*) = A^*(z) \quad \text{and} \quad B(z^*) = B^*(z). \quad (2.42)$$

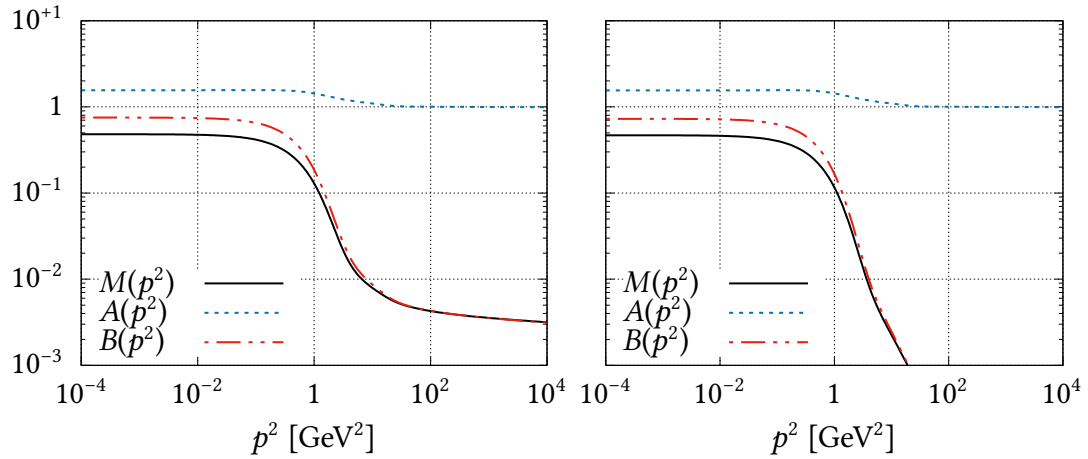


Figure 2.4: The quark dressing functions for a small current quark mass $m = 3.8$ MeV (left panel) and in the chiral limit for $m = 0$ MeV (right panel), respectively. The function values for A are dimensionless, whereas the function values of B and M have the dimension GeV.

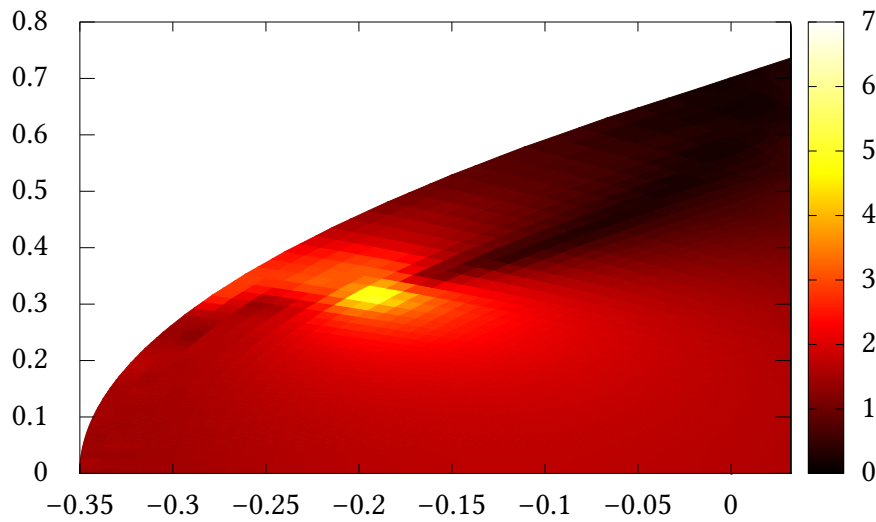


Figure 2.5: Heat map of the vector dressing function σ_v of the quark propagator as a function of the complex momentum p^2 . The abscissa denotes $\text{Re}(p^2)$ and the ordinate denotes $\text{Im}(p^2)$, both given in GeV^2 . The quark mass we used is given by 3.8 MeV. We find singularities at $p^2 \approx (-0.2 \pm 0.3 i) \text{GeV}^2$.

The denominator of the dressing functions of the “non-inverse” quark dressing functions σ_v and σ_s , which reads

$$\text{den}(p^2) = \frac{1}{p^2 A^2(p^2) + B^2(p^2)}, \quad (2.43)$$

leads to a pole structure, which is shown in Fig. 2.5 for $m_{\text{ren}} = 3.8$ MeV as a heat map. With the symmetries mentioned before in Eq. (2.42), two complex conjugate poles occur at $p^2 \approx (-0.2 \pm i 0.3)$ GeV symmetric with respect to a reflection on the real axis. Later we will see that these poles play an important role in order to describe bound states of quarks (and antiquarks) in bound state equations.

CHAPTER 3

BETHE-SALPETER EQUATIONS

As pointed out in the previous section, Dyson-Schwinger equations describe the dynamics of quarks and gluons on the level of 1PI Green's functions, i.e. their propagators and vertices. In order to describe bound states and resonances, equations of motion are required that put the quark constituents together with a binding potential. A solution of these equations should then include information about the energy, the decay properties and the spatial structure of the state. In hadron physics, we call these equations Bethe-Salpeter equations (BSEs), firstly described in the 50s [111]. In this thesis, these equations will make the most central tool in order to do investigations for exotic hadrons. This chapter should provide a brief, but clear overview about how to derive and solve these equations in general. Furthermore, we will discuss the $q\bar{q}$ equation and the properties of $J = 0, 1$ mesons and diquarks in detail for various quark configurations as they will be of great interest for the inner structure of four-quark states.

3.1 Derivation

First, we will briefly¹ derive a generic n -quark meson bound state equation with $n/2$ quarks and $n/2$ antiquarks. For that, we start with the $(2n)$ -quark Green's function G which is defined by the vacuum expectation value of $2n$ time-ordered quark field operators:

$$G_{\alpha_1 \dots \alpha_{2n}}^{(2n)}(x_1, \dots, x_{2n}) = \langle 0 | T \psi_{\alpha_1}(x_1) \bar{\psi}_{\alpha_2}(x_2) \dots \psi_{\alpha_{2n-1}}(x_{2n-1}) \bar{\psi}_{\alpha_{2n}}(x_{2n}) | 0 \rangle \quad (3.1)$$

where the superindices α_i summarize the Dirac, colour and flavour structure. The QCD Hamiltonian has a variety of eigenstates $|\lambda\rangle$; we can formulate a corresponding completeness relation as follows [112],

$$\mathbb{1} = \sum_{\lambda} \frac{1}{(2\pi)^3} \int \frac{d^3 p}{2(\mathbf{p}^2 + m_{\lambda}^2)} |\lambda\rangle \langle \lambda|. \quad (3.2)$$

¹This could be considered as a short, but generalized version of the derivation provided in the review article [38]. More details along with useful comments could be found there and in [112].

The eigenstates $|\lambda\rangle$ span a state space with countably infinite elements – among others, it contains colourless mesons, baryons and multihadron states as well as coloured states such as diquarks. In fact, every composite state of QCD makes an element of this state space by definition.

Inserting (3.2) into (3.1) and subsequently Fourier transforming the result yields the spectral decomposition of G in momentum space:

$$G_{\alpha_1 \dots \alpha_{2n}}^{(2n)}(P, p_1, \dots, p_{2n-2}) = \sum_{\lambda} \frac{\mathcal{R}_{\alpha_1 \dots \alpha_{2n}}^{\lambda, n}(P, p_1, \dots, p_{2n-2})}{P^2 + M_{\lambda}^2} + \text{regular terms} \quad (3.3)$$

P is the total momentum and p_i are relative momenta between the quarks. It becomes visible that the objects of interest in this thesis, namely hadrons, generate poles in G ; to each of those we can assign an individual residue

$$\mathcal{R}_{\alpha_1 \dots \alpha_{2n}}^{\lambda, n} := \langle 0 | \psi_{\alpha_1} \dots \bar{\psi}_{\alpha_n} | \lambda \rangle \langle \lambda | \psi_{\alpha_{n+1}} \dots \bar{\psi}_{\alpha_{2n}} | 0 \rangle \quad (3.4)$$

which carries all the relevant non-trivial information about G in the vicinity of the bound state pole. As an abbreviation, we define the so-called Bethe-Salpeter wave function $\Psi^{\lambda, n}$ as the transition element between the vacuum and a bound state [113]:

$$\Psi_{\alpha_1 \dots \alpha_n}^{\lambda, n}(P, p_1, \dots, p_{n-2}) := \langle 0 | \psi_{\alpha_1} \dots \bar{\psi}_{\alpha_n} | \lambda \rangle \quad (3.5)$$

From here on, we will drop the index λ and act as if we were close to the pole of a specific state. Alternatively to Eq. (3.1), the $2n$ -quark Green's function could also be written by using T , the non-trivial part of the scattering matrix S (indices α_i implicit):

$$\begin{aligned} G^{(2n)} &= G_0^{(n)} + G_0^{(n)} K^{(n)} G^{(2n)} = G_0^{(n)} + G_0^{(n)} T^{(2n)} G_0^{(n)} \quad \text{with} \\ T^{(2n)} &= K^{(n)} + K^{(n)} G_0^{(n)} T^{(2n)}, \end{aligned} \quad (3.6)$$

Here, $K^{(n)}$ is the n PI scattering kernel with respect to quark propagators and $G_0^{(n)}$ is the product of n free, non-interacting, full quark propagators. By taking the limit $P^2 \rightarrow -M^2$ where M is the on-shell mass of the composite state we're interested in, Eqs. (3.3) – (3.6) yield the conditions

$$\begin{aligned} G^{(2n)}(P, p_1, \dots, p_{2n-2}) &\xrightarrow{P^2 \rightarrow -M^2} \frac{\Psi^{(n)}(P, p_1, \dots, p_{n-1}) \bar{\Psi}^{(n)}(P, p_n, \dots, p_{2n-2})}{P^2 + M^2} \quad \text{or} \\ T^{(2n)}(P, p_1, \dots, p_{2n-2}) &\xrightarrow{P^2 \rightarrow -M^2} \frac{\Gamma^{(n)}(P, p_1, \dots, p_{n-1}) \bar{\Gamma}^{(n)}(P, p_n, \dots, p_{2n-2})}{P^2 + M^2}, \end{aligned} \quad (3.7)$$

respectively, where we define the Bethe-Salpeter amplitude Γ (BSA) via an amputation of the free n -quark propagator from the wave function:

$$\Psi_{\alpha_1 \dots \alpha_n}^{(n)} = [G_0^{(n)} \Gamma^{(n)}]_{\alpha_1 \dots \alpha_n} \quad (3.8)$$

Altogether, we obtain the homogeneous BSEs for the wave function and for the amplitude, respectively, as eigenvalue equations for the eigenvalue $\lambda = 1$ by comparing the residues in (Eq. 3.6):

$$\Psi_{\alpha_1 \dots \alpha_n}^{(n)} = [G_0^{(n)} K^{(n)} \Psi]_{\alpha_1 \dots \alpha_n} \quad \text{or} \quad \Gamma_{\alpha_1 \dots \alpha_n}^{(n)} = [K^{(n)} G_0^{(n)} \Gamma]_{\alpha_1 \dots \alpha_n} \quad (3.9)$$

The possibility of a formulation of an inhomogeneous BSE persists if we absorb the poles in (3.7) by the amplitudes. Then, one searches for poles in $\Gamma(P)$ instead.

Normalization. Due to the homogeneity of the BSEs in (3.9), the wave function Ψ and the amplitude Γ are unspecified with respect to a complex normalization constant. In order to determine this constant, we have to specify an adequate criterion. Here, this criterion is formulated by differentiating G with respect to the total momentum squared using the chain rule, which yields the relation

$$\frac{dG^{(2n)}}{dP^2} = - (G^{(2n)})^{-1} \frac{dG^{(2n)}}{dP^2} (G^{(2n)})^{-1}, \quad (3.10)$$

where we could insert (3.7) in order to obtain

$$\left[\bar{\Psi} \frac{d(G^{(2n)})^{-1}}{dP^2} \Psi \right]_{P^2 = -M^2} = 1 \quad (3.11)$$

in the vicinity of the bound state pole, i.e. $P^2 \approx -M^2$. Further inserting (3.8) and using (3.10) inversely for G_0 yields the normalization criterion for the amplitude Γ :

$$\left[\bar{\Gamma} \left(\frac{dG_0^{(n)}}{dP^2} + G_0^{(n)} \frac{dK^{(n)}}{dP^2} G_0^{(n)} \right) \Gamma \right]_{P^2 = -M^2} = -1 \quad (3.12)$$

This criterion was firstly formulated by Cutkosky and Leon in [114]. Equivalently, the BSA could be normalized via the Nakanishi criterion which connects the differential of the BSE eigenvalue¹ with a closed loop of BSAs [115]:

$$\left[\frac{d\lambda(P^2)}{dP^2} \right]_{P^2 = -M^2}^{-1} = \bar{\Gamma} G_0 \Gamma \quad (3.13)$$

Whereas this criterion is less complex than (3.12) as it does not include a two-loop diagram, we will use (3.12) consistently in this work because the mentioned reduction of complexity does not hold for RL truncated kernels as we will see later.

Leptonic decay constants. An electroweak decay of a bound state $|\lambda\rangle$ happens through a transition between the bound state and the QCD vacuum while coupling to a current,

¹Cf. the right hand side of Eq. (3.9), which is an on-shell relation where $\lambda = 1$ holds. For the Nakanishi criterion we generalize the on-shell BSE to off-shell momenta, where eigenvalues different than 1 could occur. Then, the BSE eigenvalue is a function of the total momentum, $\lambda = \lambda(P^2)$.

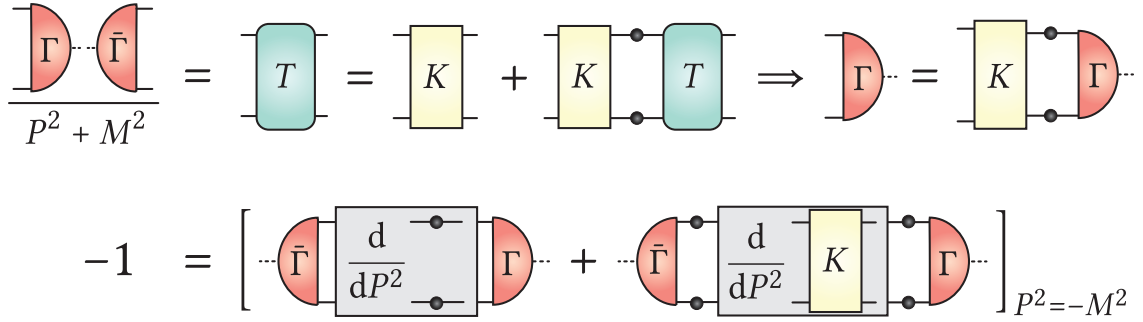


Figure 3.1: Graphical sketch of the derivation for the homogeneous two-quark Bethe-Salpeter equation (first line) and the normalization criterion (second line) as Feynman diagrams.

which defines the (gauge-invariant) electroweak decay constant f_λ [38]:

$$f_\lambda \sim \langle 0 | j_a^{(\mu)}(x) | \lambda \rangle \quad (3.14)$$

The quantum numbers of the current j , denoted by a , have to be chosen in a way that an electroweak decay is possible. In that sense, a pseudoscalar meson couples to an axialvector current whereas a vector meson couples to a vector current. Eq. (3.14) can be translated into a symbolic representation as follows:

$$f_\lambda M_\lambda \sim \tilde{\Gamma}_a^{(\mu)} G_0^{(n)} \Gamma^{(n)} \quad (3.15)$$

The quantum numbers and thus the form of the vertex $\tilde{\Gamma}_a^{(\mu)}$ is explicitly determined by the current $j_a^{(\mu)}$.

Important cases. In practice, we will solve the BSE for the amplitude $\Gamma^{(n)}$, where the cases $n = 2$ and $n = 4$ will be particularly interesting in course of this thesis. For a quick comprehension of the vital parts of the derivation, we show the most important step of the derivation along with the normalization criterion as Feynman diagrams in Fig. 3.1 for $n = 2$. In that sense, the following sections of this chapter will exclusively cover two-quark BSEs; four-quark states will be addressed in chapter 4.

3.2 The Two-Quark BSE

The simplest BSE we could imagine to solve for a composite state of quarks and antiquarks is the $q\bar{q}$ meson one. It contains only one interaction kernel diagram and has comparably simple kinematics. As a Feynman diagram, the BSE is shown in Fig. 3.2.

Due to momentum conservation at every vertex, the two-quark amplitude only links two distinct momenta, the total momentum P and the relative momentum between the quarks p . The momenta of the two quarks, which we call p_\pm according to Fig. 3.2 are then

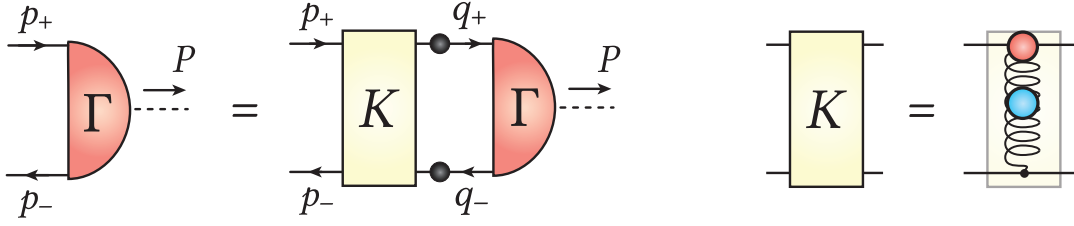


Figure 3.2: *Left panel:* The meson BSE as a Feynman diagram. All indices (Lorentz, Dirac, flavour and colour) are implicit. For convenience, spin lines and momentum flow are always pointing into the same direction. *Right panel:* The interaction kernel K has the same form as the quark self energy kernel enforced by the axWTI.

given by

$$p_+ = p + \eta P \quad \text{and} \quad p_- = p + (\eta - 1)P, \quad (3.16)$$

where $\eta \in [0, 1]$ is an arbitrary momentum routing parameter, which determines how much of the total momentum is carried by the particular quark. In the case of equal quark masses, it is reasonable to set $\eta = 0.5$; otherwise, we will later see that a more asymmetric routing will make sense for heavy-light states for technical reasons – although the parameter is in fact arbitrary. The kernel K depends on three momenta: the total momentum P and the external/internal relative momenta p/q . Applying the Feynman rules yields the $q\bar{q}$ BSE as an integral equation, graphically shown on the left hand side in Fig 3.2:

$$\Gamma_B^A(P, p) = \int_q K_{BD}^{AC}(P, p, q) [S(q_+) \Gamma(P, q) S(q_-)]_D^C \quad (3.17)$$

The calligraphic superindices $\mathcal{A} \dots \mathcal{D}$ include Dirac-, flavour and colour indices; possible Lorentz indices of the amplitudes are suppressed. At this point it is worth to mention that the propagators of the two quarks are not necessarily the same quantities. In the case of non-equal constituents we have to apply a more general notation and write $S(q_+) \rightarrow S_1(q_+)$ and $S(q_-) \rightarrow S_2(q_-)$ for example.

The full solution of this equation, the BSA, lives in the product space of a 4×4 dimensional Dirac space, a $N_f \times N_f$ dimensional flavour space and a $N_c \times N_c$ dimensional colour space (where the physical value $N_c = 3$ is always set in our calculations). Additionally, for a non-vanishing angular momentum ($J \neq 0$) the amplitude itself is a Lorentz tensor, otherwise a scalar:

$$\Gamma^{(\mu), \alpha\beta, AB, ab} = \Gamma_{\text{Dirac}}^{(\mu), \alpha\beta} \otimes \Gamma_{\text{Colour}}^{AB} \otimes \Gamma_{\text{Flavour}}^{ab} \quad (3.18)$$

In appendix A, our flavour- and colour space conventions are shown explicitly.

3.3 Truncations

So far, the form of the BSE kernel was not specified, yet. The self energy kernel of the quark DSE and the scattering kernel K from the two-quark BSE are related via the

axial-vector Ward-Takahashi identity (axWTI) [43],

$$(\gamma_5 \Sigma(p_-) + \Sigma(p_+) \gamma_5)_{\alpha\beta} = - \int_q K_{\alpha\gamma, \beta\delta}^{(2)}(p, q, P) (\gamma_5 S(q_-) + S(q_+) \gamma_5), \quad (3.19)$$

which retains chiral symmetry and all the associated effects. Since chiral symmetry describes vital characteristics of low-energy QCD [40], a breaking of this identity would be dramatic. The axWTI yields that most generally, we have to adopt the same form for the scattering kernel as it occurs in the self energy term of the quark DSE. Thus, we set¹

$$K = Z_1 g^2 i\gamma_\mu D_{\mu\nu}(q-p) \Gamma_v^{\text{qg}}(P, p, q). \quad (3.20)$$

We see that this kernel is driven by the exact same “problems” as the quark DSE: we have to know the gluon propagator and the quark-gluon vertex to know the kernel exactly. Whereas it just sounds reasonable to apply the same truncation here as we did in the quark DSE, the axWTI even forces us to do so since the truncations and interaction models we chose for the quark DSE propagate through the WTI (3.19) into the BSE kernel. So, we will apply the Rainbow-Ladder truncation also for the meson BSE. Here, it becomes obvious why the truncation in the BSE is basically called *Rainbow-Ladder* (RL) truncation: its visual appearance in a Feynman diagram has a ladder-look because of the vertical curly line of the exchange gluon; this is visualized on the right hand side of Fig. 3.2.

Applying the MT-interaction like in the quark DSE as well, the equal-mass constituent BSE in Eq. (3.17) is given by

$$\Gamma^{(\rho)}(P, p) = -Z_2^2 C_F \int_q \frac{\mathcal{G}(k^2)}{k^2} T_{\mu\nu}(k) \gamma_\mu S(q_+) \Gamma^{(\rho)}(P, q) S(q_-) \gamma_\nu, \quad (3.21)$$

where $k := q - p$.

3.4 Quantum Numbers

In the two-body BSE we could distinguish between states with different quantum numbers $I(J^{PC})$. We will work in the isospin symmetric limit – thus, the isospin quantum number will only affect the flavour part of the wave functions, but not the observables. The quantum numbers J, P and C however could be fixed by specifying the amplitudes. In this section we will restrict ourselves to states with $J = 0, 1$ and discuss the amplitude construction and the corresponding solutions.

3.4.1 (Pseudo-)Scalar $q\bar{q}$ Mesons

The BSA of a $J = 0$ $q\bar{q}$ meson is a Lorentz scalar and its Dirac part can generally be written as a linear combination of four basis elements. The difference between scalar and pseudoscalar mesons is reflected in the parity quantum number – the eigenvalue

¹For readability reasons, the colour part of the kernel is suppressed.

of the parity transformation operator \mathcal{P} when applying it on the amplitude. The parity transformation on a generic $J = 0$ BSA Γ is defined as follows (cf. appendix C),

$$\mathcal{P}(\Gamma(P, p)) = \gamma^0 \Gamma(\Pi P, \Pi p) \gamma^0. \quad (3.22)$$

The operator Π is the parity operator for four vectors, given by $\Pi = \text{diag}(1, -1, -1, -1)$. A possible choice of basis elements for scalar ($P = +$) mesons is given in the following [116]:

$$\begin{aligned} b_1^+(P, p) &= \mathbb{1} & b_2^+(P, p) &= -i\mathcal{P} \\ b_3^+(P, p) &= -i\not{p} & b_4^+(P, p) &= [\mathcal{P}, \not{p}] \end{aligned} \quad (3.23)$$

Factors of i and negative signs are inserted such that the dressing functions become real and positive in all components. However, they do not change the BSA overall – any scalar prefactor gets absorbed by the associated dressing function. The latter two basis elements correspond to p -waves [38], which have to be considered by describing a meson as a covariant, thus relativistic composite state. The pseudoscalar ($P = -$) basis is constructed by multiplying γ_5 to any basis element of the scalar basis in order to flip the parity sign:

$$b_i^-(P, p) = \gamma_5 b_i^+(P, p) \quad (3.24)$$

The full Dirac part of an amplitude is then given by

$$\Gamma^{\text{Dirac}}(P, p) = \sum_{i=1}^4 b_i(P, p) \cdot F_i(P, p) \quad (3.25)$$

As objects consisting of quarks with colour and flavour, the BSA lives in the colour and flavour space, too. The full amplitude is then given by the dyadic product of the different sensor parts

$$\Gamma_{\alpha\beta, AB, ab}^e = \Gamma_{\alpha\beta}^{\text{Dirac}} \otimes \Gamma_{AB}^{\text{colour}} \otimes \Gamma_{ab}^{\text{flavour}, e}. \quad (3.26)$$

The construction of the colour and flavour part happens by

- demanding that mesons are observable particles living in the colour singlet¹, which is represented by the unity matrix in colour space:

$$\Gamma_{AB}^{\text{colour}} = \delta_{AB} \quad (3.27)$$

- ensuring the correct flavour quantum numbers (isospin, strangeness, charm, ...). For instance, pions are pseudoscalar mesons and live in the isotriplet which could be represented by the three flavour matrices

$$r^+ = u\bar{d} = \frac{1}{\sqrt{2}} (\sigma_1 + i\sigma_2) \quad ; \quad r^- = d\bar{u} = \frac{1}{\sqrt{2}} (\sigma_1 - i\sigma_2) \quad ; \quad r^0 = (u\bar{u} - d\bar{d}) = \sigma_3 \quad (3.28)$$

with $\Gamma_{ab}^{\text{flavour}, e} = r_{ab}^e$, where σ_i are the Pauli spin matrices. Factors of $\sqrt{2}$ are motivated

¹The corresponding composition follows from the colour $SU(3)$: $3 \otimes \bar{3} = 8 \oplus 1 = \text{octet} \oplus \underline{\text{singlet}}$.

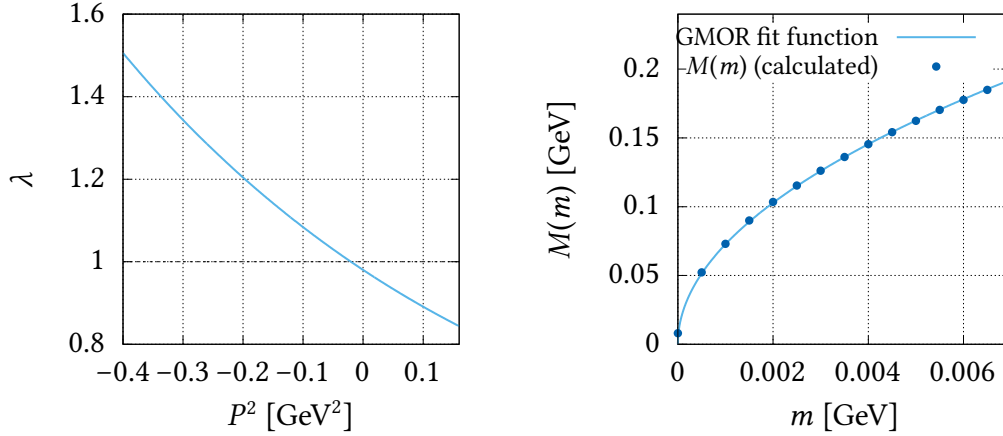


Figure 3.3: At the left: Spline-interpolated plot of the function $\lambda(P^2)$ for the π meson. One can see, that Eq. (3.30) produces one bound state for $P^2 \in \mathbb{R}^-$, which corresponds to a real, physical mass $M > 0$. At the right, the calculations for $M(m)$ are displayed. A corresponding fit function $f_a(m) = \sqrt{am}$ shows the typical behaviour of the GMOR relation and verifies that the effects of dynamical chiral symmetry breaking are conserved in the chosen interaction. All calculations are done in Maris-Tandy interaction.

by the value of N_f and ensure a consistent normalization as follows:

$$r_{ab}^e r_{ba}^e = N_f \quad (3.29)$$

Mass iteration. As shown in the previous chapter, a BSE solution is an eigenstate of a kernel $\mathcal{K} := K^{(2)}G_0^{(2)}$ for the eigenvalue $\lambda(P^2) = 1$ on the mass shell:

$$\lambda(P^2) \Gamma(P, p) = \int_q \mathcal{K}(P, p, q) \Gamma(P, q), \quad (3.30)$$

Once a momentum P^2 is found such that $\lambda(P^2) = 1$ and the dressing functions are determined, the equation is solved and we can identify the mass with $P^2 = -M^2$ as long as P^2 is a negative, real number. A solution technique for this equation can be found in chapter C.1.3. Briefly sketched, we solve Eq. (3.30) for various P^2 numerically to extract the eigenvalue curve $\lambda(P^2)$. As an example, the eigenvalue curve of the pion is displayed on the left panel of Fig. 3.3. Besides that, another interesting function is the mass curve $M(m)$, the bound state mass as a function of the quark mass. Here, we vary the quark mass consistently as we wish to calculate the properties of hypothetical¹ states. Such a curve is sketched on the right hand side of Fig. 3.3 for pseudoscalar $q\bar{q}$ mesons. We see a square root dependency here, according well to the leading term of the Gell-Mann-Oakes-Renner (GMOR) relation [117]. This includes that the pseudoscalar $q\bar{q}$ meson becomes the massless Goldstone boson according to the effects of spontaneous chiral symmetry breaking in QCD's chiral limit ($m = 0 \Rightarrow M = 0$).

¹“hypothetical” because in nature we only observe specific quarks with discrete masses, but in calculations we are not restricted to those.

3.4.2 (Axial-)Vector $q\bar{q}$ Mesons

For vector and axialvector mesons, the BSE (3.21), has the same structure as the (pseudo)scalar one; the only difference between the (pseudo)scalar and the (axial)vector BSAs is the on-shell Dirac structure, which is the product of the $J = 0$ Dirac bases and the Lorentz structures $\{ \gamma_\mu, p_\mu, P_\mu \}$. Due to transversality of the bound state propagator on the mass shell, the basis elements with a P_μ participation drop out and we just have to consider eight basis elements in total. A possible choice for the bases of a vector (-) state amplitude is given in the following [116]:

$$\begin{aligned}
b_1^{\mu-}(P, p) &= i\gamma_T^\mu & b_2^{\mu-}(P, p) &= \gamma_T^\mu \mathcal{P} \\
b_3^{\mu-}(P, p) &= (-\gamma_T^\mu p + p_T^\mu \mathbb{1}) (p \cdot P) & b_4^{\mu-}(P, p) &= (i\gamma_T^\mu [\mathcal{P}, \not{p}] + 2ip_T^\mu \mathcal{P}) \\
b_5^{\mu-}(P, p) &= \mathbb{1} p_T^\mu & b_6^{\mu-}(P, p) &= ip_T^\mu \mathcal{P} (p \cdot P) \\
b_7^{\mu-}(P, p) &= -ip_T^\mu \not{p} & b_8^{\mu-}(P, p) &= p_T^\mu [\mathcal{P}, \not{p}]
\end{aligned} \tag{3.31}$$

Again, an multiplication with a γ_5 matrix flips the parity quantum number and transforms a vector (-) into an axialvector (+) element (and vice versa):

$$b_i^{\mu+} = \gamma_5 b_i^{\mu-} \tag{3.32}$$

As in the pseudoscalar case, other choices for the basis elements are possible as long as they are still a generating system of the corresponding Dirac space. Factors of $(p \cdot P)$, i and negative signs are, again, optional and get absorbed by the dressing functions. The full Dirac part of the amplitude can then be written down as

$$\Gamma(P, p) = \sum_{i=1}^8 b_i^{\mu-}(P, p) \cdot F_i(P, p). \tag{3.33}$$

The parity quantum numbers can be checked by applying the parity transformation on the $J = 1$ BSA (cf. appendix C)

$$\mathcal{P}(\Gamma^\mu(P, p)) = -\gamma_0 \Pi^{\nu} \Gamma_\nu(\Pi P, \Pi p) \gamma_0. \tag{3.34}$$

The mass iteration procedure happens in an analogous way as in chapter 3.4.1 and is described in more detail in chapter C.1.3.

3.5 Normalization and Decay Constants

As already mentioned in 3.1, the BSA is undetermined up to a constant prefactor such that a normalization criterion had to be defined. To become able to use a BSA in a larger Feynman diagram, a normalization is mandatory as it defines important properties such as the charge of a hadron or its decay constant. This happens e.g. via the Leon-Cutkosky condition [114], in which we differentiate the trace of a closed meson-meson loop with respect to the total momentum P^2 . Doing this, it is worth the mention that the differential merely acts on a few special terms, for instance the quark propagators in the first summand and the kernel in the second summand of Eq. (3.35), but never on the amplitudes, whose

$$-1 = \left[\dots + \dots \right]_{P^2 = -M^2}$$

Figure 3.4: The normalization condition for the bound state BSA as in Fig. 3.1. In Rainbow-Ladder, the interaction kernel does not depend on the total momentum; therefore, the differential in the second summand with respect to P^2 vanishes.

total momenta are always held constant at the pole mass, $Q^2 = -M^2$. Schematically, the full normalization condition in momentum space reads (Dirac-, colour-, flavour and Lorentz-indices are implicit)

$$1 = \frac{d}{dP^2} \Big|_{P^2 = -M^2} \text{tr} \int_q \left\{ \left(\bar{\Gamma}(-Q, q) S(q_+) \Gamma(Q, q) S(q_-) \right) + \int_q \int_l \left(S(L) \bar{\Gamma}(-Q, l) S(l_+) K(P, l, q) S(q_+) \Gamma(Q, q) S(q_-) \right) \right\} \Big|_{Q^2 = -M^2} \quad (3.35)$$

and is universal for all two-quark BSAs.¹ In Rainbow-Ladder truncation, the kernel K is independent of P and vanishes in the differential, so that we do not have to consider the second two-loop integral. We trace over all Dirac-, colour and flavour indices. From the meson properties (colour \otimes flavour structure), it follows that the product of N_c and N_f occurs as a global prefactor. With the charge conjugation matrix $C := \gamma_0 \gamma_2$, the required conjugate amplitude $\bar{\Gamma}(Q, q)$ for $J = 0$ and $J = 1$ BSAs is defined by

$$\bar{\Gamma}(Q, q) := C \Gamma^T(Q, -q) C^T \quad ; \quad \bar{\Gamma}^\mu(Q, q) := C \Gamma^{\mu T}(Q, -q) C^T \quad (3.36)$$

(Pseudo)Scalar mesons. When solving the (pseudo)scalar BSE in Maris-Tandy interaction, the explicit normalization condition is given by Eq. (3.35):

$$1 = \text{tr}_{\text{scf}} \frac{d}{dP^2} \Big|_{P^2 = -M^2} \int_q \bar{\Gamma}(-Q, q) S(q_+) \Gamma(Q, q) S(q_-) \quad (3.37)$$

The operator tr_{scf} denotes the trace over Dirac spin, colour and flavour indices and results from closing the loop we see in Fig. 3.4.

Choosing the basis given in Eq. (3.23), the dressing functions $F_i(p)$ are the largest in the infrared and approach zero in the high ultraviolet as we can see in Fig. 3.5, where the dressing functions of a pion are graphically displayed. This indicates already that the non-perturbative low-energy sector is particularly important for bound states of quarks

¹For $J \neq 0$ states one has to contract the occurring Lorentz indices by additional transverse projectors and divide the result by the associated symmetry factor, cf. e.g. [118].

and antiquarks. Again, as we saw by solving the quark DSE, the dressing functions mostly start to change at around Λ_{QCD} .

Once a $q\bar{q}$ BSA is normalized, it can be used to calculate observables as an ingredient of Feynman diagrams, e.g. for the electroweak decay constant f_λ . For the uncharged pion ($\lambda = \pi^0$), it describes the decay $\pi^0 \rightarrow e^+ + e^- + \gamma$. This decay is equivalent to a transition from a pseudoscalar meson to an axial-vector current and defines the leptonic decay constant by [43]

$$\langle 0 | j_5^\mu(x) | \pi \rangle = -iP^\mu f_\pi e^{-ix \cdot P}. \quad (3.38)$$

In Dirac space, the corresponding vertex is given by the axial-vector vertex $\Gamma_{5\mu} = \gamma_5 \gamma_\mu$, to which the pion BSA couples. To be more precise, evaluating the corresponding Feynman diagram yields

$$if_\pi P_\mu = Z_2 N_c \text{tr}_s \int_q \Gamma_{5\mu} S(q_+) \Gamma(P, q) S(q_-). \quad (3.39)$$

Z_2 is the quark renormalization constant and stems from the fact that f_π as an observable has to be renormalization group invariant. In our flavour space convention¹, the pion decay constant corresponds to its experimental value of roughly 93 MeV.

(Axial)Vector mesons. The normalization condition looks similar to the (pseudo)scalar case and the solution technique is the same. In this case we have to contract the kernel with a transverse projector and average over the three polarizations such that the condition is

$$1 = \text{tr}_{\text{sfc}} \frac{d}{dP^2} \int_q \frac{T_{\mu\nu}(P)}{3} \bar{\Gamma}^\mu(-Q, q) S(q_+) \Gamma^\nu(Q, q) S(q_-). \quad (3.40)$$

In Fig. 3.6 we see a plot of the dressing functions of the normalized ρ meson BSA as functions of p^2 . Like the pion BSA, the dressing functions have a characteristic value in the infrared and vanish in the ultraviolet.

With the normalized BSA, we can then calculate the leptonic decay constant as we did by treating the pion. This time, the decay vertex is a vector, γ_μ , and all Lorentz indices are contracted with a transverse projector, where an additional factor of $\sqrt{3}$ comes into play. The corresponding equation to calculate the decay constant is given by [104]

$$if_\rho m_\rho = \frac{Z_2 N_c}{\sqrt{3}} \text{tr}_s \int_q \gamma_\mu S(q_+) \Gamma^\mu(P, q) S(q_-). \quad (3.41)$$

¹The flavour matrix of the axial-vector vertex $\Gamma_{5\mu}$ is normalized; that means, it is given by the structure of Eq. (3.29), but overall divided by the factor of $\sqrt{2}$. There are other conventions with included factors of $\sqrt{2}$. Then, for example, the decay constant also increases by a factor of $\sqrt{2}$ as well and gives the discrepancy 93 vs. 130 MeV.

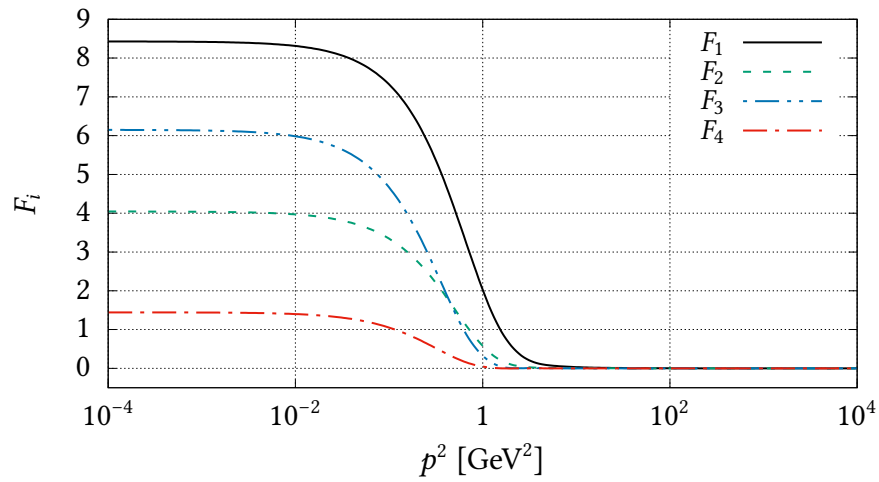


Figure 3.5: The dressing functions F_i , $i = 1, 2, 3, 4$, of the normalized pion BSA, plotted against the relative quark momentum p^2 .

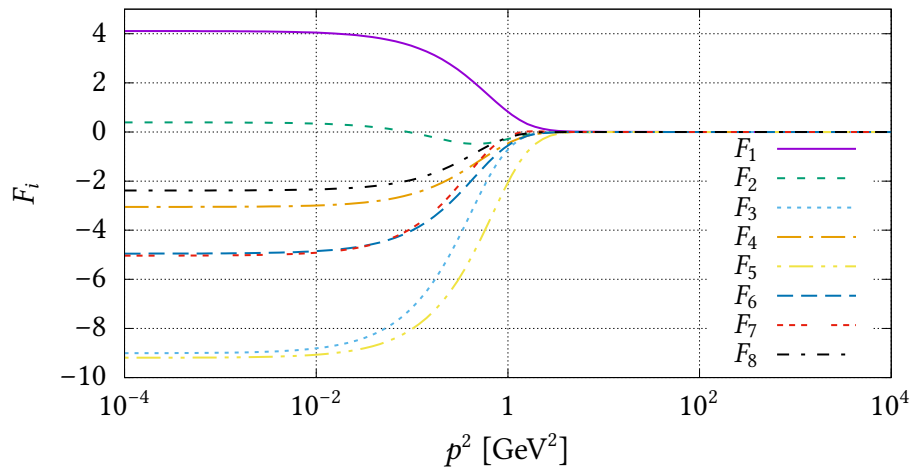


Figure 3.6: The dressing functions F_i , $i = 1, \dots, 8$, of the normalized ρ BSA, plotted against the relative quark momentum p^2 .

3.6 Diquarks

Diquarks are colour-carrying objects consisting of two quarks or two antiquarks and will become necessary as effective ingredients of states consisting of more than two quarks. Due to the non-vanishing colour, they underlie confinement and consequently cannot be measured as physical particles by experiment; but they may occur as building blocks of higher bound states. For example, baryons consisting as three-quark states can be described by a quark-diquark approximation of the three-body Faddeev equation, see Refs. [38, 118, 119]. A similar ansatz leads to the description of higher multiquark states, e.g. tetraquarks [47, 120].

The diquark and the corresponding BSA has to differ from its meson equivalent in parity due to the content: there are two quarks now instead of one quark and an antiquark. Because of this, diquark amplitudes can be constructed by using the meson ones and multiplying a charge conjugation matrix $C = \gamma^0 \gamma^2$ from the right to the Dirac part of the meson BSA, which turns an antiquark into a quark and further ensures the corresponding flip of the parity quantum number¹. Moreover, we have to correct the flavour and colour structure: We construct the diquark amplitude such that it is potentially an ingredient of higher multiquark states like baryons or tetraquarks. For us, that means the amplitude has to live in the antisymmetric colour triplet, represented by a Levi-Civita tensor ε_{ABX} . The additional index X is then the colour index of the diquark amplitude indicating the particular state within the antitriplet. Just as mesons, the diquark amplitudes also live in the flavour space: For $N_f = 2$, we have to do a case differentiation for distinct angular momentum states J^P as in the meson case, because diquarks with equal quark content underlie Pauli antisymmetry. For scalar 0^+ diquarks that means, the spins have to stand antiparallel in order to form an antisymmetric wave function, as well as the isospin, whose structure is given by the flavour singlet matrix s_{ab}^0 . For axialvector 1^+ diquarks, we get a symmetric spin, and hence, also a symmetric flavour wave function, given by the isospin triplet matrices $s_{ab}^{1,2,3}$. The matrices s_{ab}^i can be constructed by the standard representation in flavour space, $u \doteq (1, 0)$ and $d \doteq (0, 1)$ ² and are, in the $N_f = 2$ case, given by linear combinations of the three Pauli matrices, the generators of the SU(2) just as in the meson (ms) case:

$$\Gamma_{\text{dq}}^{\text{Dirac}} \otimes \Gamma^{\text{colour}} \otimes \Gamma^{\text{flavour}} = \Gamma_{\text{ms}}^{\text{Dirac}} C \otimes \varepsilon_{ABX} \otimes \begin{cases} s_{ab}^0 & J^P = 0^+ \\ s_{ab}^{1,2,3} & J^P = 1^+ \end{cases} \quad (3.42)$$

$$s^0 = |ud - du\rangle \doteq i\sigma_2 \quad s^1 = |uu\rangle \doteq \frac{\mathbb{1} + \sigma_3}{\sqrt{2}} \quad s^2 = |ud + du\rangle \doteq \sigma_1 \quad s^3 = |dd\rangle \doteq \frac{\mathbb{1} - \sigma_3}{\sqrt{2}} \quad (3.43)$$

There are other ways to choose a Dirac basis for this amplitude, but in this choice, the diquark BSE almost equals the meson BSE. This can be seen by evaluating the Feynman diagram (Fig. 3.7) – we can replace the outgoing antiquark with a quark by a charge

¹Using the Clifford algebra anticommutation relation, we see: $\mathcal{P}(\Gamma C) = \gamma^0 \Gamma \gamma^0 \gamma^2 \gamma^0 = -\mathcal{P}(\Gamma)C$.

²Optionally, one can add heavy quarks like the s and the c by extending the space to a four dimensional one. Despite the different N_f , this does *not* change the BSA overall.

conjugation of its antiparticle:

$$[\Gamma_{\text{dq}}(P, \boldsymbol{p})]_B^A = [\Gamma_{\text{ms}}(P, \boldsymbol{p}) C]_B^A = \int_q K_{DB}^{AC}(P, \boldsymbol{p}, q) [S(q_+) \Gamma_{\text{dq}}(P, q) S^T(-q_-)]_D^C \quad (3.44)$$

The kernel K is the usual one we already used in the meson BSE, but the indices B and D are switched due to the different spin line direction. Rewriting $S^T(-q_-) = C^T S(q_-) C$, multiplying the whole equation (3.44) by C_{EB} from the right and finally evaluating the colour trace entails that the meson and the diquark BSE are identical up to a factor of $1/2$, which remains as a global prefactor of the diquark BSE. Hence, the diquark amplitude is effectively given by Eq. (3.42) with

$$[\Gamma_{\text{dq}}(P, \boldsymbol{p}) C^T]_{\mathcal{A}}^B = [\Gamma_{\text{ms}}(P, \boldsymbol{p})]_B^A = \frac{1}{2} \int_q K_{BD}^{AC}(P, \boldsymbol{p}, q) [S(q_+) \Gamma_{\text{ms}}(P, q) S(q_-)]_D^C. \quad (3.45)$$

The normalization of the amplitude is analogous to the meson case, but here we have to add a symmetrization factor of $1/2$ in front of the normalization integral [121]. The replacement of an antiquark with a quark is understood implicitly.

Using Maris-Tandy interaction entails that diquarks appear as solutions of the BSE on the real axis and thus, appear as physical particles. This is a flaw of our model as it disagrees with the concept of confinement, but should not bother us further because we only investigate colourless states and not the physical properties of diquarks. The calculated masses only serve as theoretical reference values which we could use to explain physics on the level of energy arguments.

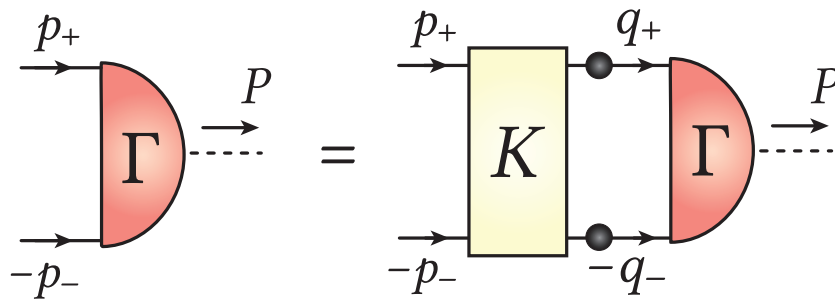


Figure 3.7: The diquark BSE as a Feynman diagram. All indices are implicit. For convenience, spin lines and momentum flow have the same direction.

[MeV]	m_π	f_π	m_ρ	f_ρ	m_σ	m_{b_1}
calculations	139.4	93.0	728.1	146.5	668.3	900.0
experiment [106]	138.5	92.6	775.3	152.7	400...550	1229.5

Table 3.1: Physical quantities of masses and decay constants resulting from the (pseudo)scalar and the (axial)vector BSEs with light quarks ($q = u/d$) when using the full tensor basis.

3.7 Two-Quark Properties in the Maris-Tandy Model

3.7.1 Full Basis

The calculated bound state properties of the π and the ρ meson reproduce the experimental values in a good approximation using the Maris-Tandy interaction model with a light quark mass of $m = 3.8$ MeV in the isospin symmetric limit. The relative deviations of the pion mass and the leptonic decay constant of the pion compared to the experimental values are smaller than 1%, which is not surprising since the model parameters are fixed on pion physics. The mass of the ρ meson and the associated leptonic decay constant however differ from the experimentally measured values with a slightly larger relative deviation. This exhibits a minor weakness of this model, although the errors are small enough to conclude that it's suitable in order to describe vector mesons. For states with opposite parity quantum numbers, namely scalar and axialvector mesons, the model shows tremendous weaknesses; in the light quark sector, the scalar $q\bar{q}$ meson and the corresponding axialvector state (known as b_1) are showing up too light. Although this is not obvious from Tab. 3.1 as the experimental σ meson is lighter than the calculated one, we expect the experimental σ not to be a $q\bar{q}$ state. It is more plausible here that the *actual* $q\bar{q}$ ground state is lying above 1 GeV instead [102, 107] – the $f_0(1370)$ may be such a candidate. Another issue of any Rainbow-Ladder bound state equation is the absence of (hadronic) decay diagrams, which is why we cannot make a statement about a strong decay width here. To be able to make these, we have to take additional BRL diagrams into account. Studies on this topic were done e.g. in [45] with BRL corrections, which lead to widths when decay terms are explicitly included. However, the ρ meson for instance gets even lighter in these approaches as it falls below 700 MeV.

3.7.2 Truncated Basis

While the solution of the BSE with a complete Dirac basis might lead to the most accurate description of the physical properties, it is conceivable that a truncated form of the basis might lead to acceptable results as well with a considerably lower effort. Comparing the solution using a full basis with truncated ones leads to statements about whether certain elements are “leading” or “sub-leading”. In this part, we will discuss this for light pseudoscalar and vector mesons as well as the consequences for future calculations in this work. The results are shown graphically in Fig. 3.8.

Pseudoscalar mesons. We find that the leading basis element is the first one, γ_5 . While the full basis leads to a pion mass of 139.4 MeV and a decay constant of 93.0 MeV, only

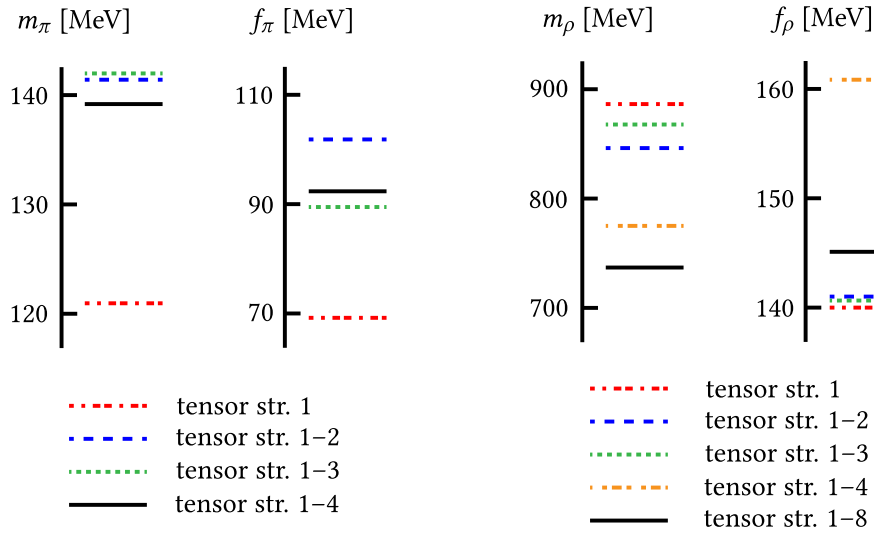


Figure 3.8: The figure shows the masses and decay constants of the π and the ρ meson for differently truncated Dirac tensor bases. We start with only include one tensor structure (red bars) and complete the bases step by step (blue, green and orange bars) until we show the values we computed by taking into account the complete bases (black bars).

taking into account the first element yields a mass of 122.3 MeV and a decay constant of 69.3 MeV. Adding only the second basis element ($\gamma_5 \not{P}$) already shifts the mass into the correct region, and further including the third element, $\gamma_5 \not{p}$, entails an accurate decay constant. The remaining element, $\gamma_5 [P, p]$, only leads to small corrections, yielding the mass and decay constant we decided about by fixing the model parameters.

Vector mesons. In vector meson calculations, we find analogous results as we did in the pseudoscalar case. The first tensor structure, γ_μ , already produces a vector meson with a mass of 887.8 MeV and a decay constant of 140.2 MeV, which is in a reasonable mass region, and the relative deviation from the values using the full basis ($m = 728.1$ MeV, $f = 146.5$ MeV) is similar to the pseudoscalar case; the decay constant is actually much less sensitive in the vector case. The inclusion of tensor structures 2–3 does not change the mass so much, but the fourth one decreases the mass significantly towards the region where we find a mass in the full model while the value of the decay constant increases. Completing the basis with tensor structures 5–8 further decreases the mass and decay constant to the values we already mentioned before.

Treatment. As we can see, the leading components of the BSAs already lead to solutions of the equations and display the physical observables in a reasonable region – for the pion, taking into account the first tensor structure γ_5 exclusively gives a relative error of 12% for the mass and 25% for the decay constant in comparison to the values we get by taking into account the full basis. We conclude that the leading order basis element is already a good approximation for the full amplitude, and therefore, as ingredients of larger diagrams,

we will use this leading order in almost any further calculation. Although a technical implementation of more than one basis element is straightforward, the inclusion of only one basis element brings tremendous simplifications into numerical calculations of higher diagrams as we will see later in chapter 4. On the other hand, meson propagators remain untouched (not approximated by a basis truncation) in those calculations because of the absence of the complex Dirac structure. This approximation corresponds to mesons as pure s -wave particles – p -wave properties are stored only in those tensor structures which explicitly depend on the relative momentum between the quarks [38].

Similar arguments hold for vector mesons; the leading component γ_μ is already yielding observables in the correct energetic region. With relative deviations of 20% for the mass and only 4% for the decay constant, we assume that only taking into account the leading tensor structure in larger diagrams will be a good approximation of the full BSA.

We expect those statements to be applicable for scalar and axialvector diquarks as well because the BSEs are essentially identical up to a factor of $1/2$ (cf. 3.6).

3.7.3 Dynamic Interaction Model

We can vary the coupling by finding different parameter sets which we fix at pion and kaon physics¹ consistently to estimate a model error in this energetic region. The parameters we vary are the light and strange quark mass (m_q, m_s) at the renormalization point, the parameter Λ and a global prefactor a in front of the infrared part of the running coupling. A variation of η in the interval [1.6, 2.0] is possible as well, but the impact on the observables is considerably small [38]. Altogether, besides the variation of the quark masses, the infrared part of the model function \mathcal{G} changes its definition as follows:

$$\mathcal{G}^{\text{ir}}(k^2, \Lambda, \eta) \rightarrow a \cdot \mathcal{G}^{\text{ir}}(k^2, \Lambda', \eta') \quad (3.46)$$

The structure of the ultraviolet part is well-determined by perturbation theory and thus, remains untouched.

The parameter sets we found for $a \in [0.8, 1.2]$ are given in Tabs. 3.2 and 3.3. The standard values for the model parameters, the ones for $a = 1.0$, which we use as the “standard parameter set” are given in the third line. As a quick crosscheck, we also show the masses of the vector mesons ρ and K^* and the ones for the scalar diquarks qq and qs as a result of the variation. We see that the “strengths” of the model – the description of pseudoscalar and vector mesons – are preserved during the variation. The ρ meson is still too light in any setup, but the overall impact on observables remains bearable, although this doesn’t necessarily need to hold for other quantum numbers or multi-quark states like tetraquarks as well. The same holds for the K^* meson. In our calculations we have to implement the dynamics for all ingredients consistently to comply with the axial-vector WTI, which preserves the effects of dynamical chiral symmetry breaking in the light quark sector.

¹Our goals are to restore an accurate pion mass m_π , decay constant f_π and kaon mass.

a	Λ [GeV ²]	m_q [MeV]	m_π [MeV]	f_π [MeV]	m_ρ [MeV]	m_{qq} [MeV]
0.8	0.78	4.2	140.6	93.0	733.0	770.7
0.9	0.74	4.0	139.8	92.7	728.3	785.2
1.0	0.71	3.8	139.4	93.0	728.1	801.3
1.1	0.68	3.6	138.5	92.7	723.9	810.4
1.2	0.66	3.5	140.1	93.4	727.2	826.4

Table 3.2: We see different variations of the Maris-Tandy coupling function, which reproduce pion physics (m_π and f_π) sufficiently well. All deviations are within the numerical error bars. Since we expect the σ meson basically to consist of two pions, all parameter sets potentially correspond to suitable effective models for describing that state. In two additional columns, the masses of the ρ meson and the scalar qq diquark for the particular parameter set are shown as well.

a	Λ [GeV ²]	m_q [MeV]	m_s [MeV]	m_K [MeV]	m_{K^*} [MeV]	m_{sq} [MeV]
0.8	0.78	4.2	82.5	499.6	934.0	1051.5
0.9	0.74	4.0	84.0	500.1	928.2	1072.7
1.0	0.71	3.8	85.5	500.3	927.7	1108.5
1.1	0.68	3.6	87.5	499.8	925.2	1126.5
1.2	0.66	3.5	89.0	500.0	929.2	1146.3

Table 3.3: We see different variations of the Maris-Tandy coupling function, which reproduce the kaon mass sufficiently well. All deviations are within the numerical error bars. In additional columns, the masses of the K^* meson and the scalar, heavy-light sq diquark for the particular parameter set are shown as well.

3.8 Pole Restrictions

Naively, one can assume that we could calculate the eigenvalue of a bound state candidate with arbitrary masses by looking for a momentum P^2 where $\lambda(P^2) = 1$ holds. In practice, the momentum range is usually restricted by the singularities of the quark propagator since it is part of the BSE integrand. Using the Maris-Tandy interaction model, there are multiple poles occurring in the timelike half plane, which restricts the total momentum P we put into the equation. Refs. [122, 123] identify some pole positions of the quark propagator in the complex plane for dynamic quark masses using the MT model, but an analytic description and the corresponding residues are still unknown – therefore, we must stick to numerical methods to avoid integrating over those poles as good as possible. If the momentum routing for the quarks using the parameter $\eta \in [0, 1]$ is given by

$$q_+ = q + \eta P \quad (3.47)$$

$$q_- = q + (1 - \eta)P \quad (3.48)$$

with $q^2 \in [0, \infty)$, we have to integrate over right-hand opened parabolas in the complex plane with their apices at

$$\begin{array}{ll} \eta^2 P^2 & \text{in the } q_+ \text{ case} \\ (1 - \eta)^2 P^2 & \text{in the } q_- \text{ case} \end{array}$$

For $\eta = 0.5$, the parabolas are equal, but if we increase/decrease the routing parameter η , one parabola shifts away from the origin of the complex plane, whilst the other parabola shifts towards it. Then, if we increase the bound state mass (\Leftrightarrow decrease the bound state total momentum squared), both parabolas shift away from the origin. Assuming that there are complex-conjugate poles up from some p_{crit}^2 with $\text{Re}(p_{\text{crit}}^2) < 0$, we are restricted by a critical value of the total momentum squared (or of the bound state mass, respectively), such that

$$P^2 \stackrel{!}{>} P_{\text{crit}}^2 \quad \text{or equivalently} \quad M < M_{\text{crit}}. \quad (3.49)$$

All this is visualized in Fig. 3.9.

Example (Pion BSE and MT interaction). The pion BSE includes two light quarks which have two complex-conjugated-symmetric poles at momenta $\text{Re}(p_{\text{crit}}^2) \approx -0.20 \text{ GeV}^2$ when using Maris-Tandy interaction with a standard parameter set (cf. section 2.2.3). A safe scenario would therefore be to set the apex of the parabola at $p^2 = -0.20 \text{ GeV}^2$. We choose symmetric momentum routing due to equal-mass constituents ($\eta = 0.5$) and get:

$$\frac{P^2}{4} > -0.2 \text{ GeV}^2 \Rightarrow P^2 > -0.8 \text{ GeV}^2 \Rightarrow M < 0.894 \text{ GeV}. \quad (3.50)$$

We see that the restricting critical mass is far above the physical pion mass and the quark poles should not interfere with our integration domain to calculate pion properties. Anyhow, we will see that for other quantum numbers or excited states, the quark poles restrict the domain heavily since the corresponding masses lie above the critical threshold.

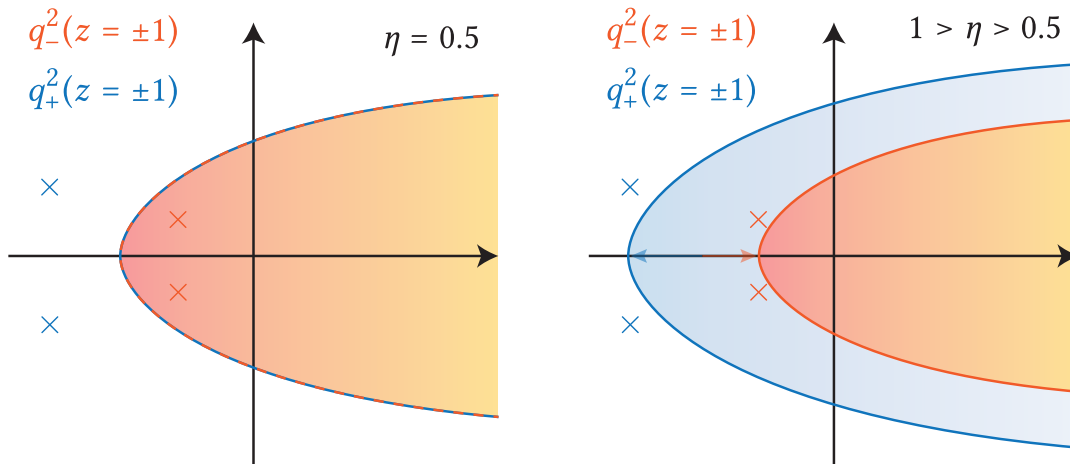


Figure 3.9: A visualization of the variation of the momentum routing parameter η for a fixed bound state mass with $M < M_{\text{crit}}$. The orange/blue dashed lines on the left panel stand for the parabolas one has to integrate over with symmetric momentum routing, $\eta = 0.5$. The orange/blue crosses denote the light/heavy Maris-Tandy quark poles. The BSE integral is defined iff the light quark poles (orange crosses) do not lie inside the interior of the orange parabola (denoted by the orange shaded region). Equivalently, the blue shaded interior (on the left panel, the blue and the orange parabolas overlap as they are identical) of the blue parabola must not include the heavy quark poles (blue crosses). One can easily see that the symmetric routing does not satisfy these conditions in this example, but there exists a choice for the momentum routing parameter $\eta > 0.5$ such that the BSE poles are excluded from the integration domains, but this is only possible up to a critical bound state mass.

General considerations. Pole restrictions will be important for the calculation of heavy-light mesons/diquarks, which may have large masses, but are restricted by light quark poles. In addition, higher bound states such as multi-quark states and other exotics are restricted as well by such a condition. The obvious strategy to calculate the heavy-lights anyway is to increase the bound state mass as far as we are able to without crossing the poles and extrapolate from this point into the desired region which is inaccessible by a direct calculation. This could be very difficult due to the amount of extrapolation efforts and leaves us with additional error bars, whose sizes depend on the extrapolation distance.

3.9 Heavy(-Light) Mesons and Diquarks

Varying the quark input makes it possible to plug in various quark masses into the BSE in order to calculate either heavier equal-mass mesons and diquarks as well as mesons and diquarks with non-equal quark content, kaons for example. First steps in calculating heavy-light mesons with heavy constituent quarks (charm, bottom) in RL truncation were done in [124], albeit without an inclusion of the lightest quarks u/d . As mentioned in the previous section, quark poles in the integration domain may cause difficulties, and the pole structure of the quark propagator in the Maris-Tandy model is not known analytically; instead, one has to apply numerical tools. Since it is a difficult challenge to perform a numerical integration over poles properly, we have (at least) three possibilities to do calculations in the heavy-light meson and diquark sector:

- We can go as far as we can without crossing the poles by varying the total momentum and momentum routing parameter. It is possible to estimate the pole positions by solving the quark propagator roughly.
- We deform the integration path of the radial integral in the meson BSE since we expect the self energy integrand to be holomorphic everywhere except for the pole locations, which the deformation circumvents by construction.
- We bring the propagator in an analytic form, e.g. by doing fits and predict the poles using sophisticated numerical methods such as the Schlessinger-Point method [125].

The first possibility restricts us to critical bound state masses and the nearer we close up to the poles, the less stable gets our numerical calculation. The second possibility requires a good knowledge about the pole positions of the Maris-Tandy quarks, which is a big challenge. The third possibility would give us an analytic structure of the quarks and thus the corresponding residues of the poles, which allows us to perform analytic integrals. Unfortunately, we have not yet found a reliable technique to bring the propagator into an analytic structure. Due to these technical issues, we proceed with the first possibility. With that, we are able to solve BSEs for various configurations of mesons and diquarks, although we might have to extrapolate the eigenvalue curve to get a solution when the mass difference of the two quarks is too large. Doing all this, the mass curves for pseudoscalar and vector mesons as well as scalar and axialvector diquarks are given in Fig. 3.10 with the heavy quark set as a charm quark with an input mass of $m_c = 795$ MeV.

Heavy-Light Two-Quark Bethe-Salpeter amplitudes

Although we are not able to solve the BSE for many heavy-light two-quark states directly on the mass shell to obtain a solution, it is still required to have knowledge about the corresponding amplitudes to be able to use them as building blocks of larger diagrams. In this thesis, this was done by a combination of fitting and extrapolating. To approach a heavy-light Qq state, we can extrapolate in two directions: from below, by raising the mass of one light quark, $qq \rightarrow Qq$ and from above, by lowering the mass of a heavy quark, $QQ \rightarrow Qq$. We evaluate specific points of the (normalized) two-quark

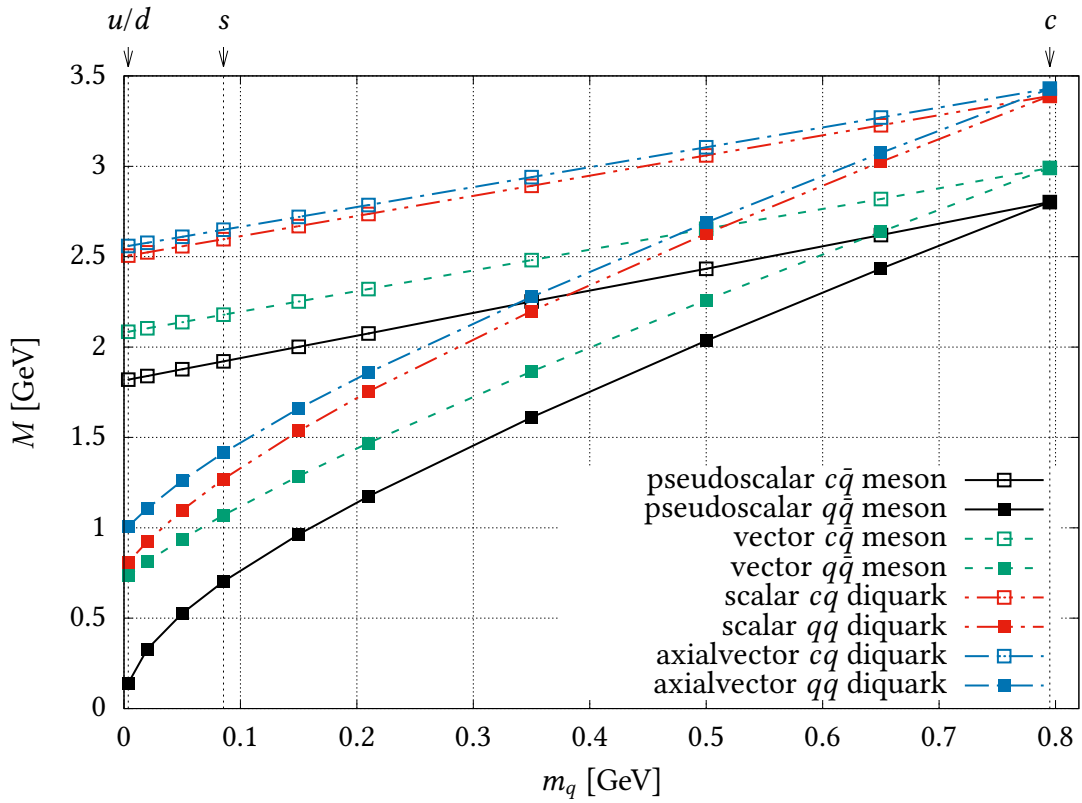


Figure 3.10: Mass curves for equal-mass (filled squares) and heavy-light (unfilled squares) two-quark states. Heavy-light meson and diquark masses may result from the extrapolation of their eigenvalue curves, but equal-quark two-quark state masses never do for these quantum numbers.

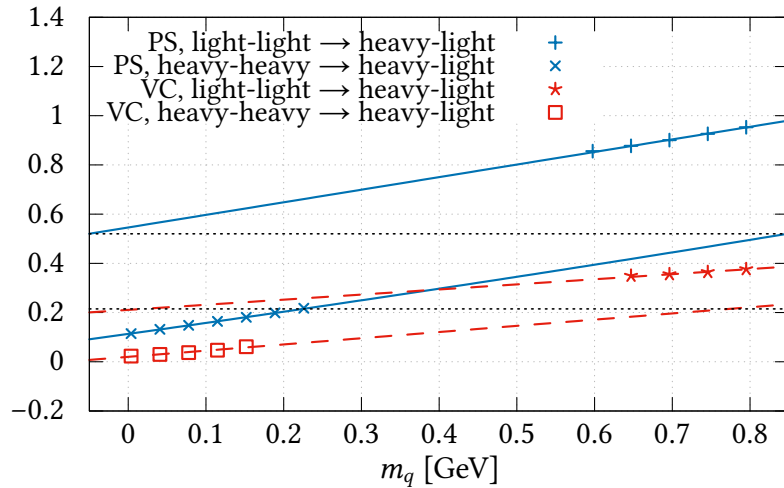


Figure 3.11: The extrapolation procedure for pseudoscalar and vector mesons taking the example of $p^2 = 5 \text{ GeV}^2$ for the leading amplitudes. The levels of the black lines correspond to the values of the heavy-light amplitudes for p^2 used in our calculations. This procedure is done for a p^2 grid to obtain amplitude shapes by using the fit function (3.51).

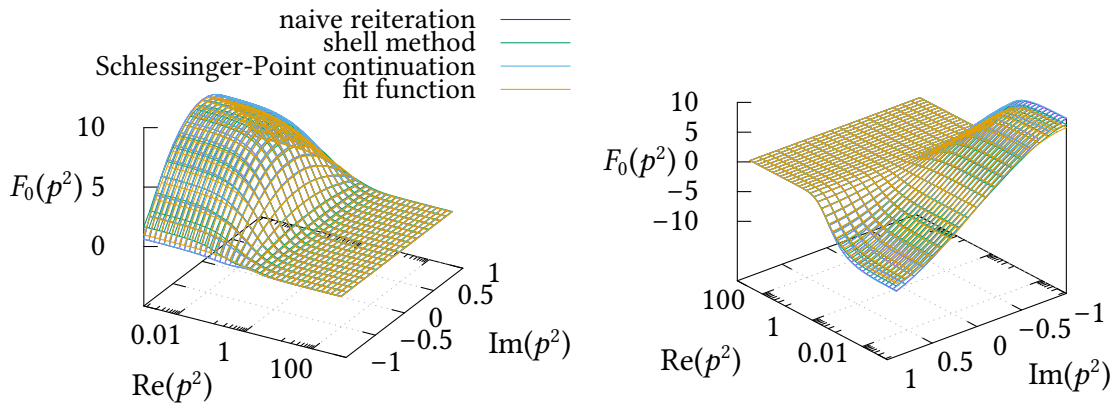


Figure 3.12: The continuation of the pion BSA into the complex plane with positive $\text{Re}(p^2)$ using different methods. On the left hand side, we see the real part of the leading pion amplitude and on the right hand side, we see the imaginary part. It is clearly visible that all of the methods lie on top of each other – the accordance is so precise that the naive reiteration curve is almost completely covered by the other ones. We conclude that it should be sufficient to implement the *cheap* fit in most practical calculations.

BSAs for certain momenta p^2 along those two paths and find fit functions such that the values of the amplitudes roughly match in the heavy-light case as seen in Fig. 3.11. The extracted value of the amplitude is then the mean of the two extrapolated values. Then, we collect those values on a specific p^2 grid and continue these functions using a fit function, Eq. (3.51), which will be discussed in the next section. For simplicity, we neglect the angular dependence of the BSA completely. Apparently, this is a good approximation if the dressing functions are flat and symmetric in the angular variable z . We found that this is mostly true, although for far-heavy-light states, the dressing functions may lose their flatness near the border points, $z \approx \pm 1$. The fact that these border points just account for a small part of the integration domain strengthens the value of our approximation.

3.10 Bethe-Salpeter Amplitudes in the Complex Plane

As BSAs are vertices occurring in loop diagrams, the relative momentum p^2 may become a complex number in a Euclidean calculation. The mass determination can be done by iterating on the real axis only, which yields the results we saw already in Figs. 3.5 and 3.6. Calculating the dressing functions in the complex plane however could be done naively just like in the quark DSE, but with the same numerical issues as we already had to deal with before, namely the integration over branch cuts in the radial integral. It is also possible to apply the already known method using “shell parabolas” to continue the amplitudes, and besides that, we can try to find an analytic continuation by finding good fit functions or using the Schlessinger-Point continuation method [125]. In terms of this thesis, we systematically compared the different methods to find a proper and efficient¹

¹efficient in terms of computation time.

way of calculating the amplitudes for complex momenta. Fig 3.12 shows the agreement between the different methods. The naive reiteration, the shell method and the analytic continuation via rational polynomials were implemented numerically, and the used fit function is given by

$$f(p^2) = \frac{1}{1 + a p^2} + b \exp(-c p^2) \quad (3.51)$$

with a, b, c as fit parameters.

The excellent agreement between different methods and the fit function in the relevant domain led to the conclusion that, if possible, fit functions will be implemented to perform calculations with occurring internal meson/diquark amplitudes. However, a caveat of using the fit function is that it's meant to give accurate results in the right half plane (the one for space-like momenta), whereas the results in the left half plane (the time-like one with a negative real part) are not trustworthy and thus, the important pole structure is not caught. If this region is required, it is a more reasonable choice to go with the shell method or the naive reiteration. In this thesis, we dynamically switch between the methods as needed.

3.11 Meson and Diquark Propagators

When calculating the bound state propagators, we distinguish again between $J = 0$ and $J = 1$ states due to the different Lorentz structure. In this section we will describe how we calculate certain bound state propagators and how we deal with them in practical calculations.

Pseudoscalar Mesons and Scalar Diquarks

The meson and diquark propagators for vanishing angular momentum near the mass shell are given by the "bare" mass pole of the bound state mass M :

$$D_{\text{on-shell}}(P^2) = \frac{1}{P^2 + M^2} \quad (3.52)$$

As ingredients of larger diagrams, in which the total meson/diquark momentum P is affected by the loop momentum, the propagators may be required in the far off-shell region as well. One can derive the expression for the bound state propagator using the self-consistent definition of the T -matrix for the interaction between two quarks,

$$T = K + K G_0 T. \quad (3.53)$$

Recalling the derivation of the Bethe-Salpeter equation where we have set the amplitudes $\bar{\Gamma}$ as the residue of the T -matrix ($T = \bar{\Gamma} D_{\text{on-shell}} \bar{\Gamma}$) at the mass pole, we are now interested in the general, off-shell bound state propagator $D(P^2)$. Plugging this into Eq. (3.53) and closing the open quark legs with an amplitude and its conjugate leads to

$$\bar{\Gamma} G_0 \Gamma D \bar{\Gamma} G_0 \Gamma = \bar{\Gamma} G_0 K G_0 \Gamma + \bar{\Gamma} G_0 K G_0 \Gamma D \bar{\Gamma} G_0 \Gamma. \quad (3.54)$$

With $M^2 n := \bar{\Gamma} G_0 \Gamma$ and $M^2 k := \bar{\Gamma} G_0 K G_0 \Gamma$, motivated by the notation in Refs. [118, 126], Eq. (3.54) simplifies to

$$D^{-1} = M^2 (nk^{-1}n - n). \quad (3.55)$$

This constitutes a two-loop integral which would have to be solved. However, we will approximate the two-loop part by the analytic functions given in [118] and shown in appendix C.

Vector mesons and axialvector diquarks

For vector mesons and axialvector diquarks we can split the propagator in a transverse part D_T and a longitudinal part D_L , which means:

$$D_{\mu\nu} = D_T T_{\mu\nu} + D_L L_{\mu\nu} \quad \text{and} \quad D_{\mu\nu}^{-1} = D_T^{-1} T_{\mu\nu} + D_L^{-1} L_{\mu\nu} \quad (3.56)$$

With the projections

$$D_T^{-1} = (nk^{-1}n)_T - n_T \quad \quad \quad D_L^{-1} = (nk^{-1}n)_L - n_L \quad (3.57)$$

we can calculate those propagators, too. For convenience [118], we set

$$(nk^{-1}n)_T = (nk^{-1}n)_L. \quad (3.58)$$

So, the full (axial-)vector (diquark/) meson propagator is given by

$$D_{\mu\nu}^{-1} = nk^{-1}n \delta_{\mu\nu} - n_T T_{\mu\nu} - n_L L_{\mu\nu} = nk^{-1}n \delta_{\mu\nu} - n_{\mu\nu}. \quad (3.59)$$

Propagator fits

Once the amplitudes are determined, the propagators can be evaluated in the complex plane via a direct calculation, but this becomes numerically expensive when they are included in larger diagrams. We found that the fit functions

$$\begin{aligned} f_{(T)}(P^2) &= \frac{1}{P^2 + M^2} + \zeta \cdot \frac{P^2 + a_1}{P^2 + a_2} + a_3 \exp(-a_4 P^2) \\ f_L(P^2) &= \frac{b_1}{P^2 + b_2} - \frac{b_3}{(P^2 + b_4)^2} + \zeta \end{aligned} \quad (3.60)$$

are a good choice to describe the calculated propagators. The variables a_i , b_i and ζ are fit parameters which describe the regular part of the propagator and M is the corresponding bound state mass. The function $f_{(T)}$ reproduces the propagator of $J = 0$ states and the transverse part of $J = 1$ ones, whereas f_L is a function proved to be a good choice for the longitudinal part of a $J = 1$ propagator. The shared parameter ζ is an asymptotic ultraviolet variable coming from the fact that the longitudinal and the transverse part of propagators of $J = 1$ states match in the far ultraviolet. With those fits, the propagators are described quite precise for momenta P^2 that satisfy $\text{Re}(P^2) > -M^2$. In terms of this thesis, that is a sufficient region because the pole structure is given analytically and we exclude integrations where we go far into the region where $\text{Re}(P^2) < -M^2$ holds.

3.12 Off-shell Meson and Diquark Amplitudes

Pseudoscalar Mesons and Scalar Diquarks

In the course of calculations based on the methods given in this chapter we solve the BSE for an on-shell $J = 0$ bound state like mesons or diquarks satisfying the condition $P^2 = -M^2$. Instead of solving the whole equation for off-shell momenta, we model the amplitude by doing two some assumptions:

- the leading amplitude is nearly unaffected by the degree of “offshellness” of the bound state and
- the subleading amplitudes are suppressed for highly off-shell momenta.

Thus, we assume that the leading amplitude stays the same and the subleading amplitudes are suppressed by an insertion of a suppressing function g . Moreover, we introduce a function h . The functions are given by [118, 126]

$$g(P^2) = M^2(P^2 + 2M^2)^{-1} \quad h(P^2) = -i \sqrt{\frac{P^2}{P^2 + 2M^2}}. \quad (3.61)$$

These functions are inserted such that every sub-leading amplitude is multiplied by g and every occurring P^μ in the basis elements is multiplied by h . So, in case of the pion BSE, the off-shell amplitude is modeled by

$$\Gamma(P, p) = \gamma_5 F_1(P, p) + gh \gamma_5 \not{P} F_2(P, p) + gh \gamma_5 \not{p} (P \cdot p) F_3(P, p) + gh \gamma_5 [\not{P}, \not{p}] F_4(P, p). \quad (3.62)$$

Crosschecking the physical point indeed leads back to the calculated on-shell amplitude:

$$g(-M^2) = 1 = h(-M^2) \quad (3.63)$$

Vector mesons and axialvector diquarks

The off-shell amplitudes of vector mesons and axialvector diquarks are also affected by the functions g and h [118]. One has to multiply a g to all subleading dressing functions again, an h to the 1st, 2nd, 3rd, 7nd dressing function and an h^2 to the 5th one. The on-shell (ax-)vector bound state propagator is forced to be transverse to the absolute momentum, whereas the off-shell one has longitudinal contributions. Omitting the transverse projections inside the basis of the calculated (on-shell) bound states, we get the general expression for the off-shell amplitude. On the mass shell, the longitudinal parts will be suppressed by a factor of $P^2 + M^2$ due to the pole in the propagator to ensure a reasonable expression for the T -matrix. As an ansatz and to ensure that the correct on-shell behaviour is reached by taking the limit $P^2 \rightarrow -M^2$, we insert the on-shell dressing functions $F_i (i = 1 \dots 8)$.

CHAPTER 4

TETRAQUARKS

Tetraquarks are exotic states consisting of a combination of two quarks and two antiquarks. As a hot topic in elementary particle physics these composite states are a subject of broad research. Due to confinement, observable (colourless) states are only possible with a $(q\bar{q}q\bar{q})$ configuration. As already mentioned in the introduction, one of the main motivations to study these kinds of bound states is the paradox mass ordering in the spectrum of light, scalar meson candidates: The isoscalar $f_0(500)$ has a lower mass than the corresponding isotriplet state, but assuming a $q\bar{q}$ structure, these states should roughly lie in the same mass region. Additionally, due to the p -wave nature enforced by the non-relativistic quark model, the mass of the isoscalar state is too small for an ordinary quarkonium – we would expect it to be heavier than the corresponding vector mesons; but apparently, this is not the case. Early on, quite basic reflections already led to the proposal that these states might not be conventional quarkonia: in the 70s, Jaffe [4] concluded first that a four-quark structure would be the solution for the “inverse” mass ordering in the spectrum of scalar mesons.

Finally, after many years of lacking experimental evidence, the observation of the $\chi_{c1}(3872)$ in 2003 engaged the attention of hadron physicists all over the world. It showed properties which disagree with the picture of ordinary charmonia and was the first and yet, most prominent candidate for a four-quark state. After that, many other of these *exotic* states were discovered. At least since the discovery of Z states (which have a non-zero electric charge), the existence of states consisting of more than a quark-antiquark pair is unquestionable.

A theoretical description of those states in the frameworks of DSEs and BSEs is ambitious. As one could have guessed, the amount of kinematic complexity is increasing exponentially with an increasing number of quarks considered. Different to the (comparably simple) meson BSE, an exact four-body equation must include every interaction between the different quarks, and a simple Rainbow-Ladder truncation on the level of two-body interactions is not respecting 3PI and 4PI scattering kernels which may occur in the bound state equation. Despite the effort which was made by solving the four-quark equation in previous works [46, 47, 91], we will stick to an approximate two-body equation in this work due to kinematic simplicity, firstly introduced in [120]. Due to its similarity to a two-body description of quark-antiquark states, we will see that it could easily be extended to the coupling of four-quark states to ordinary quarkonia, as

advertised in section 1.3.

This chapter is dedicated to the main equation which we will solve in order to obtain results in this work: the two-body tetraquark BSE. Along with a derivation from the full four-body BSE and the coupling to the two-body BSE, we will discuss the idiosyncracies and technical difficulties of the equation and point out the central differences in comparison to the four-quark BSE.

4.1 The Two-Body Equation

For bound states of four quarks in the Dyson-Schwinger/Bethe-Salpeter framework, we expect (as in the Baryon case) a homogeneous eigenvalue equation similar to the three-body Faddeev equation. To be able to derive such an equation, we start with the full four quark propagator $G^{(4)}$:

$$G^{(4)} = G_0^{(4)} + G_0^{(4)} K^{(4)} G^{(4)} \quad (4.1)$$

$G_0^{(4)}$ = SSSS is the interaction-free four body propagator and the four-body scattering kernel $K^{(4)}$ includes two-, three- and four-quark interactions, denoted by quantities with a tilde [127],

$$K^{(4)} = \tilde{K}^{(2)} + \tilde{K}^{(3)} + \tilde{K}^{(4)}. \quad (4.2)$$

In the following, we will neglect three- and four-body interactions, i.e. we set that $\tilde{K}^{(3)} = \tilde{K}^{(4)} = 0$. We do this on the basis of previous works on baryons [38, 44, 128] and tetraquarks [46, 47, 91, 120], see [129] for a mini-review, where it is argued that the quark-antiquark interactions dominate the equation over the three- or four-particle irreducible contributions. The consistent and physically meaningful results from the past decade justify this approximation. By omitting those three- and four-particle irreducible contributions, we can further distinguish between the remaining two-quark interactions of distinct quark pairs and therefore apply an index notation as follows:

$$K^{(4)} \approx \tilde{K}^{(2)} = \sum_i \tilde{K}_i^{(2)} \quad \text{with} \quad \tilde{K}_i^{(2)} = K_{rs}^{(2)} S_t^{-1} S_u^{-1} + S_r^{-1} S_s^{-1} K_{tu}^{(2)} - K_{rs}^{(2)} K_{tu}^{(2)}, \quad (4.3)$$

where $i \in \{1, 2, 3\}$ ¹. It specifies the interactions between the quarks r, s and t, u separated (first two terms) and together (last term). The negative sign results from a double-counting of the two-pair interaction kernel which could be seen by expanding G into a series and considering that independent scattering kernels commute for distinct r, s, t, u , i.e. $[K_{rs}, K_{tu}] = 0$. Based on these “subkernels” we could define four-body T -matrices and work with their self-consistent series:

$$\tilde{T}_i^{(2)} = \tilde{K}_i^{(2)} + \tilde{T}_i^{(2)} G_0^{(4)} \tilde{K}_i^{(2)} \quad (4.4)$$

¹The index i is uniquely related to an ordered configuration (rs, tu) . One can thus define a bijective function $f : \{1, 2, 3\} \rightarrow \{(12, 34), (13, 24), (14, 23)\}$.

Independent from that and by making use of the residue ansatz for a bound state amplitude (cf. section 3.1), the full four-body on-shell tetraquark BSE is given by

$$\Psi = K^{(4)} G_0^{(4)} \Psi, \quad (4.5)$$

where Ψ is the four body bound state amplitude. With that and the segmentation of the interaction kernel, Eq. (4.3), we can define “sub-amplitudes” Ψ_i ,

$$\Psi \stackrel{(4.5)}{=} K^{(4)} G_0^{(4)} \Psi \approx \sum_i \tilde{K}_i^{(2)} G_0^{(4)} \Psi =: \sum_i \Psi_i, \quad (4.6)$$

and an insertion of Eq. (4.4) yields

$$\Psi_i = \tilde{T}_i^{(2)} G_0^{(4)} (\Psi - \Psi_i) = \sum_{j \neq i} \tilde{T}_i^{(2)} G_0^{(4)} \Psi_j. \quad (4.7)$$

Now, we can plug in the two body pole ansatz $T_{rs}^{(2)} = \Gamma_{rs} D \bar{\Gamma}_{rs}$ (cf. 3.1) inside T_i with $i = (rs, tu)$,

$$\tilde{T}_i^{(2)} = T_{rs}^{(2)} \mathbb{1}_t \mathbb{1}_u + \mathbb{1}_r \mathbb{1}_s T_{tu}^{(2)} - T_{rs}^{(2)} T_{tu}^{(2)} = \Gamma_{rs} D \bar{\Gamma}_{rs} + \Gamma_{tu} D \bar{\Gamma}_{tu} - \Gamma_{rs} D \bar{\Gamma}_{rs} \Gamma_{tu} D \bar{\Gamma}_{tu}, \quad (4.8)$$

to derive a kernel including bound state amplitudes out of Eq. (4.7). Defining an effective tetraquark two-body amplitude Φ such that

$$\Psi_i =: \Gamma_{rs} \Gamma_{tu} G_0^{(2,2)} \Phi_i \quad (4.9)$$

with $G_0^{(2,2)} = DD$ and $i = (rs, tu)$, then closing the quark legs by multiplying $\bar{\Gamma}_{rs} \bar{\Gamma}_{tu} G_0^{(4)}$ from the left side leads to

$$\begin{aligned} & \left(\bar{\Gamma}_{rs} G_0^{(2)} \Gamma_{rs} \right) \left(\bar{\Gamma}_{tu} G_0^{(2)} \Gamma_{tu} \right) G_0^{(2,2)} \Phi_i \\ &= \left[\left(\bar{\Gamma}_{rs} G_0^{(2)} \Gamma_{rs} \right) D + \left(\bar{\Gamma}_{tu} G_0^{(2)} \Gamma_{tu} \right) D - \left(\bar{\Gamma}_{rs} G_0^{(2)} \Gamma_{rs} \right) \left(\bar{\Gamma}_{tu} G_0^{(2)} \Gamma_{tu} \right) DD \right] \\ & \times \bar{\Gamma}_{rs} \bar{\Gamma}_{tu} G_0^{(4)} \Gamma_{rt} \Gamma_{su} G_0^{(2,2)} \Phi_j \\ &+ \left[\left(\bar{\Gamma}_{rs} G_0^{(2)} \Gamma_{rs} \right) D + \left(\bar{\Gamma}_{tu} G_0^{(2)} \Gamma_{tu} \right) D - \left(\bar{\Gamma}_{rs} G_0^{(2)} \Gamma_{rs} \right) \left(\bar{\Gamma}_{tu} G_0^{(2)} \Gamma_{tu} \right) DD \right] \\ & \times \bar{\Gamma}_{rs} \bar{\Gamma}_{tu} G_0^{(4)} \Gamma_{st} \Gamma_{ru} G_0^{(2,2)} \Phi_l. \end{aligned} \quad (4.10)$$

Isolating Φ_i yields:

$$\begin{aligned} \Phi_i &= \left[\left(\bar{\Gamma}_{tu} G_0^{(2)} \Gamma_{tu} D \right)^{-1} + \left(\bar{\Gamma}_{rs} G_0^{(2)} \Gamma_{rs} D \right)^{-1} - 1 \right] \\ & \times \left[\bar{\Gamma}_{rs} \bar{\Gamma}_{tu} G_0^{(4)} \Gamma_{rt} \Gamma_{su} G_0^{(2,2)} \Phi_j + \bar{\Gamma}_{rs} \bar{\Gamma}_{tu} G_0^{(4)} \Gamma_{st} \Gamma_{ru} G_0^{(2,2)} \Phi_l \right] \end{aligned} \quad (4.11)$$

With Eqs. (4.6) and (4.9), this defines the full two-body tetraquark BSE, a system of coupled integral equations. Working with the Born series of the T -matrix and the two-body BSE, in which λ_{rs} is the BSE eigenvalue of the meson/diquark amplitude Γ_{rs} for

an arbitrary total momentum, entails:

$$\begin{aligned}
\Gamma_{rs} D \bar{\Gamma}_{rs} G_0^{(2)} \Gamma_{rs} &= T G_0^{(2)} \Gamma_{rs} = (K + K G_0 T) G_0^{(2)} \Gamma_{rs} \\
&= \sum_i \left(K G_0^{(2)} \right)^i \Gamma_{rs} = \left(\frac{1}{1 - \lambda_{rs}} - 1 \right) \Gamma_{rs} \\
&= \left(\frac{\lambda_{rs}}{1 - \lambda_{rs}} \right) \Gamma_{rs}
\end{aligned} \tag{4.12}$$

It follows that

$$\left(\Gamma_{rs} D \bar{\Gamma}_{rs} G_0^{(2)} \right)^{-1} = \frac{1 - \lambda_{rs}}{\lambda_{rs}} = \frac{1}{\lambda_{rs}} - 1 \tag{4.13}$$

and so, we can plug in this expression for the one-loop prefactors:

$$\Phi_i = \left[\frac{1}{\lambda_{rs}} + \frac{1}{\lambda_{tu}} - 3 \right] \left[\bar{\Gamma}_{rs} \bar{\Gamma}_{tu} G_0^{(4)} \Gamma_{rt} \Gamma_{su} G_0^{(2,2)} \Phi_j + \bar{\Gamma}_{rs} \bar{\Gamma}_{tu} G_0^{(4)} \Gamma_{st} \Gamma_{ru} G_0^{(2,2)} \Phi_l \right] \tag{4.14}$$

Specifying the quark content to $(q_1 \bar{q}_2 q_3 \bar{q}_4)$, the corresponding meson and diquark amplitudes are needed. The whole tetraquark equation can then be written as a matrix multiplication including two meson amplitudes and one diquark amplitude, where K_{ij} are quark exchange kernel elements:

$$\begin{pmatrix} \Phi_{M1} \\ \Phi_{M2} \\ \Phi_D \end{pmatrix} = \begin{pmatrix} 0 & K_{12} & K_{1D} \\ K_{21} & 0 & K_{2D} \\ K_{D1} & K_{D2} & 0 \end{pmatrix} \begin{pmatrix} \Phi_{M1} \\ \Phi_{M2} \\ \Phi_D \end{pmatrix} \tag{4.15}$$

This system of equations is shown in Fig. 4.1 as Feynman diagrams. Emphasizing the two-body structure in tetraquarks, we neglect the single two body interactions and write $\tilde{T}_i^{(2)} = -T_{rs} T_{tu}$, which has been proven to be a good approximation in previous works [126]. Then, the tetraquark BSE simplifies in the sense that the one loop diagrams in the prefactor of Eq. (4.11) vanish completely and we get

$$- \Phi_i = \bar{\Gamma}_{rs} \bar{\Gamma}_{tu} G_0^{(4)} \Gamma_{rt} \Gamma_{su} G_0^{(2,2)} \Phi_j + \bar{\Gamma}_{rs} \bar{\Gamma}_{tu} G_0^{(4)} \Gamma_{st} \Gamma_{ru} G_0^{(2,2)} \Phi_l. \tag{4.16}$$

This is a system of coupled two-loop integral equations which has to be solved. With Q as the total tetraquark momentum and p as the relative meson/diquark momentum we calculate the amplitudes $\Phi_i(Q, p)$ explicitly with the same methods as we used to solve the meson and diquark BSEs. At this point it is worth to mention that the full index structure of a tetraquark amplitude is given by

$$\Phi = \Phi_{(AB)}^{\mu\dots} \tag{4.17}$$

where $\mu\dots$ are potential Lorentz indices, coming into play for quantum numbers $J \neq 0$, and A, B are colour indices especially occurring in diquark-antidiquark amplitudes. Φ does not have a Dirac structure; it is fully carried by the attached two-quark BSAs which complete the four-body amplitudes, see Eq. (4.9).

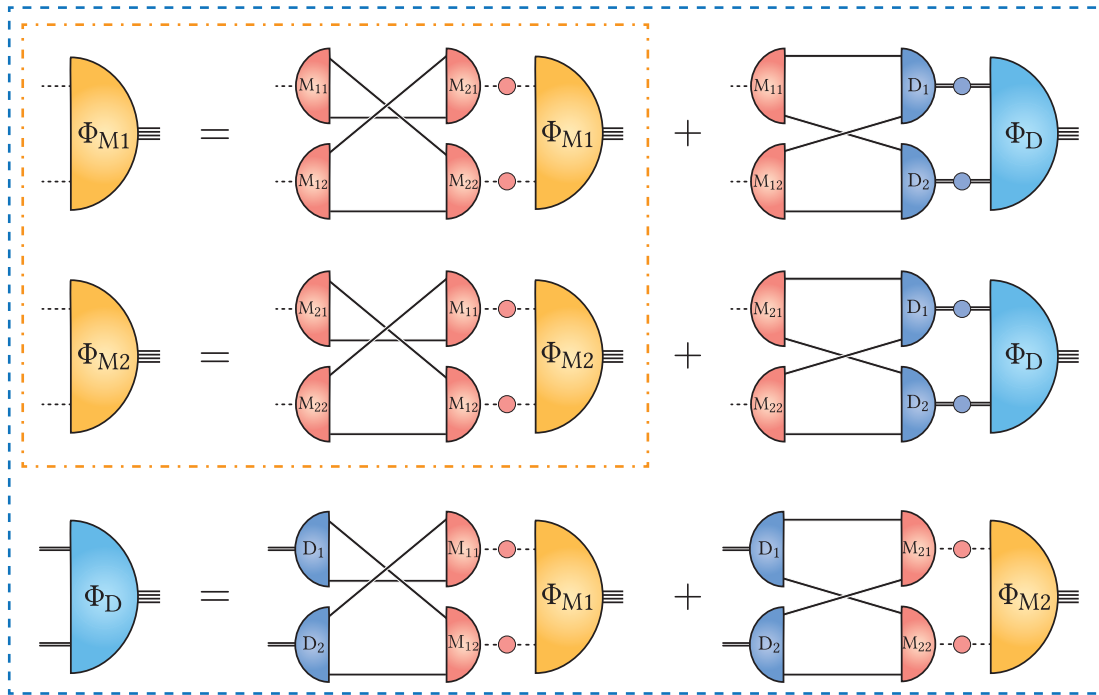


Figure 4.1: The tetraquark BSE system as Feynman diagrams. Prefactors and indices are suppressed here. M_{ij} stand for meson- and D_i for diquark amplitudes, whereas Φ_i denote the three coupled two-body tetraquark amplitudes. Continuous lines are fully dressed quark propagators, filled dots are the corresponding meson/diquark ones. The system of equations inside the blue (equidistantly) dashed rectangle represents the full BSE, the equations caught inside the orange (non-equidistantly) dashed rectangle represent the BSE with suppressed diquark contributions.

Amplitude exclusions. The two-body tetraquark BSE has an interesting feature allowing the analysis of the amplitude for identifying dominant substructures. Let's take a look at Eq. (4.15) for that, where an exclusion of all parts containing a diquark is possible. Doing this allows us – besides a comparison with the full solution – to decide whether this part is sub-dominant (which it is in case the solution does not change significantly) or not. For candidates having an experimentally observed candidate, e.g. XYZ states in the charmonium spectrum, we can do predictions for the inner structure of those. The exclusion of the diquarks is just an example – we could also exclude the M1 or the M2 component, respectively.

Comparison to the four-body equation. Although we derived the two-body equation from the four-body one, there are limitations and therefore differences which have to be discussed. In order to prevent confusion in this paragraph, we want to clarify the nomenclature: we mean the tetraquark BSEs when we talk about “four- and two-body BSEs”. Quark-antiquark or diquark BSEs however are always referred as “two-quark BSEs”, although, technically speaking, they are also “two-body” BSEs. Further details on four-quark states in the DSE/BSE framework could be found in our mini review [129].

The two-body equation relies on the information provided by the BSAs and the

occurrence of internal poles in the four-body BSA in order to describe the $q\bar{q}$ interactions. In contrast to the four-body equation, the two-body one is not suitable to describe states which do not have a structure different from clusters in $dq\bar{d}q$ or meson-meson. Therefore, compact components of tightly arranged constituent quarks will always be missing here. Technically, this is connected to the fact that the number of basis elements is highly restricted due to the enforcement of meson and diquark constituents. Moreover, after doing the two-body approximation, the inclusion of three- and four-body forces is not possible any more; viz. the equation is founded on the fact that the three- and four-body irreducible kernels are negligible.

When comparing the two- and the four-quark BSE, we have a conservation of complexities. In the four-quark equation the kinematics is more complex, but in turn, the diagrams are conceptionally simpler (especially when using RL truncation) because only one kernel type has to be specified (given that three- and four-body forces are neglected). In contrast, the two-quark BSAs and the meson/diquark propagators have to be known in the complex plane in order to be able to solve the two-body BSE.

In practice, one uses very similar truncations in both approaches on the level of the Dirac structure, which makes the solution process feasible. Whereas one omits all basis elements up to a few in the four-body equation, we only consider the leading Dirac tensor structures of the two-quark BSAs in the two-body equation. If one reduces the tensor structures of the four-body equation to the product of the leading structures we use in the two-body BSE and insert the corresponding constituent poles by hand as done e.g. in [46, 91], the truncations and therefore the results in both approaches are comparable.

Another direct consequence of the definition of the “effective” T matrices $\tilde{T}_i^{(2)}$ is that the diagonal terms of the interaction kernel of the three sub-amplitudes are non-existent. The reason for that is based on the approximation of the two-quark T matrices using the meson and diquark BSAs as pole residues, (4.8). That yields the internal occurrence of the two-quark BSAs in the four-quark amplitude, (4.9), which, through the corresponding (generally inhomogeneous) BSE absorb the diagonal two-quark kernels. This makes an isolation of only one specific component (through the exclusion of all other components) impossible – the only interactions which are not already stored in the effective amplitudes Ψ_i are quark exchanges which transition one amplitude into another.

So, again, the main difference between the equations is that one relies on the correct (off-shell) behaviour of the two-quark BSAs, which is particularly difficult to acquire and incorporate, even for simple truncations like Rainbow-Ladder.

In this work we will recalculate the properties of certain heavy-light four-quark candidates in the charmonium spectrum in order to check whether the results in both approaches agree with each other or not. An agreement would indicate consistency because the two equations start from the exact same outset, then redistribute the kinematic dynamics, get truncated similarly and meet again on the level of quantitative results. In the sector of scalar mesons this was already done in course of the pioneer work of Heupel et. al. [47, 120] who showed an excellent agreement between the methods qualitatively for the light scalars. In this work we will extend that to the comparison with the most recent results in the four-body approach [46, 91].

4.2 Quantum Numbers

Scalar tetraquarks

“The simple one”. Treating tetraquarks in the two-body formalism is, in the simplest way, possible by setting every quantum number in the calculation to $J = 0$, thus choosing pseudoscalar mesons and scalar diquarks as building blocks inside the tetraquark kernel with vanishing orbital angular momentum. That brings technical and numerical simplicity:

- There are no Lorentz contractions needed by solving the BSE.
- The tetraquark amplitude is completely scalar (up to the diagonal colour structure of the diquark-antidiquark amplitudes) and has only one basis element, the 1.
- The Dirac bases of the mesons/diquarks have the minimal number of linear independent tensor structures.

Additionally, we can go one step further by specifying only one meson type in the amplitudes. The two meson-meson amplitudes are, due to identical quantum numbers, equal up to a symmetry factor so that the three-lined bound state equation (4.15) collapses into a two-lined one:

$$\begin{pmatrix} \Phi_M \\ \Phi_D \end{pmatrix} = \begin{pmatrix} K_{MM} & K_{MD} \\ K_{DM} & 0 \end{pmatrix} \begin{pmatrix} \Phi_M \\ \Phi_D \end{pmatrix} \quad (4.18)$$

“The simple one.”

If we concentrate on the meson-only case, in which the diquark contribution is neglected, the whole tetraquark BSE collapses further into just one homogeneous equation of the meson-meson amplitude:

$$\Phi_M = K_{MM}\Phi_M \quad (4.19)$$

“The even simpler one.”

Here, K_{MM} is just a scalar integral operator, Φ_M is a function of the total tetraquark momentum Q and p is the relative momentum between the two mesons. Calculations in the past showed that the latter equation is already a good approximation for the calculation of the lightest tetraquark candidate with two pions as ingredients [120].

Non-scalar tetraquarks

The $\chi_{c1}(3872)$ – a motivating candidate. The particle known as $\chi_{c1}(3872)$, firstly detected in 2003, was originally expected to be a $c\bar{c}$ state since it is clearly located midway through the spectrum of ordinary charmonia and is uncharged without having charged isospin partners, but its quantum numbers (1^{++}) in combination with its small width do not fit into quark model predictions. Its mass, lying slightly below the DD^* threshold, and the observed decay into $D\bar{D}^*$ strongly promotes the suggestion that it could be a four-quark state with constituents $(c\bar{c}q\bar{q})$, where $q \in \{u, d\}$. Another observed decay in mesons is given by $\omega J/\psi$ [106], which also emphasizes the expected quark content and gives us an idea how to potentially set up a two-body object:

- the quark configuration is $(c\bar{c}q\bar{q})$
- a diquark-antidiquark structure is possible with $(cq, \bar{c}\bar{q})$
- meson pairs can be chosen to be $D\bar{D}^*$ and $\omega J/\psi$
- the two-body amplitudes live in the Lorentz space with
 - (1) two Lorentz indices ($D\bar{D}^*$ amplitude)
 - (2) three Lorentz indices ($\omega J/\psi$ amplitude)
 - (3) two or three Lorentz indices (diquark-antidiquark amplitude)

We can justify these numbers by taking a deeper look into the amplitude structure.

Due to the degrees of freedom in the multidimensional Lorentz space and the Lorentz contractions whilst projecting on the dressing functions, the numerical effort is much larger in this setup than it was by treating scalar tetraquarks. For technical details, I refer on appendix C.2.

General considerations. While the upper candidate, the $\chi_{c1}(3872)$, is pretty motivating from an experimental point of view, we are, within our calculations, not restricted to states which are already measured by experiment and thus, we should be able to do *predictions*. Besides experimentally observed candidates, which are generally hidden-charm objects, open-charm objects are possible ones as well, although an experimental creation of those is much more difficult. Whereas we can vary the angular momentum quantum number and the quark mass, we can also “play around” with parity and charge conjugation, determining a whole spectrum of pure four-quark states resulting from Bethe-Salpeter calculations. An aim of this thesis is to perform those calculations and to investigate how specific states are structured. For hidden charm states in the charmonium sector, it will be also interesting to see how the states are mixing with ordinary charmonia, which we are able to calculate from the corresponding two-quark Bethe-Salpeter equations. In the end, those are, besides the two-body meson-meson / diquark-antidiquark components, also just components of the full Bethe-Salpeter amplitude, which we can switch on and off to investigate whether this it plays an important role within the full description or not.

4.3 Amplitude Construction

The full tetraquark amplitude Ψ as the four-quark-meson vertex lives in the Dirac, colour and flavour space, carrying four Dirac, four colour and four flavour indices. With momentum conservation at the vertex, it depends on four momenta in total. Without loss of generality, we consider the total tetraquark momentum Q and three independent, relative quark momenta $q_{1,2,3}$; any other momentum appearing in the equation can be written as a linear combination of the four given momenta. The number of Lorentz indices depends

on the angular momentum of the four-quark state. So, we can write down the amplitude in general as

$$\left[\Psi^{(\mu\dots)}(Q, q_1, q_2, q_3) \right]_{\alpha\beta\gamma\delta,abcd,ABCD} = : \left[\Psi^{(\mu\dots)}(Q, q_1, q_2, q_3) \right]_{ABCD}, \quad (4.20)$$

where we introduced calligraphic superindices to shorten the expressions. Traces are then performed simultaneously by closing the diagrams.

Without loss of generality, we combine two two-quark bound state amplitudes in the following way to build up the four-quark amplitude:

$$\begin{aligned} & \left[\Psi^{(\mu\dots)}(Q, q_1, q_2, q_3) \right]_{ABCD} \\ & \sim \Gamma_{1,AB}^{(\rho\dots)}(q_+, q_1) \Gamma_{2,CD}^{(\sigma\dots)}(q_-, q_2) D_1^{(\rho\dots\alpha\dots)}(q_1) D_2^{(\sigma\dots\beta\dots)}(q_2) \Phi^{(\mu\dots\alpha\dots\beta\dots)} \left(Q, \frac{q_1 + q_2}{2} \right) \end{aligned} \quad (4.21)$$

We see that the Dirac, colour and flavour structure is now stored inside the two-quark amplitudes, whereas the two-body tetraquark amplitude only carries a Lorentz structure, if indeed¹, along with scalar dressing functions. Though, the diquark-antidiquark amplitude is an exception: in that case, the corresponding diquark-antidiquark two-body amplitude has a diagonal colour structure. This is because diquarks are never colourless, therefore cannot live in a colour singlet and always carry a colour index by themselves.

Quantum numbers

The tetraquark is characterized by the quantum numbers isospin I , angular momentum J , parity P and charge conjugation C , usually summarized by the notation

$$I(J^{PC}). \quad (4.22)$$

Whereas the angular momentum is connected to the number of Lorentz indices, we want to focus on isospin, parity and charge conjugation transformation in the following.

Isospin. If light quarks (u/d) are involved, the isospin quantum number is determined by well-chosen coefficients of the linear combination of possible compositions. Treating a heavy-light $Q\bar{Q}q\bar{q}$ tetraquark with $q = u/d \neq Q$, the isospin is determined by the flavour structure of the $q\bar{q}$ part – the mesonic clusters as well as the diquarkonic ones have to show the correct structure by extracting the $q\bar{q}$ flavour wave function. A construction of

¹As in case of the four-quark amplitude, that depends on the angular momentum.

an uncharged $Q\bar{Q}q\bar{q}$ with isospin I has the following flavour wave function:

$$\Psi_{abcd}^{[Q\bar{Q}q\bar{q}],I} \sim \sqrt{2} \begin{pmatrix} 0 & & \\ & 0 & \\ & & 1 \end{pmatrix}_{ab} \begin{pmatrix} 1 & 0 \\ 0 & (-1)^I \\ & & 0 \end{pmatrix}_{cd} \quad (4.23)$$

$$= \sqrt{2} \left[\begin{pmatrix} 0 & & \\ 0 & 0 & \\ 1 & 0 & \end{pmatrix}_{ac} \begin{pmatrix} 0 & 1 \\ 0 & 0 \end{pmatrix}_{db} + (-1)^I \begin{pmatrix} 0 & 0 \\ 0 & 1 \end{pmatrix}_{ac} \begin{pmatrix} 0 & 0 \\ 0 & 1 \end{pmatrix}_{db} \right] \quad (4.24)$$

$$= \sqrt{2} \left[\begin{pmatrix} 0 & & \\ 0 & 0 & \\ 1 & 0 & \end{pmatrix}_{ad} \begin{pmatrix} 0 & 1 \\ 0 & 0 \end{pmatrix}_{cb} + (-1)^I \begin{pmatrix} 0 & 0 \\ 0 & 1 \end{pmatrix}_{ad} \begin{pmatrix} 0 & 0 \\ 0 & 1 \end{pmatrix}_{cb} \right] \quad (4.25)$$

Expression (4.23) is the flavour structure with focus on the $[Q\bar{Q}]/[q\bar{q}]$ clusters, and (4.24/4.25) are the ones for the $[Q\bar{q}]/[q\bar{Q}]$ and the $[Qq]/[\bar{Q}\bar{q}]$ compositions. Factors of $\sqrt{2}$ come into play due to flavour space conventions applied by inserting the two-quark amplitudes. The upper decomposition also shows that isospin violating decay diagrams drop out algebraically. States without light quark contributions do not carry an isospin and thus, there is nothing to care of them.

Parity. At first, we recall the parity transformation matrix

$$\Pi := \text{diag}(1, -1, -1, -1) \quad (4.26)$$

which was already defined in course of the parity transformations of two-quark BSAs, see Eq. (3.22). With this, by parity transforming the bound state amplitude, the Dirac structure as the tensor product of two two-quark BSAs is transformed individually via the parity transformation matrix γ_0 . As a transformation in the Poincaré group, the parity transformation matrix also acts on the tetraquark amplitude itself for any external Lorentz index. Furthermore, it acts on any momentum on which the amplitude depends. We suppress the colour and flavour structure here, because it is not affected by parity transformations:

$$\begin{aligned} [\Psi^{(\mu\dots)}(Q, q_1, q_2, q_3)]_{\alpha\beta\gamma\delta}^P &\sim (-1)^L (\gamma_0 \Gamma_1^{(\rho\dots)}(\Pi q_+, \Pi q_1) \gamma_0)_{\alpha\beta} (\gamma_0 \Gamma_2^{(\sigma\dots)}(\Pi q_-, \Pi q_2) \gamma_0)_{\gamma\delta} \\ &\times D_1^{(\rho\dots\alpha\dots)}(\Pi q_+) D_2^{(\sigma\dots\beta\dots)}(\Pi q_-) \\ &\times \Pi^{\mu\nu} \Phi^{(\nu\dots\alpha\dots\beta\dots)}(\Pi Q, \Pi q) \end{aligned} \quad (4.27)$$

Charge conjugation. The charge conjugation is done in an equivalent way as the parity transformation. We have to conjugate the two-quark amplitudes (the transposition acts on Dirac, colour and flavour); finally, we have to reverse the relative momentum between the tetraquark constituents and interchange quarks of indistinguishable quark pairs. The following transformation holds for $[Q\bar{q}]/[q\bar{Q}]$ clusters; for other clusters we

have to adapt the different index distribution.

$$\begin{aligned}
[\Psi^{(\mu\dots)}(Q, q_1, q_2, q_3)]_{\alpha\beta\gamma\delta}^C &\sim \left(C \left[\Gamma_2^{(\sigma\dots)}(q_-, -q_2) \right]^T C^T \right)_{\alpha\beta} \left(C \left[\Gamma_1^{(\rho\dots)}(q_+, -q_1) \right]^T C^T \right)_{\gamma\delta} \\
&\times D_1^{(\rho\dots\alpha\dots)}(-q_-) D_2^{(\sigma\dots\beta\dots)}(-q_+) \\
&\times \Phi^{(\mu\dots\alpha\dots\beta\dots)}(Q, -q)
\end{aligned} \tag{4.28}$$

Choice of basis elements

The challenge is to set appropriate conditions for the basis elements of the two-body amplitudes Φ . So, to get the correct quantum numbers, we apply the corresponding transformations on the full amplitude Ψ and demand that Φ ensures the correct quantum numbers.

Example: The $\chi_{c1}(3872)$ candidate. For the $\chi_{c1}(3872)$ candidate (quantum numbers 1^{++}), the wave functions are schematically constructed from the following building blocks, which are partially¹ motivated from leading decay channels:

- (1) D and D^* mesons (and the appropriate antimesons) to guarantee an uncharged object:

$$\Psi^{D,D^*} = D^0 \bar{D}^{*0} + D^{*0} \bar{D}^0 + D^+ D^{*-} + D^{*+} D^-$$

- (2) ω and J/ψ :

$$\Psi^{\omega, J/\psi} = \omega J/\psi$$

- (3) for diquarks, we choose a combination of an axial-vector and a scalar one:

$$\Psi^{\text{Ax Sc}} = \text{Ax} \bar{\text{Sc}} + \text{Sc} \bar{\text{Ax}}$$

Imposing the symmetry conditions resulting from the positive parity condition, we get the following bases:

$$\begin{aligned}
\Phi_{\mu\nu}^{D\bar{D}^*}(Q, q) &\sim (\{ q_\mu^T \} \times \{ Q_\nu, q_\nu \}) \cup \{ T_{\mu\nu} \} \\
\Phi_{\mu\nu\rho}^{\omega, J/\psi}(Q, q) &\sim \{ \varepsilon_{\mu\nu\rho\sigma} \} \times \{ Q^\sigma, q^\sigma \} \\
\Phi_{\mu\nu}^{\text{Ax Sc}}(Q, q) &\sim (\{ q_\mu^T \} \times \{ Q_\nu, q_\nu \}) \cup \{ T_{\mu\nu} \}
\end{aligned}$$

Each basis element already corresponds to an eigenstate of the charge conjugation operator. To specify specific quantum numbers, one has to impose the corresponding even- or oddness of the product of each single basis element and its attached dressing function. The multiplication of a scalar product ($Q \cdot q$) is possible as well to enforce the amplitudes to be either even or odd. As in the two-quark meson/diquark case, this is just cosmetic and has does not affect the solution, since those prefactors get absorbed in the BSAs.

¹Obviously, there is no decay channel for diquarks and antidiquarks due to confinement.

4.4 Poles and Thresholds

The two-body tetraquark BSE includes many poles, which could turn out to be problematic in order to solve integrals numerically. A kernel expression K as used e.g. in Eq. (4.15) involves four quark- and two meson or diquark propagators. We choose a momentum routing where the relative momenta between the quarks of the internal two-quark BSAs don't depend on the total momentum of the tetraquark, see appendix C.2.

Quarks. As a result, all quark propagators inside the quark exchange diagram have a momentum dependence which can be written as

$$S(f(q, p, l) \pm Q/4) \quad (4.29)$$

With that, the quark dressing functions $\sigma_{v,s}$ carry a squared momentum argument like

$$\sigma_{v,s}(\dots - M^2/16), \quad (4.30)$$

where $M^2 = -Q^2$ is the squared tetraquark mass. Doing similar considerations as in Sec. 3.8, we come to the conclusion that the tetraquark input mass is restricted by quark poles as given in Tab. 4.1 (where m_q is the mass of the lightest quark in the system and $M < M_{\text{crit}}$).

Mesons and Diquarks. Besides quarks, there are also diquark and meson poles occurring in the equation. Usually, the mesons are the lightest subclusters and restrict the tetraquark mass the most, even stronger than the quark poles. The calculation of the critical mass from these is straightforward with m as the mass of the lightest meson/diquark in the equation:

$$M < M_{\text{crit}} = 2 \cdot m \quad (4.31)$$

For internal pions as lightest subclusters, we get a critical mass of 0.28 GeV; a ρ would lead to 1.5 GeV. This relation holds universally since we use a symmetric momentum routing between the two mesons/diquarks for a good reason: Another routing would propagate into the quark loop and forces us to know the dressing functions of the meson and diquark amplitudes in the complex relative momentum plane. While this is feasible for amplitudes which we can calculate directly, see Sec. 3.10, it is a vague endeavour to do so for highly heavy-light amplitudes, which we have to extrapolate already on the real axis.

m_q [MeV]	M_{crit} [GeV]
3.8	2.0
85.5	2.8
795.0	7.0

Table 4.1: Critical tetraquark input masses M_{crit} dependent on m_q , the mass of the lightest quark in the system from quark poles. Note that these are usually not the *real* threshold masses as described further in the text.

4.5 Quarkonium Mixing

It is nice to see how observables like the mass or the inner structure can be investigated by using the pure two-body tetraquark BSE, but as specific four-quark candidates are lying in the middle of quarkonium mass spectra, it would indeed be even more impressive to open up the possibility of a mixing between two- and four-quark states. This requires an extension to the two-body ansatz we already used to set up a BSE. With the two-body meson BSE, we have the possibility to calculate the amplitudes of quarkonia straightforwardly – the task then is to insert them sophisticatedly into the ansatz, which is the main content of this section. The derivation in this section is based on a phenomenological insertion as we will see later and thus, is not motivated from first principles. Such a derivation would have to be performed e.g. like it was done in [130] for a single-component relativistic scalar field theory. However, as argued by the authors, the generalization to theories with a condensed vacuum (like QCD) is quite an involved task.

***T*-matrix extension.** We recall the ansatz for the four-body T -matrices T_i we used to derive¹ the two-body tetraquark BSE with similar symbolic quark indices 1, 2, 3, 4:

$$T_i = T_{rs}^{(2)} \mathbb{1}_t \mathbb{1}_u + \mathbb{1}_r \mathbb{1}_s T_{tu}^{(2)} - T_{rs}^{(2)} T_{tu}^{(2)} \quad (4.32)$$

A mixing with ordinary quarkonia is only possible if at least two quarks have the same flavour. The idea is now to include an expression for the T matrix including two-quark interactions for a possible bound state of a quark and an antiquark.

We use the self consistent equation of motion of the $q\bar{q}$ T matrix,

$$T = K + KG_0 T, \quad (4.33)$$

which is equivalent to

$$T = (1 - KG_0)^{-1} K, \quad (4.34)$$

and extend the T -matrix ansatz by the following term:

$$T_i^{2q} = K_{rs}^{(2)} K_{tu}^{(2)} S_{st} G_0^{(2)} \left[(\mathbb{1} - KG_0)^{-1} K \right]_{ru} G_0^{(2)} S_{st} K_{tu}^{(2)} K_{rs}^{(2)} \quad (4.35)$$

Due to the loss of definite information by using symbolic quark indices r, s, t, u , the idea is graphically sketched in Fig. 4.2. From the T -matrix definition we can read off the structure of the corresponding sub-amplitude and write down this part of the full amplitude Ψ in the following way, where Γ^* is the pure quark-antiquark BSA, ensuring the correct quantum numbers.

$$\Psi^{2q} = K_{rs}^{(2)} S_{st} K_{tu}^{(2)} G_0^{(2)} \Gamma^* \quad (4.36)$$

Performing equivalent steps as done in deriving the two-body tetraquark BSE leads to three ‘new’ types of kernel expressions occurring within the mixed BSE among the already known quark exchange kernel from the two-body tetraquark BSE – one kernel expression, with which four-quark states transition into two-quark ones and vice versa

¹We omit the tilde over T_i from here on.

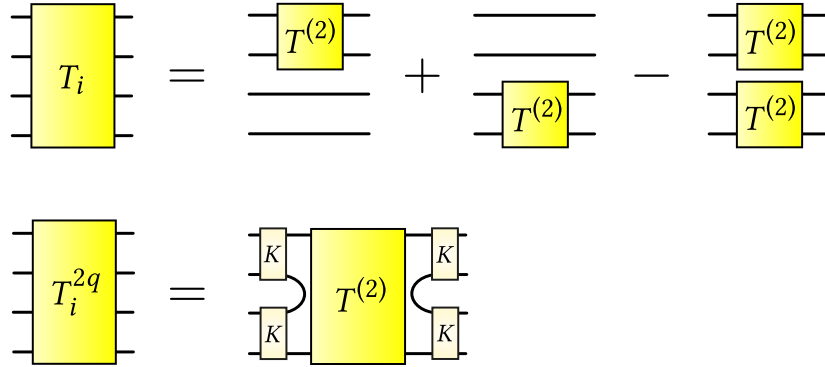


Figure 4.2: The figure graphically shows the definition of the T matrices. The first line shows the T matrices we already used by deriving the two-body tetraquark BSE, whereas the second line corresponds to a two-quark contribution to be able to mix four- and two-quark states with each other. The index i is symbolic for the possible permutations. For the sake of readability, quark propagators are implicit in this figure.

for the other kernel type. A fourth kernel type, the transition from a two-quark to another two-quark state, also comes into play and is basically given by the two-quark interaction, e.g. via Rainbow-Ladder.

Going into detail, the kernels are enumerated in the following:

- (1) An amplitude $\Phi^{4\text{-quark}}$ transitions into an amplitude $\Phi^{4\text{-quark}}$:

$$K^{4 \rightarrow 4} = -\bar{\Gamma}_{rs} \bar{\Gamma}_{tu} G_0^{(4)} \Gamma_{rt} \Gamma_{su} \quad (4.37)$$

We know this one already from the two-body tetraquark BSE.

- (2) An amplitude $\Phi^{4\text{-quark}}$ transitions into an amplitude $\Phi^{2\text{-quark}}$:

$$K^{4 \rightarrow 2} = -\bar{\Gamma}_{rs} \bar{\Gamma}_{tu} S_{st} S_r S_u \quad (4.38)$$

- (3) An amplitude $\Phi^{2\text{-quark}}$ transitions into an amplitude $\Phi^{4\text{-quark}}$:

$$K^{2 \rightarrow 4} = K_{ru} S_r S_{st} S_u \Gamma_{rs} \Gamma_{tu} \quad (4.39)$$

- (4) An amplitude $\Phi^{2\text{-quark}}$ transitions into an amplitude $\Phi^{2\text{-quark}}$:

$$K^{2 \rightarrow 2} = K_{ru}^{(2)}, \quad (4.40)$$

where $K_{ru}^{(2)}$ is the interaction that binds the quarks r and u together to build up the two-quark state – in the simplest case, this is a RL truncated interaction.

The appropriate expressions occurring within the mixed BSE are sketched as Feynman diagrams in Fig. 4.3. This provides a completely new tool to investigate mixings between

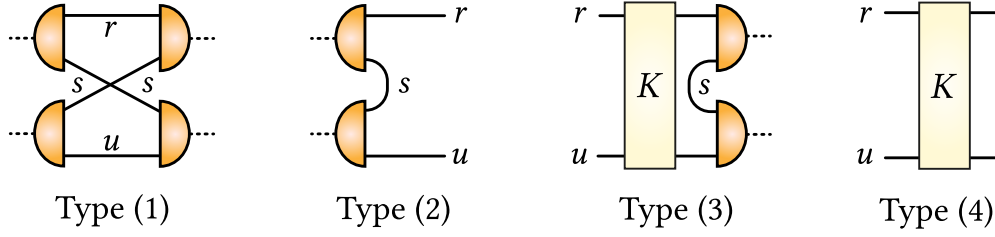


Figure 4.3: The four kernel types occurring in the mixed BSE with one quarkonium component included. Type (1) is the already known quark exchange kernel from the pure two-body tetraquark BSE, types (2) and (3) are mixing kernel diagrams coming into play by including the quarkonium component and type (4) is the ordinary two quark interaction, e.g. a Rainbow-Ladder based one.

two- and four-quark states in the Dyson-Schwinger/Bethe-Salpeter framework with a classical mixing equation:

$$\begin{pmatrix} \Phi \\ \Gamma^* \end{pmatrix} = \begin{pmatrix} K_{\Phi\Phi} & K_{\Phi\Gamma} \\ K_{\Gamma\Phi} & K_{\Gamma\Gamma} \end{pmatrix} \begin{pmatrix} \Phi \\ \Gamma^* \end{pmatrix} \quad (4.41)$$

As before in this work, Φ denotes tetraquark components, whereas Γ^* is the putative two-quark state. If the mixing terms K_{ij} with $i \neq j$ are considerably small, the two configurations decouple and we discard the interpretation of a mixed state.

Besides the possibility of performing calculations on this level, there are technical difficulties arising though. While it is always sufficient to only have knowledge about the two-quark Bethe-Salpeter wave function on the real axis by treating diagrams of type (1), we need those wave functions in the complex plane by doing calculations with diagrams of type (2) and (3). Furthermore, it is difficult to do calculations with heavy quarks included. A possibility here could be using the dressing function B of the inverse quark propagator to have an approximate expression for the leading BSA for pseudoscalar mesons through

$$F_0(p^2, z) \approx B(p^2)/f_0. \quad (4.42)$$

This is especially applicable when using light u/d quarks, because relation (4.42) holds exactly in the chiral limit [43]. Actually, this approach has been applied several times in the past to have an approximation of the leading pion dressing function in the complex plane, e.g. in Ref. [45]. Because of this, mixing a scalar two-quark σ with its tetraquark candidate is feasible without having to perform a deep investigation of the pole structure of mesonic wave functions in the complex plane. Especially for heavier quarks, we must apply one of the methods described in section 3.10.

A comment about irreducibility. The mixed BSE as it is shows a $q\bar{q}$ irreducible kernel as pointed out in [131]. It is important to note that this does not imply inconsistency on any level, as extensively demonstrated in [132]. An alternative form for the coupled BSE with a $q\bar{q}$ irreducible kernel, where the 2-quark kernel K in the equation of Type (3) in Fig. 4.3 does not occur, was derived in [133]. It is possible in our approach to derive the exact same equations by not inserting the T matrix in Eq. (4.35), but simply the full

two-quark propagator G ,

$$G = G_0 + G_0 K G = (1 - G_0 K)^{-1} G_0. \quad (4.43)$$

This propagator can alternatively be rewritten by using the T matrix,

$$G = G_0 + G_0 T G_0. \quad (4.44)$$

By comparing with Eq. (4.35), we merely inserted the second summand, $G_0 T G_0$, into the expression of T^{2q} . While it may be a more general approach to use G , as it is adding G_0 as a further diagram, it should be subleading since it does not bind the quarks in question together directly by gluon exchange.¹ In [132] we showed that the effects are indeed merely on a few-percent level – all physical statements remain unaffected for the states we investigate, cf. chapter 5.2. Based on this, every calculation with quarkonium mixing in this work was done using the reducible kernel (4.39), although the usage of the irreducible kernel would bring further numerical simplicity as (4.39) is only one-loop then.

Box diagrams. The attentive reader may remember the absence of diagonal elements in the two-body equation as formulated in (4.15). In chapter 4.1 it was argued that the missing diagonal terms which appear in the full four-body equation are virtually absorbed by the two-quark amplitudes. Beyond that however, one could still think of *box* diagrams where the quark exchange does not occur “diagonally” as it is the case for the interaction kernel of type (1) in Fig. 4.3, but vertically between two constituent partners of *one* configuration. The $q\bar{q}$ -inclusion effectively brings those (as of yet) missing terms into the four-quark part of the equation – internally, by substituting the two-quark part back into the four-quark BSE, the box diagrams appear. The occurrence of diagrams could be understood intuitively and was already proposed in [134]. In our formulation as given above, the quarks inside the box diagrams further exchange a gluon; this gluon vanishes if we derive the coupled system from the full two-quark propagator G instead of the T matrix, as described in the prior paragraph.

4.6 Resonances and the Complex Q^2 Plane

Path deformations. As many tetraquark candidates are expected to be resonances, one expects the T -matrix poles to lie in the complex Q^2 plane, where the width can be determined by using the kinematic relation

$$Q_\mu = (iM - \Gamma/2, \mathbf{0})_\mu. \quad (4.45)$$

As can be seen, this relation is given in the rest frame, but it can be rotated arbitrarily as long as Q^2 remains constant. Since the BSE would produce the corresponding pole at

¹We expect a putative two-quark component to be dominated by gluon exchange rather than by quark exchange. While the latter interaction is definitely possible, we discard it with clear conscience as we obtain rich $q\bar{q}$ spectra which are in impressive accordance with experimental results by not considering a quark(-antiquark) exchange as part of the scattering kernel at all.

a specific position Q^2 in the second Riemann sheet, where $\lambda(Q^2) = 1$ holds, it would be desirable to figure out the exact position in the complex plane. If the eigenvalue curve is evaluated above the threshold determined by the ingredient masses, a branch cut starts to open. Going over the threshold and evaluating the eigenvalue curve for some non-zero values of Γ is only possible by performing a suitable path deformation of the radial BSE integral, ensuring that the poles as critical points (meson/diquark and quark poles) are never hit by any propagator argument. Since the meson and/or diquark propagators include the disruptive poles which determine the threshold in the first place within the tetraquark BSE kernel with a momentum partitioning

$$q_+ = q + \eta Q \qquad q_- = q + (\eta - 1)Q, \qquad (4.46)$$

the conditions are given by

$$q_{\pm}^2 \neq -m_{\pm}^2, \qquad (4.47)$$

where m_{\pm} are the masses of the respective ingredients. Performing such a deformation and tracing the solution Q^2 back to M and Γ gives the resonance mass and width. A possible deformation and a path for the light $f_0(500)$ tetraquark candidate is given in Fig. 4.4; the analytic form of the spiral-shaped path above the two-meson threshold ($M > 2m$) with an input tetraquark mass M and width Γ is given by

$$\gamma_{M,\Gamma,m}(t) = \exp \left[-i \operatorname{sgn}(\Gamma) \cdot \pi/4 \cdot (5 + 3t) \right] \cdot \sqrt{\frac{3 + 3t}{2}} \cdot \left| m^2 + (iM - \Gamma/2)^2/4 \right| \qquad (4.48)$$

for $t \in [-1, 1]$. Furthermore, Fig. 4.5 shows the effect of the path deformation on the integration domain in the complex q^2 domain, where we see in which way the poles are bypassed. We have to keep in mind that we have to access the propagators for complex values with a real part *smaller* than $-m_{\pm}^2$, and this is the problematic domain for the propagator fits as pointed out in section 3.11. However, the region closely around $q_{\pm}^2 = -m_{\pm}^2$ is dominated by the bound state pole and thus, numerically induced deviations are a manageable issue.

The branch cut (blue, solid path in Fig. 4.4) is described by the divergence criterion $q_{\pm}^2 = -m_{\pm}^2$. For these values of q^2 , the corresponding angular integral in the BSE has at least one point in the respective domain, where the kernel diverges because we hit a bound state pole. Of course, integrals like this cannot be solved numerically and might lead to non-removable singularities in the complex q^2 plane. The deformed path exploits the fact that the branch cut has an opening and thus, is going through this opening to be continued to $q^2 \rightarrow \infty$ in a certain way. One has to note at this point that there are additional branch cuts coming from the quark propagator and excited states of mesons and diquarks, but these occurrences are mostly irrelevant for the calculations in this thesis; they show up only at masses far above the expected resonance masses M .

Note that the path given in Eq. (4.48) is not unique – other paths are possible as well, e.g. the one used in [45]. While our proposed path resolves a weakness¹ of the one in the

¹The referred path crosses the cut when the tetraquark input mass is very close to the threshold. This merely leads to small numerical artefacts in just a very small region, such that the two paths could be

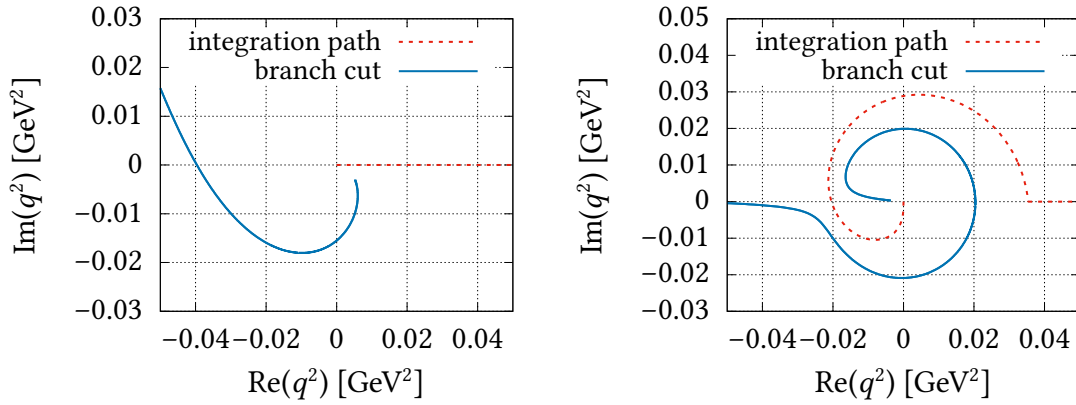


Figure 4.4: Examples for pion branch cuts and integration paths calculating the eigenvalue of the $f_0(500)$ candidate. L.h.s.: $(M, \Gamma) = (0.24, 0.3)$ GeV; a ‘normal’ integration on the real axis is possible since the mass M is lower than $2 m_\pi \approx 0.280$ GeV so that the branch cut does not cut through the positive real axis. R.h.s.: $(M, \Gamma) = (0.4, 0.01)$ GeV; the branch cut goes over the real axis and the integration path has to be deformed.

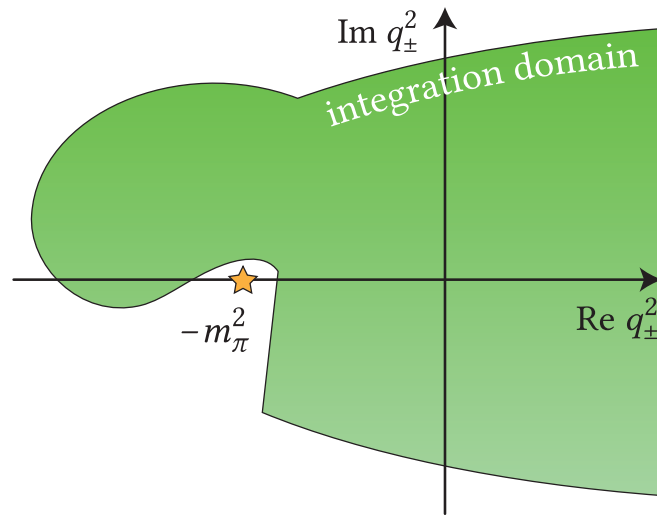


Figure 4.5: A visualization of the integration domain in the variables q_\pm . We show the complex plane and the integration area (green) coming from the radial q^2 and the angular z integral. We see that the pole (in this example it’s a pion pole, denoted by the orange star) is never hit.

Ref. in the proximity of the two-meson threshold, we will frequently cross-check our results by changing the path.

A caveat of our path (4.48) is that the path spreads farer into the timelike half plane than it has to. For very heavy tetraquarks such as all-charm candidates this could lead to an integration region that includes the diquark poles as they are relatively much closer¹ to the meson poles for heavy systems. This is numerically unfortunate; therefore, we will use another path for the investigation of all-charm tetraquark candidates in the complex plane which we basically assume to consist of $\text{di-}J/\psi$. For the spiral-shaped part and $t \in [-1, 1]$ we use:

$$\gamma_{M,\Gamma,m}(t) = \begin{cases} -0.01 \cdot \left[1 + 500 \cdot \left(\frac{M}{2m} - 1\right)\right] \cdot (t + 1) & t < 0 \\ -0.01 \cdot \left[1 + 500 \cdot \left(\frac{M}{2m} - 1\right)\right] \cdot 6^t \cdot \exp(-i\pi t^3) & t \geq 0 \end{cases} \quad (4.49)$$

Note that this path is by far not as general and sophisticated as the one in Eq. (4.48) as it is constructed only for $\text{di-}J/\psi$ states in order to prevent additional poles from being crossed.

Analytic continuations. Our calculations are restricted to the first Riemann sheet, but poles of resonances are located in the second [135]. Although we can not evaluate eigenvalues there directly, we can predict the behaviour of the curve by continuing it analytically. For that, we use the information in the first Riemann sheet and extrapolate these values into the “interesting” area, cf. Fig. 4.6. These extrapolations could happen either via polynomial fits or by using more advanced methods, e.g. Schlessinger’s method of continued fractions (SPM) [125]. Apparently, it strongly depends on the mathematical behaviour of the function, which method is suitable and which is not. In practice, we will mostly apply the method of *sticky curves*, which will be described in the following paragraph.

Sticky Curves. Practical calculations show that a two-dimensional SPM continuation is not applicable for every eigenvalue curve in the complex plane. Technically, it is possible to bypass that problem by calculating *sticky curves*. The idea is to extrapolate to specific values (M, Γ) where $\text{Re}(\lambda - 1)$ and $\text{Im}(\lambda)$ are identical, thus “stick together”. A solution is obtained at the point where the sticky curve crosses the zero. The single points are calculated via one-dimensional continuations, e.g. for a fixed mass M in a Γ domain, as illustrated in Fig. 4.7. Note that this is not the only way do those continuations – especially for heavy-light tetraquark candidates, we will also perform the one-dimensional continuations diagonally as showed on the right hand side of Fig. 4.6. This technique is individually tailored to the problems in this work and was not used in other works, yet.

considered both as suitable for the problems of this work.

¹One can see this in Fig. 4.5. If the diquark pole is close to the left of the meson pole, it may enter the integration domain, which we should avoid absolutely.

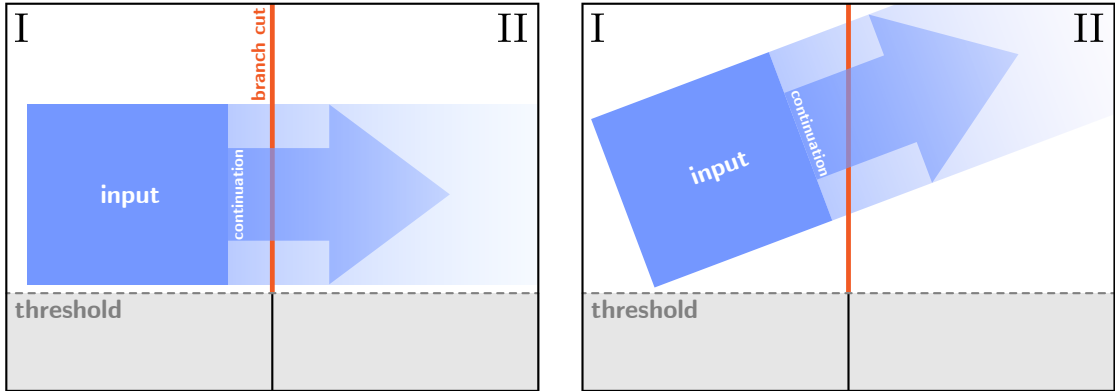


Figure 4.6: The analytic continuation procedure displayed schematically. The horizontal axis is showing the width Γ ; the vertical axis is showing the mass M . The grey dashed line is marking the threshold mass. The orange line denotes the branch cut coming into play because of the internal meson/diquark poles. Note that the branch cut is only present while “staying” in one Riemann sheet; the function is continuous when transitioning from one into the other sheet. We continue a set of input points (blue area on the left hand side) from the first to the second Riemann sheet by using a method of analytic continuation. We show two sets of input points, which provide two different views into the second Riemann sheet.

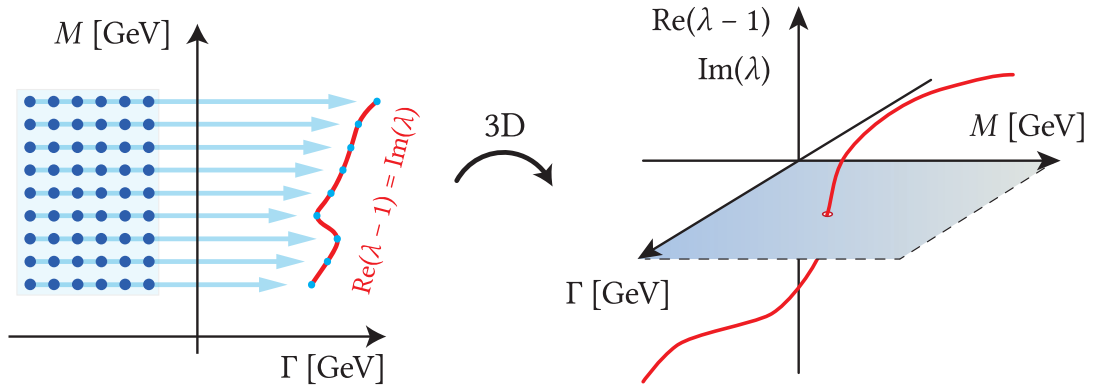


Figure 4.7: An illustration of a sticky curve and its computation. *Left panel:* Calculated input points of the eigenvalue curve (dark blue) with shadowed background. The partially transparent blue arrows and the bright blue points they point on denote one-dimensional extrapolations. The red curve is the sticky curve for which $\text{Re}(\lambda - 1) = \text{Im}(\lambda)$ holds. *Right panel:* Three dimensional illustration of the sticky curve with the eigenvalue axis as the ordinate. The non-transparent surface corresponds to $\text{Re}(\lambda - 1) = 0 = \text{Im}(\lambda)$, where the BSE is considered to have a solution, if the sticky curve crosses it.

CHAPTER 5

RESULTS

5.1 Pure Heavy-Light Tetraquarks

This section includes mass curves of calculations with pure tetraquarks in the charmonium sector. The clusterings are generally either mesonic, hadro-charmonium or diquarkonic as defined beforehand in this thesis. Furthermore, we can distinguish between hidden and open charm states. Hidden charm states are having a charm quantum number equal to zero, thus contain a $c\bar{c}$ pair internally. The quark content of a pure tetraquark with light quark contributions is then $c\bar{c}q\bar{q}$. Besides that, it is potentially possible to find open charm states, which are consequently defined to have a non-vanishing charm quantum number. Such states can be clearly distinguished from ordinary quarkonia due to their non-vanishing heavy flavour, and a mixing with an ordinary quarkonium is impossible. The quark content is set to $cc\bar{q}\bar{q}$ (or the corresponding antiparticles). Obviously, there is no possibility for the open charm state to cluster into hadro-charmonium, indicating that a separation into two mesons can only happen with heavy-light ones. This section shows, to which extent differences between those states are showing up in our calculations and which predictions we could make on that basis.

5.1.1 Hidden Charm

The hidden charm states we investigated were the following, where the meson-meson clusters are, if possible, motivated by leading decay channels of experimental states, see Tab. 5.1. The calculated mass curves are shown in Fig. 5.1 – 5.4. Dashed lines are

I	$J^{P(C)}$	exp. candidate	clusters
0	$0^{+(+)}$	–	$D\bar{D}, \omega J/\psi, SS$
1	$0^{+(+)}$	–	$D\bar{D}, \pi\eta_c, SS$
0	$1^{+(+)}$	$\chi_{c1}(3872)$	$D\bar{D}^*, \omega J/\psi, AS$
1	$1^{+(-)}$	$Z_c(3900)$	$D\bar{D}^*, \pi J/\psi, AS$

Table 5.1: The investigated quantum numbers with potential experimental candidates and the different clusterings for hidden charm tetraquarks. Diquarks are distinguished via A (axialvector) and S (scalar).

fits for the mass curve of the full setup. All errors come from extrapolations via SPM continuation.

$$I(J^{PC}) = 0(0^{++})$$

Going down the mass curve starting from an all-charm tetraquark, we see that the hadro-charmonium component is not dominant at all since switching it off doesn't do much. Switching off the diquarkonic component increases the mass in the heavy-light region slightly, and switching off the mesonic $D\bar{D}$ component leads to no solution of the BSE at all, highlighting its importance. We interpret that the tetraquark is dominated by the $D\bar{D}$ component with a small diquarkonic component consisting of two scalar diquarks. Incorporating the possibility of a tetraquark with open-strange decay channels, we get the masses

$$M_{c\bar{c}q\bar{q}}^{0(0^{++})} = 3.49(25) \text{ GeV} \quad (5.1)$$

$$M_{c\bar{c}s\bar{s}}^{0(0^{++})} = 3.69(18) \text{ GeV}. \quad (5.2)$$

$$I(J^{PC}) = 1(0^{++})$$

We see a non-negligible hadro-charmonium component for the hidden-charm $1(0^{++})$ tetraquark because switching it off increases the mass along the mass curve by almost 1 GeV consistently. Diquarks do not play a significant role here and switching off the $D\bar{D}$ component gives no solution again. This leads us to the conclusion that this tetraquark is basically dominated by the mesonic $D\bar{D}$ and the hadro-charmonium $\eta_c\pi$ component. Compared to the isoscalar equivalent discussed beforehand, this makes sense, since the included pion as a light particle favours lower-energy states. With

$$M_{c\bar{c}q\bar{q}}^{1(0^{++})} = 3.20(31) \text{ GeV}, \quad (5.3)$$

the mass is considerably smaller than the isoscalar with $M_{c\bar{c}q\bar{q}}^{0(0^{++})} = 3.49(25) \text{ GeV}$.

$$I(J^{PC}) = 0(1^{++})$$

As this tetraquark has experimental candidates for $q = u/d, s$, namely the $\chi_{c1}(3872)$ and the $X(4140)$, we have values to compare by going down the mass curve. We see that the diquarks have absolutely no influence on the mass curve at all and the hadro-charmonium component only has a negligibly small influence, which leads to the conclusion that this tetraquark is unambiguously dominated by the mesonic $D\bar{D}^*$ component. This agrees with recent four-body DSE/BSE-calculations [46] and so confirms those. At the up/down (q) and the strange (s) quark mass, our results are

$$M_{c\bar{c}q\bar{q}}^{0(1^{++})} = 3.85(18) \text{ GeV} \quad (5.4)$$

$$M_{c\bar{c}s\bar{s}}^{0(1^{++})} = 4.10(16) \text{ GeV}, \quad (5.5)$$

covering the experimental candidates $\chi_{c1}(3872)$ and $X(4140)$ pretty well within error bars. Apparently, the error bars are too large to talk about calculations on a high precision

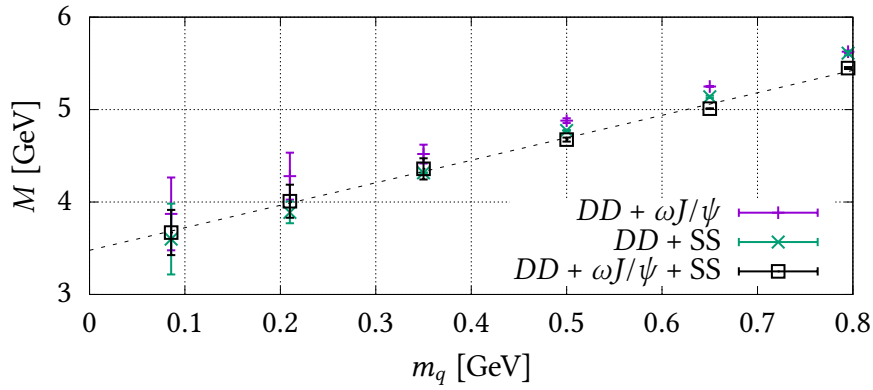


Figure 5.1: Mass curves for the $0(0^{++})$ hidden charm tetraquark.

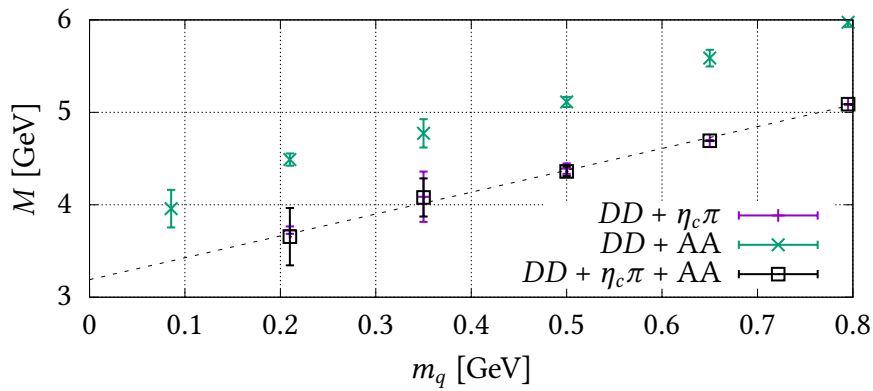


Figure 5.2: Mass curves for the $1(0^{++})$ hidden charm tetraquark.

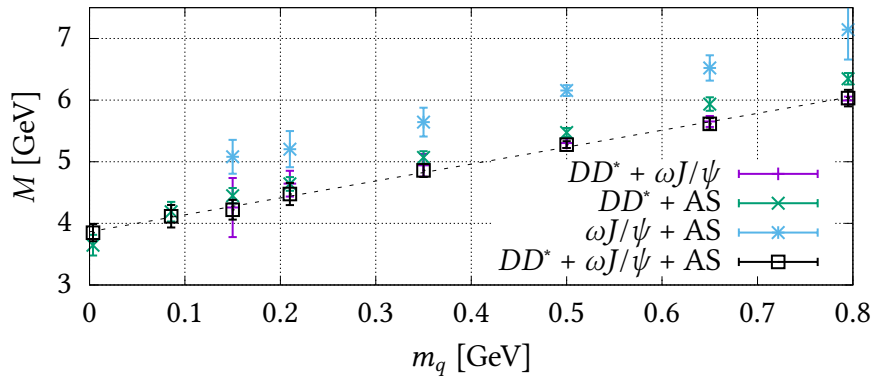


Figure 5.3: Mass curves for the $0(1^{++})$ hidden charm tetraquark.

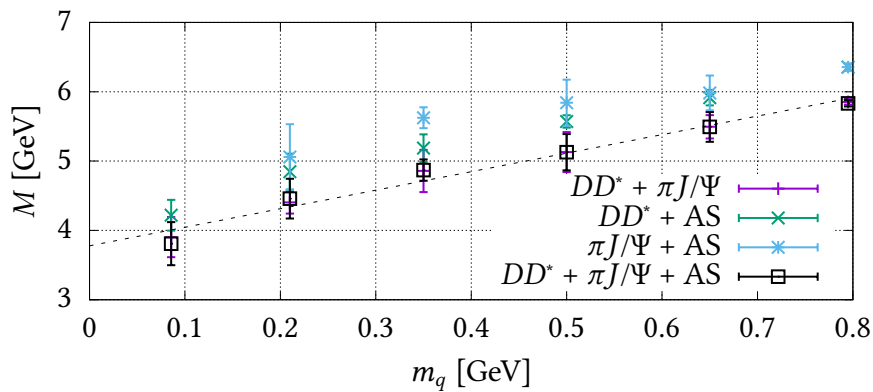


Figure 5.4: Mass curves for the $1(1^{+-})$ hidden charm tetraquark.

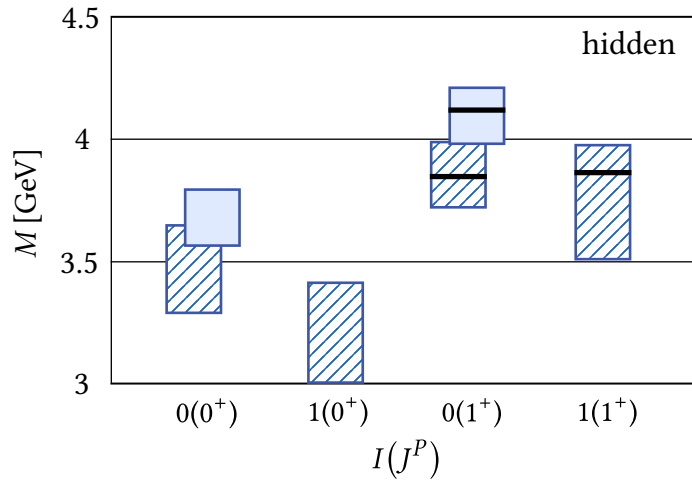


Figure 5.5: The hidden-charm tetraquark mass spectrum. Blue shaped rectangles denote the calculated results including error bars. Blue shaded rectangles denote heavy-light states with strange content, $c\bar{c}s\bar{s}$. Values for experimental candidates are given by the black bars.

level, but this inaccuracy does not transfer to the statement about the inner structure, which shows up to be mesonic ($D\bar{D}^*/D_s\bar{D}_s^*$).

$$I(J^{PC}) = 1(1^{+-})$$

With the $Z_c(3900)$ as an experimental candidate, we can again do a comparison between our calculations and the physical value from literature. With the pion as a light particle in the hadro-charmonium component, we see again, as in the scalar case, that this component gets more relevant for the state and that the overall mass decreases slightly compared to the $I = 0$ equivalent state, even though the experimental candidate does not reflect this decrease. The diquarkonic component remains unimportant over the whole mass curve and the calculated mass for light $q = u/d$ quark masses is given by

$$M_{c\bar{c}q\bar{q}}^{1(1^{+-})} = 3.79(31) \text{ GeV}, \quad (5.6)$$

which makes it possible to identify it with the experimental $Z_c(3900)$.

Summary

After all, we got a ground state spectrum of hidden charm tetraquark states for different quantum numbers, given in Fig. 5.5. The mass ordering seems natural – states with higher angular momentum are more massive than those with lower. Also, the masses of the isovector states are slightly lower than their isoscalar equivalents, and the reason for this may be the light pion being a possible ingredient. In the axialvector spectrum this disagrees with experimental results, where the isovector state is slightly heavier than the isoscalar one. Within these calculations however, it is important to point out that any statement of higher-/lower-lying states are not absolute due to the large error bars

I	J^P	exp. candidate	clusters
1	0^+	–	DD, D^*D^*, AA
0	1^+	–	DD^*, D^*D^*, AS
1	1^+	–	DD^*, D^*D^*, AA

Table 5.2: The investigated quantum numbers with potential experimental candidates and the different clusterings for open-charm tetraquarks.

we get, and this should also not be the main statement of this chapter. Instead, we focus on those about the dominance of certain substructures: The hidden-charm states seem to be strongly dominated by mesonic clusters. Heavy-light states always have a strong $D\bar{D}^{(*)}$ component, whereas the hadro-charmonium component becomes vital whenever we have isovector states. Diquarks are mostly irrelevant except for the $0(0^{++})$ case, where they seem to play a minor role.

5.1.2 Open Charm

The open charm states we investigated are displayed in Tab. 5.2 Note that, since there are always indistinguishable quarks, Pauli symmetry conditions have to be satisfied. Effectively, this reduces the amount of possible diquark clusterings. An explanation how to determine the correct diquark clusters based on the spin, colour and flavour structure of the individual diquark wave functions is given in appendix C.

$I(J^P) = 0(0^+)$

We can figure out directly that diquarks are playing a minor role here again and that mesonic contributions consisting of DD are dominant. Exchanging the DD component with D^*D^* component raises the mass significantly, letting us conclude that the DD component is *the* important mesonic component for the ground state. Since the pseudoscalar D has a lower mass than the vector D^* , this seems natural. Setting $q = u/d$ the tetraquark mass shows up to be

$$M_{cc\bar{q}\bar{q}}^{1(0^+)} = 3.214(17) \text{ GeV}. \quad (5.7)$$

Due to Pauli symmetry, it is impossible to generate a scalar/isoscalar tetraquark with a diquarkonic clustering, so we didn't focus on that one.

$I(J^P) = 0(1^+)$

Going down the mass curve here shows that diquarkonic components are irrelevant and that mesonic components dominate. As in the $1(0^+)$ case, the mesonic component (here: $D\bar{D}^*$) seems to be more important for the state than the D^*D^* component; the corresponding D^*D^* masses show up to be at order 6–10 GeV and therefore are way too heavy for being a significant component of the ground state. The masses for $q = u/d, s$

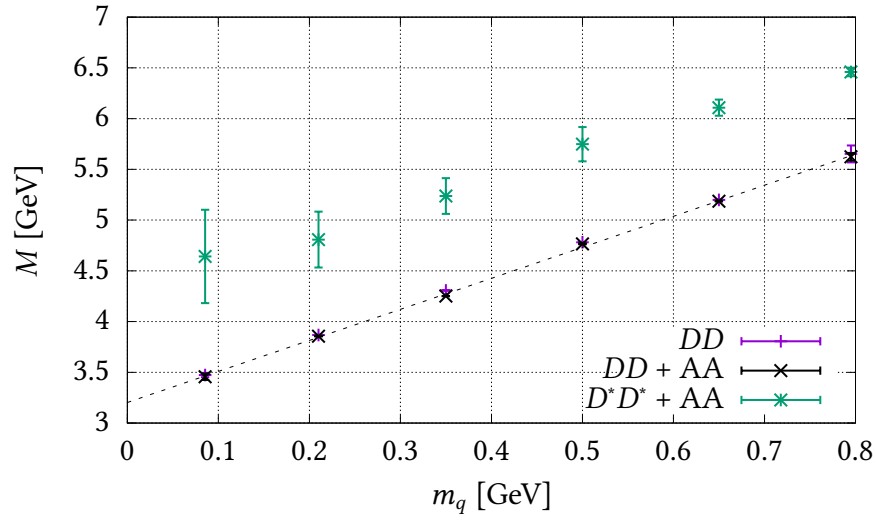


Figure 5.6: Mass curves for the $1(0^+)$ open charm tetraquark.

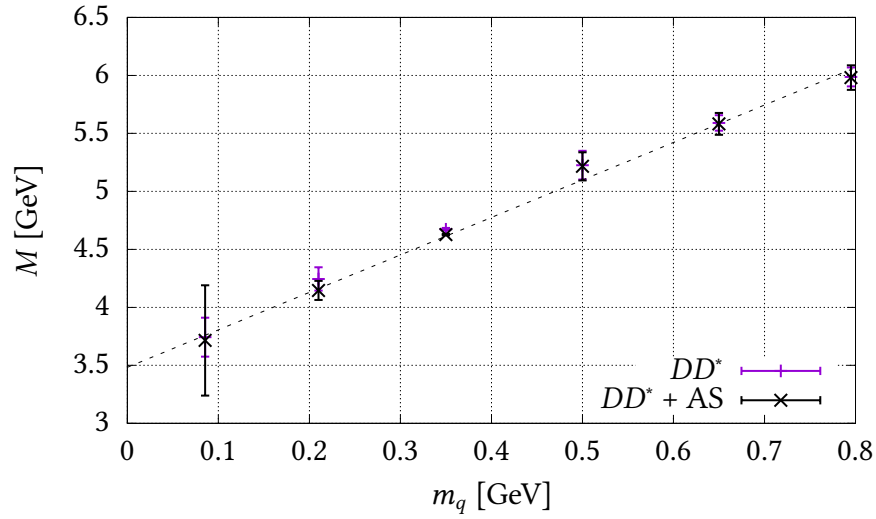


Figure 5.7: Mass curves for the $0(1^+)$ open charm tetraquark.

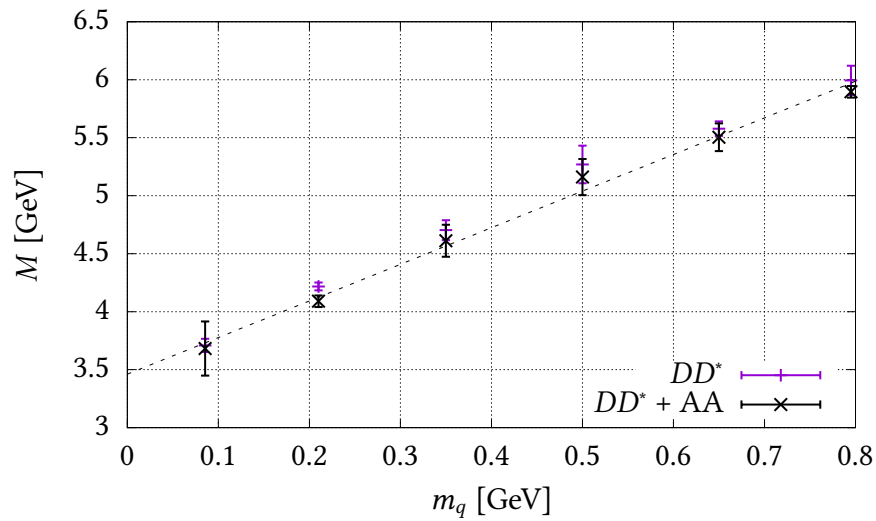


Figure 5.8: Mass curves for the $1(1^+)$ open charm tetraquark.

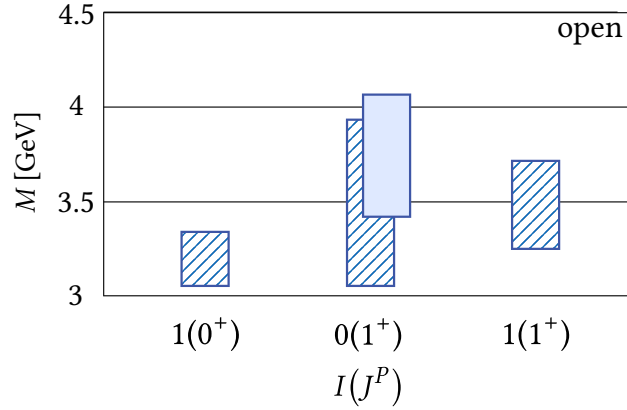


Figure 5.9: The open-charm mass spectrum. Blue shaped rectangles denote heavy-light states with $cc\bar{q}\bar{q}$ and $q = u/d$ including the error bars from extrapolations; blue shaded rectangles denote heavy-light states with strange content, $cc\bar{s}\bar{s}$.

are given by

$$M_{cc\bar{q}\bar{q}}^{0(1^+)} = 3.49(48) \text{ GeV} \quad (5.8)$$

$$M_{cc\bar{s}\bar{s}}^{0(1^+)} = 3.76(35) \text{ GeV}. \quad (5.9)$$

$I(J^P) = 1(1^+)$

The axialvector isovector state also shows a similar behaviour as its isoscalar partner, as it is clearly dominated by DD^* and not by D^*D^* , whereas diquarks are almost irrelevant again since we get similar results as in the $0(1^+)$ case. The mass for $q = u/d$ is given by

$$M_{cc\bar{q}\bar{q}}^{1(1^+)} = 3.47(24) \text{ GeV}. \quad (5.10)$$

Summary

Similar as in the hidden charm case, we also see a reasonable mass ordering for different angular momentum quantum numbers; $J = 1$ states are heavier than $J = 0$ states. Since there are no experimental candidates yet, we cannot do a corresponding comparison. Again, we can visualize the spectrum as seen in Fig. 5.9.

5.1.3 Comparison between Hidden- and Open-Charm Candidates

The transition between hidden- and open charm states is done by shifting the “anti-particle property” from a quark to another one of the other type. Although one can intuitively expect that this should not result in a huge mass difference, it seemingly does in our calculations. In general one could say that axialvector open charm states appear lighter than the corresponding hidden charm states within our equations. A possible explanation for that on the level of the BSE is the interaction – pure D -mesonic quark exchange diagrams couple stronger, which can also be seen by comparing the associated BSAs: the values of the amplitudes are numerically larger for D mesons than those included in hadro-charmonium and diquark configurations, which supports that

the largest BSE eigenvalue (which corresponds to the ground state) is dominated by D mesons. Keeping in mind that the error bars are large, definite statements about the mass remain vague, but so do not the statements about substructure dominances. That the calculated open-charm tetraquarks are bound and thus, comparably stable, aligns oneself into arguments from Ref. [136], where the authors demonstrated that $QQ\bar{q}\bar{q}$ states are stable in the heavy quark symmetric limit. We see that diquarks are irrelevant in almost every channel and mesonic contributions prevail over any other. Hadro-charmonium structures only become relevant, when pions are possible substructures, and this is the case only for isovector states. We assume that this is due to the low mass of the pion, which makes a bound state lower in mass than a state with heavier components. But even if hadro-charmonium is a significant component of the full state, the molecular component is dominating the full solution in every case (note that we often get no solution at all when we exclude it). This is mostly in good accordance with recent DSE/BSE results in an effective four-body picture [46, 91] and encumbers several diquark model calculations [21–23].

5.2 Quarkonium Mixing in the Light Quark Sector

In this section we present results for four- and two-quark states in the light quark sector ($q = u, d, s$) by mixing them together to make statements about the inner structure. In the first part of this section, we will investigate the $\sigma/f_0(500)$ by evaluating the eigenvalue curves for real Q^2 . In the second part we will repeat this calculation for complex Q^2 in order to make also statements about the decay width. Then, we transfer this procedure to setups with strange content and conclude the section with a description of the heavy-light four-quark candidates $f_0(980)$ and $a_0(980)$.

5.2.1 Real Momenta

The $\sigma/f_0(500)$ on the real axis

We approach the light $0(0^{++})$ meson, also called σ or $f_0(500)$, which has T -matrix poles at

$$\sqrt{-Q^2} = [i(400 \dots 550) \pm (200 \dots 350)] \text{ MeV} \quad (5.11)$$

in the second Riemann sheet, according to a collection of lots of analyses, including the most advanced model-independent ones from Roy-like dispersion relations [106, 137]. The pure Bethe-Salpeter Rainbow-Ladder results for a scalar $q\bar{q}$ meson with Maris-Tandy interaction, around $M \approx 650$ MeV, are known for years now and are clearly not located in the domain given in Eq. (5.11). However, this does not seem too astonishing, since a pure RL calculation does not include any decay terms which could find expression in a width. Therefore, a serious treatment of a scalar meson could only happen via BRL calculations. It shows however, that the currently most advanced BRL calculations of a pure scalar $q\bar{q}$ meson with an analysis on the real axis primarily lead to higher meson masses [56, 116] and do not make statements about the width at all as they don't include decay diagrams. From recent two-body calculations, a width of the scalar $q\bar{q}$ meson, generated from the $\sigma \rightarrow \pi\pi$ decay as an additional diagram to the RL kernel, could be determined with a

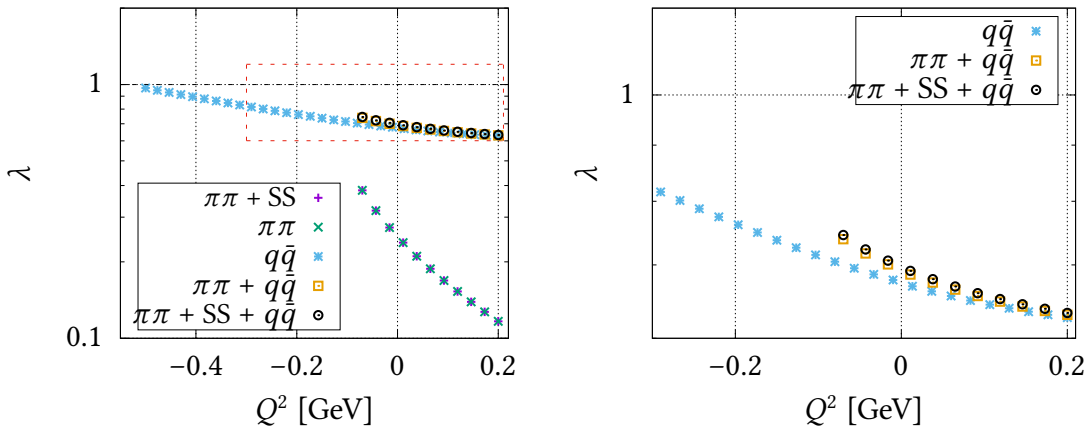


Figure 5.10: The eigenvalue curves $\lambda(Q^2)$ of the $\sigma/f_0(500)$ for different setups. The notations $\pi\pi$ (mesonic) and SS (scalar diquark-antidiquark) stand for two-body tetraquark components and $q\bar{q}$ is obviously denoting the quarkonium component. The r.h.s. shows the section located inside the red dotted rectangle on the l.h.s. and provides an insight to the details of the mixed curves.

pole located at $\sqrt{-Q^2} \approx (600 - i 90)$ MeV [138]. While the real part of the mass decreased by the kernel extension, the eigenvalue curve is still dominated by the RL part and one can expect that it will further increase by taking a more realistic interaction than the Maris-Tandy one. Since quark model calculations predict a scalar $q\bar{q}$ state in a higher mass region as well, a tetraquark character seems natural, and DSE/BSE studies in the past [47, 120] strengthened this expectation as we find a pure tetraquark state with a mass around 350 – 450 MeV in both, two- and four-body calculations. We have to keep in mind that these values result only from extrapolations of the eigenvalue curves on the real axis and do not consider the potential behaviour in the complex plane and the branch cut structure. It is now interesting to see how, and if, how significant a $q\bar{q}$ state couples to a $q\bar{q}q\bar{q}$ state. To gain knowledge about this, we perform calculations based on the technicalities described in chapter 4.5 and compare the resulting masses as well as the eigenvalue curves coming from solving the BSE on the real axis.

In this section, different setups will be compared:

- a pure tetraquark state with only the pionic substructure ($\pi\pi$),
- a pure tetraquark with pionic and diquarkonic ingredients ($\pi\pi + SS$),
- a quark-antiquark state (ordinary quarkonium) using RL truncation and the Maris-Tandy interaction model ($q\bar{q}$),
- a mixing state of a pionic tetraquark and the quark-antiquark state ($\pi\pi + q\bar{q}$) and
- a mixing state of a pionic/diquarkonic tetraquark and the quark-antiquark state ($\pi\pi + SS + q\bar{q}$).

Via Fig. 5.10, the analysis of the eigenvalue curve of a pure tetraquark state yields what we already got from calculations in the past [120]: diquarks do not play a role at all

setup	ground state mass [MeV]	1st excited state mass [MeV]
$\pi\pi$	416(26)	970(130)
$\pi\pi + \text{SS}$	416(26)	970(130)
$q\bar{q}$	667(2)	1036(8)
$\pi\pi + q\bar{q}$	472(22)	1080(280)
$\pi\pi + \text{SS} + q\bar{q}$	456(24)	1110(110)

Table 5.3: The masses of the ground state and the first excited state using different setups isolating and mixing tetraquark components and quarkonia from and with each other according to extrapolations on the real axis. The error estimates come from the extrapolations. We calculate the mass by using the on-shell mass relation $Q^2 = -M^2$.

here. The pure $q\bar{q}$ state, calculated via Rainbow-Ladder truncation using the Maris-Tandy model, follows an eigenvalue curve that crosses $\lambda = 1$ at $P^2 \approx -0.5 \text{ GeV}^2$, which compares well to RL results from the literature, e.g. from [116]. Looking further at the states with quarkonium mixing, we see that the eigenvalue curves almost match with the $q\bar{q}$ curve in the spacelike region and deviate from that when going into the timelike region, where they start to increase significantly stronger than the $q\bar{q}$ curve. On the right panel, we see that the curve with diquarkonic contributions is lying a bit higher than the one without when the mixing with the $q\bar{q}$ state is enabled, whereas in the pure tetraquark case, the curves with and without the diquarkonic SS component match quite precisely.

A quantitative investigation of the eigenvalue curves using the SPM yields the results shown in Tab. 5.3, where we also extrapolated the solutions of the second largest eigenvalue, which provides information about the first radial excitation.

Concluding remarks. From this analysis we conclude that tetraquark components are basically responsible for the low mass of the $\sigma/f_0(500)$. While the $q\bar{q}$ curve seems to dominate also the mixing curves in the spacelike region where the eigenvalues of the pure tetraquark states are quite low, the rise of the tetraquark curve starts to dominate the solution such that the mass decreases overall in comparison with the $q\bar{q}$ state. The responsibility of the tetraquark components regarding the low mass also makes sense by keeping in mind that tetraquarks are an explanation for the ‘inverse’ mass ordering we find in the light scalar meson spectrum as pointed out in the introduction. It is interesting to see that the diquark-antidiquark component becomes more relevant for the full solution when the mixing with ordinary quarkonia is enabled, whereas it seems to have almost no influence on the solution with only tetraquark components. We have no deep explanation for this effect, but we observe that the diquark-antidiquark component seems to couple stronger to the $q\bar{q}$ component than it does to the $\pi\pi$ one. At this point, we rely on extrapolations from the information we got for the eigenvalue curve on the real axis, but for an investigation of the state as a resonance, calculations in the complex plane have to be performed using a path deformation for the radial integral to avoid the internal poles, which prevent us from evaluating the eigenvalue curve apart from real axis. Such a path deformation is addressed in section 4.6.

5.2.2 Complex Momenta

Going above the threshold requires knowledge of the eigenvalue curve in the complex plane since a resonance state should appear in the second Riemann sheet as a T matrix pole or as a solution of the BSE, respectively. We perform those calculations for the lightest scalar meson, the $\sigma/f_0(500)$ by doing a path deformation of the radial integral as described in section 4.6. Other than in the last section, we restrict our calculations to the timelike region where the mass M and the width Γ are positive real numbers. We expect that the information about the pole in the second Riemann sheet is stored above the threshold anyway, as it is the case e.g. in [45].

We will distinguish between different setups again, with and without four- and two-quark contributions, and compare the calculated data points as well as the data we conclude from extrapolations into the second Riemann sheet. We will also compare the results for different parameters of the Maris-Tandy model while varying the coupling consistently as a whole parameter set.

The $\sigma/f_0(500)$

The eigenvalue curve in the (M, Γ) plane for a renormalized quark mass of 3.8 MeV is shown in Fig. 5.11 as a three dimensional plot. The real part of the eigenvalue curve is subtracted by one and the imaginary part got a negative sign. In that way, we can visually distinguish the two curves and conclude a solution of the equation, if both curves

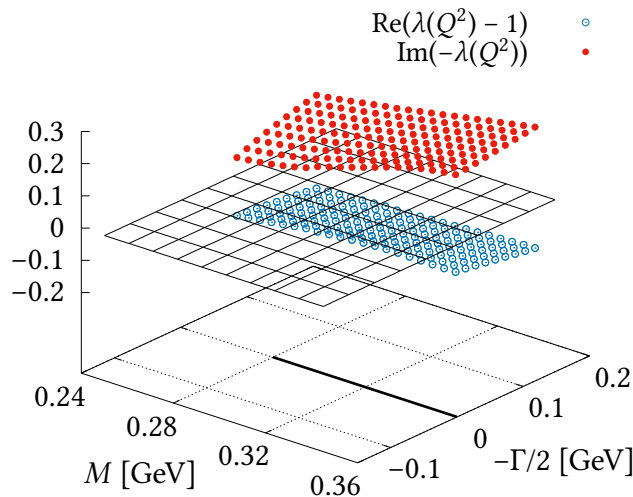


Figure 5.11: An exemplary example: the complex eigenvalue curve of the mixed $\sigma/f_0(500)$ including all components: four- and two-quark candidates. The values of the real part (red/filled circles) and the imaginary part (blue/open circles) are shown in a form where the equation shows a solution, iff both curves cross the ‘zero plane’ simultaneously; that zero is illustrated by the black lattice. Also, the two-pion branch cut is shown by the thick black line on the (M, Γ) domain.

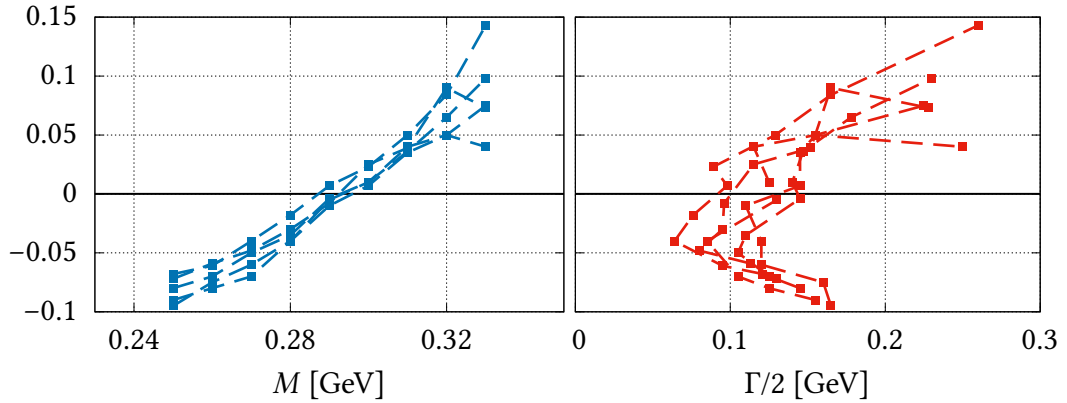


Figure 5.12: Projections of the sticky curves of the mixed $\pi\pi + SS + q\bar{q}$ state for different sets of model parameters in the sense of Tab. 3.2. Left panel: the sticky curves projected onto the (M, λ) plane. Right panel: the sticky curves projected onto the (Γ, λ) plane. The ordinate shows the real as well as the imaginary part of the eigenvalue λ , which have the same value, cf. 4.6.

cut the zero (black lattice) simultaneously. Also, the two-pion cut is shown by the thick, black bar in the (M, Γ) domain. As it is not possible otherwise, the plotted points are given in a specific domain in the first Riemann sheet, which is restricted by the following constraints:

$$0.24 \text{ GeV} \leq M \leq 0.36 \text{ GeV} \quad \text{and} \quad 0.05 \text{ GeV} \leq -\Gamma/2 \leq 0.20 \text{ GeV} \quad (5.12)$$

By looking at the imaginary part of the curve, we instantly see the threshold effects: the opening of the characteristic branch cut.¹ Also, the imaginary part as well as the “reduced” real part of the eigenvalue curve approach the zero plane by going towards the real axis. Besides this curve, which includes all components (mesonic, diquarkonic and two-quark), we calculated the curves with component exclusions as well, although we will not show those curves in this work because of the similar appearance. Instead, we show the results for the extrapolated solutions following from computing the sticky curves, which are shown in Fig. 5.12. For readability reasons, we do not show the three-dimensional plot, but the projections onto the mass and width coordinates. We see the sticky curves for the full $\sigma/f_0(500)$ candidate as a mixed state for different model parameter sets as shown in Tab. 3.2. The mass of the state barely depends on the model parameter variation; merely the width changes significantly for different setups. Altogether, this delivers a model error for our results. We note that the extrapolation error, which is in this case part of the sticky curves for the Γ projection, is at the order of 10% and overshadowed by the model error – therefore, it is neglected in the following.

The sticky curves for the mixed state as given in Fig. 5.12 deliver a stable mass in the range of 290 ... 300 MeV and a half width in the range of 90 ... 150 MeV. We show the results for the masses and widths as well as the model errors in Tab. 5.4. We denote

¹The eigenvalue curve has to be symmetric under complex conjugation when staying in a Riemann sheet and the imaginary part is clearly non-vanishing near the real axis.

setup	M [MeV]	$\Gamma/2$ [MeV]
$\pi\pi + \text{SS} + q\bar{q}$	291(5)	121(22)
$\pi\pi + \text{SS}$	302(7)	148(31)
$\pi\pi$	301(7)	158(29)
$q\bar{q}$	661(8)	0

Table 5.4: The results for the $\sigma/f_0(500)$ candidate. The left column denotes the different components which are included in the respective calculation and the other columns show the mass and half width as well as the model error we extracted from the sticky curves.

the mass as the imaginary part of the Mandelstam variable \sqrt{s} and $\Gamma/2$ as the associated negative, real part. It is clearly visible that the $q\bar{q}$ and the SS component only provide small corrections on a few-percent level to the mass of the $\pi\pi$ state, but larger ones (on a 20% level) to the width. Furthermore, the pure $q\bar{q}$ state mass is still far off. We conclude that the state is basically a $\pi\pi$ state and thereby comply with our findings from calculations on the real axis. A comparison with these findings from a quantitative point of view entails that the mass resulting from an analysis in the complex plane is significantly lower and thereby also lower than the PDG mass [106]. We suppose that these discrepancies could be traced back to our truncations and the interaction model, which binds the tetraquark state stronger than it is bound in reality. To investigate this, it is possible to vary the coupling between different components inside the BSE consistently – we found that the pole location is especially sensitive to the coupling of meson-meson and meson-quarkonium diagrams. Lowering those couplings by 30% of their strengths in these channels results in a solution $(M, \Gamma/2) = (309(14), 232(54))$ MeV, which is somewhat closer to the PDG value and supports our supposition of a model issue. Concerning the comparison with the former extrapolation on the real axis, it is important to note that the statements about the inner structure remain stable, although the mass fell significantly into a region which is clearly away from the PDG region. That leaves us with the belief that the statements about the dominant substructures of heavy-light 4-quark states from section 5.1 remain valid as well, though it is clear that it would need a deeper investigation to do reliable statements.

With our qualitative results of a lucid non- $q\bar{q}$ interpretation of the σ , we are in accordance with results of a variety of approaches, such as lattice QCD [27, 139–141], dispersion theory [142], effective field theories [58, 59, 143], DSEs [47, 120] and model studies [56, 61, 144], which also indicate a four-quark nature as already stressed in section 1.3.

Stranged, equal-mass mixed states

Besides a description of four-quark states with light quark content, it is also possible to consistently raise the quark masses simultaneously to investigate the behaviour of different setups. Especially, a central question would be, if the four-quark dominance persists while doing that, or not. The calculations have been done in the same manner as in the previous paragraph – the eigenvalue curves were calculated inside a square in the first Riemann sheet above the threshold mass and analytically continued into the

second one by computing the sticky curves. We show the results quantitatively as masses and widths in Tab. 5.5 and qualitatively as ovals in the complex plane in Fig. 5.13, whose widths and heights correspond to the model error. From a light quark mass of 3.8 MeV, we increase the mass in three steps to arrive at the strange quark mass, given by 85.5 MeV¹.

We see that the mixed state for the light quark mass, which corresponds to the σ , is clearly dominated by the 4-quark component since the states lie on top of each other, but this is nothing but the result we know already from previous calculations. By increasing the quark mass, it is interesting that the four-quark dominance seems to get lost during this process. While there is a pretty mixed picture visible for quark masses of 20 and 50 MeV, the state shows up to be dominated by the two-quark component for strange quarks, since the corresponding states overlap and the 4-quark state appears to be far off. This is how we would expect the results from a physical point of view, since the dominance of 4-quark components in the σ is a chiral effect in the first place. For heavier quarks such as the strange one, these chiral effects lose relevance more and more.² For us, this acts as a proof of principle for our approach and shows its potential, even though there are no experimental candidates for an all-strange 4-quark state, yet. It motivates the next part, namely the description of heavy-light mixed states with strange quark contributions, for which experimental candidates definitely exist: the $f_0(980)$ and the $a_0(980)$.

Stranged, heavy-light mixed states: the $f_0(980)$ and $a_0(980)$

As scalar states close to the $K\bar{K}$ threshold, the $f_0(980)$ and the $a_0(980)$ with masses and widths of

$$(M, \Gamma/2)_{f_0(980)} = (970 \dots 1010, 5 \dots 50) \text{ MeV} \quad (5.13)$$

$$(M, \Gamma/2)_{a_0(980)} = (960 \dots 1000, 25 \dots 50) \text{ MeV} \quad (5.14)$$

according to the PDG [106] are predestinated four-quark state candidates, and an analysis as mixed states is a reasonable step towards a description of these particles. Essentially, both states are identical apart from isospin: the $f_0(980)$ is an isoscalar and the $a_0(980)$ is an isovector. Correspondingly, mixing with a quarkonium state is possible for the $a_0(980)$ only if the quarkonium consists of two light quarks, but a mixing to a “strangeonium” is forbidden due to isospin conservation. The $f_0(980)$ however could have an $s\bar{s}$ component, which makes this object particularly interesting for the studies in this work.

For a description of the two setups, we generally consider the following substructures motivated by decay channels and general possibilities that allow the respective quantum numbers:

$$\circ f_0(980) = \underline{K\bar{K}} + \pi\pi + \underline{SS} + (u\bar{u} + d\bar{d}) + s\bar{s}$$

$$\triangle a_0(980) = \underline{K\bar{K}} + \pi\eta + \underline{SS} + (u\bar{u} - d\bar{d})$$

¹This mass is fixed in a way that our model yields a good kaon mass at around 500 MeV for standard MT model parameters, cf. Tab. 3.3.

²This is basically because two constituent quarks become lighter than two (pseudoscalar) mesons.

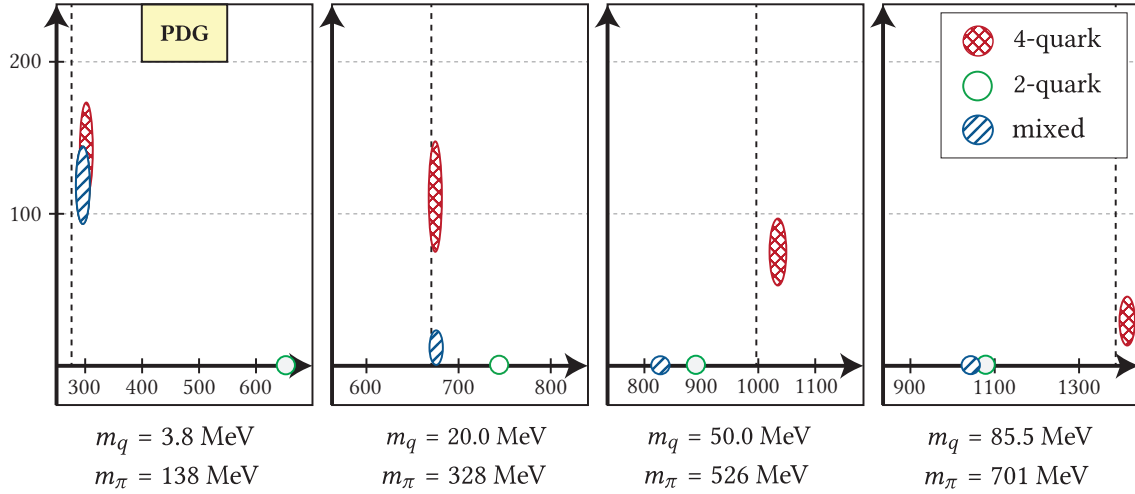


Figure 5.13: Plot of the extrapolated solutions of the equal-mass states for different quark masses. The abscissas indicate the mass M in MeV and the ordinates indicate the half width $\Gamma/2$ in MeV as well. The ovals denote the solutions with the corresponding error bars coming from model variations. Note that for readability reasons, ovals are drawn thicker, if the error is too small. The numerical values can be drawn from Tab. 5.5. For the light quark case, $m_q = 3.8$ MeV, the PDG region for the $\sigma/f_0(500)$ is also drawn as a yellow rectangle. Clear, green ovals represent pure 2-quark states, dotted, blue ovals are 4-quark states, and shaped, red ovals represent the mixed state with 4- and 2-quark components combined.

m_q [MeV]	3.8	20.0	50.0	85.5
mixed	$291(5) - i \cdot 121(22)$	$669(3) - i \cdot 11(13)$	$827(3)$	$1047(12)$
4-quark	$302(7) - i \cdot 148(31)$	$665(10) - i \cdot 110(41)$	$1045(9) - i \cdot 74(22)$	$1414(21) - i \cdot 34(20)$
2-quark	$661(8)$	$739(6)$	$881(13)$	$1073(10)$

Table 5.5: The numerical values for the plot above. All values are given in MeV and errors come from model variations. The first row states the renormalized quark masses and the values below are the pole positions of the BSE solutions for the respective setups in the form $M - i \cdot \Gamma/2$.

In our calculations, we will only consider the underlined clusters for technical reasons: The $\pi\pi$ component will not be considered because it would require internal conversion of quark flavours – on the one hand, this is tremendously difficult to implement into our equation consistently as it would have to be derived from the outset and on the other hand, it should not significantly affect the mass of the state as the corresponding diagram should be OZI suppressed¹. Furthermore, although a $\pi\eta$ state would be a possible candidate e.g. for the $a_0(980)$ [86], the light pion pole heavily restricts the domain where an evaluation of the BSE eigenvalue curve is possible. That entails that extrapolations would lose their accuracy to an extent where a prediction is not reasonable any more. Because of that, we will cut out pionic contributions completely. Furthermore, we will exclude the $(u\bar{u} \pm d\bar{d})$ components in our pure RL calculations, because they represent the pure $q\bar{q}$ as a σ candidate and its isospin partner, which yet are way too light in our model and thus, is not a realistic choice for a quarkonium mixing in this energetic region: It would spuriously dominate the state due to its low mass. However, more realistic BRL calculations show that the mass of the scalar two-quark state is at around 1.1 GeV, and recent lattice results indicate that the $a_0(980)$ is indeed a superposition of a tetraquark and such an ordinary $q\bar{q}$ state [36]. A corresponding DSE/BSE calculation would require model improvements first to provide a convincing comparison. We will include those light quark states into the equation later in this chapter by modelling the BRL effects in a very simple way.

With the emphasized choice we treat the $f_0(980)$ as an $a_0(980)$ with an additional $s\bar{s}$ component in a pure RL calculation². The setups we investigated are the following:

- a fully mixed state ($K\bar{K} + SS + s\bar{s}$)
- △ a pure four-quark state ($K\bar{K} + SS$)
- a *strangeonium* state with kaonic contributions ($s\bar{s} + K\bar{K}$)
- a *strangeonium* state with diquarkonic contributions ($s\bar{s} + SS$)
- a pure RL *strangeonium* state ($s\bar{s}$)

Points with a circle (○) correspond to potential $f_0(980)$ candidates and the triangle (△) corresponds to an $a_0(980)$ candidate. Note that the latter is a truncated, four-quark exclusive version of the full $f_0(980)$ candidate as well since we are working in the isospin symmetric limit.

The numerical results are shown in Tab. 5.6; errors stem from model variations. Note that bound states below the mass threshold could not have a width different than zero due to the absence of a decay channel in our diagrams. Because of this, we interpret all non-zero widths for states below the corresponding thresholds (every state except the pure four-quark state) as numerical artefacts. In Tab. 5.6, these widths are starred.

¹Internal gluon lines for a flavour conversion yields to disconnected diagrams once the gluon lines are cut. According to the OZI rule, these diagrams are suppressed. [145–147]

²and a different isospin, but this only attracts attention when looking at the amplitudes – the flavour traces remain the same

f_0	a_0	setup	mass [MeV]	half width [MeV]
✓		$s\bar{s} + SS + K\bar{K}$	915(20)	2(3)*
✓	✓	$K\bar{K} + SS$	1001(4)	24(16)
✓		$s\bar{s} + K\bar{K}$	927(18)	1(3)*
✓		$s\bar{s} + SS$	1057(14)	0(1)*
✓		$s\bar{s}$	1073(10)	0

Table 5.6: The comparison of the masses and the (half) widths between different setups for the mixed $f_0(980)$ and the $a_0(980)$ candidate with quark content $s\bar{s}(q\bar{q})$. The S's denote scalar diquarks as possible building blocks of the tetraquark. Checkmarks denote whether a state is a potential $a_0(980)$ or $f_0(980)$ candidate. The starred widths are the ones which have to be treated as zeroes as explained in the text.

Two-quark state. We see the pure Rainbow-Ladder $s\bar{s}$ bound state at 1073(10) MeV. Compared to a more realistic beyond-RL description of scalar quarkonia in that region [102], this mass appears too small, similar to the two-quark RL description of the σ candidate.

Four-quark contributions. Adding diquarks to the pure two-quark state decreases the mass slightly – but still, they only provide corrections on a few-percent level (1073 \rightarrow 1057 MeV). It is quite a different picture when adding the $K\bar{K}$ component instead. Here, the mass of the state goes down significantly. We get an average solution clearly below the $K\bar{K}$ threshold at 927(18) MeV and therefore, it tends to appear as a bound state in our equations. When adding the diquark-antidiquark component to the $s\bar{s} + K\bar{K}$, we see that the effect is again negligible within error bars (927 vs. 915 MeV). We find a fully mixed state at 915(20) MeV including all three components. We can further compare this with a pure four-quark state by excluding the $s\bar{s}$ component. We arrive at a state slightly above the $K\bar{K}$ threshold with a mass of 1001(4) MeV and a half width of 24(16) MeV; the corresponding sticky curve is shown in Fig. 5.14.

The $f_0(980)$. We conclude that the $K\bar{K}$ component is vital for a description of the ground state of the $f_0(980)$ candidate. It lowers the ground state mass of the pure $s\bar{s}$ state significantly into a region between 900 and 1000 MeV, where potential candidates are expected and establishes a state with a reasonable mass (927 MeV) even without adding a diquarkonium component at all. In general, the mass never falls below 1 GeV unless we include the kaonic structure. With the diquarkonium component added, we get a mass of 915 MeV, indicating that it only plays a minor role for a description of the ground state. This is as expected due to the fact that heavy-light diquarks are much heavier than kaons. The inclusion of the $s\bar{s}$ state lowers the mass of the pure four-quark significantly (1001 \rightarrow 915), which underlines the importance in this setup with a RL interaction – in a BRL calculation, this importance might change. Similar to the light quark sector, we find a state which is considerably lighter than the experimental candidate – although, the deviation from the PDG value is much smaller ($< 10\%$).

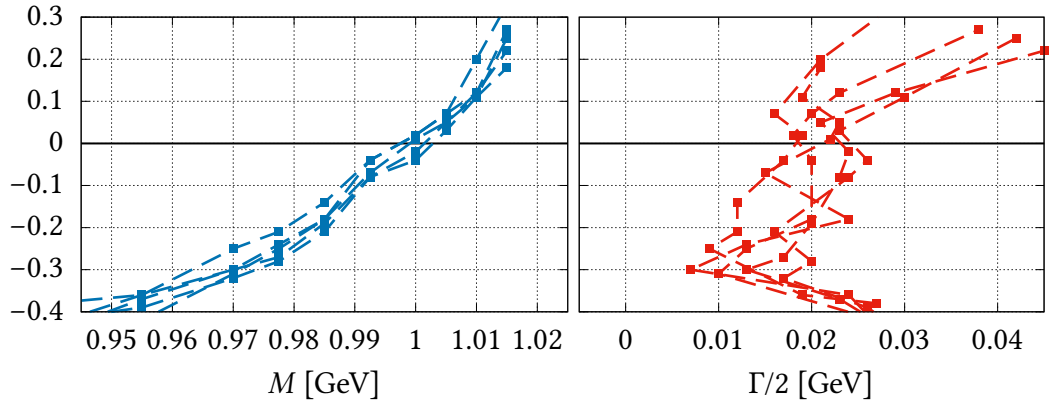


Figure 5.14: The sticky curves for the $a_0(980)$ candidate as a state $K\bar{K} + SS$. The left panel shows the (M, λ) plane and the right panel shows the (Γ, λ) plane. Different sticky curves correspond to different sets of model parameters (see Tab. 3.3), each yielding a good kaon mass.

The $a_0(980)$. Our mass for the only $a_0(980)$ candidate, the pure four-quark state consisting of $K\bar{K} + SS$, lies at 1001(4) MeV with a half width of 24(16) MeV and is therefore qualitatively in good agreement with the experimental interval of 980(20) MeV where the state was seen. The error bars are in fact overlapping. It is the only state in our calculation that appears as a resonance above the $K\bar{K}$ threshold.

Summary and Conclusions. We find candidates for the states $f_0(980)$ and $a_0(980)$. The strangeonium component, which is the only difference between both states on the BSE level¹, shows to be significant as it reduces the mass of the four-quark state by circa 90 MeV. We see a different behaviour here compared to the $\sigma/f_0(500)$ candidate, where the quarkonium component was much heavier than the pure four-quark state. For a reasonable integration into the spectra of light mesons, it would be mandatory to include also the light $q\bar{q}$ component with $q \in \{u, d\}$ instead of the $s\bar{s}$, since the $q\bar{q}$ mass is located in a similar mass region as the four-quark mass in an advanced BSE calculation [102]. Quite recently, lattice calculations indicated that there is a non-negligible mixing of the four-quark candidate of the $a_0(980)$ and a quark-antiquark state [36]. Due to model issues², calculations like these are not convincing at this point in our formulation. Further lattice studies also propose a coupling to the $\pi\eta$ component [86]. For a complete investigation of the $f_0(980)$ and the $a_0(980)$, an inclusion of these channels along with an inclusion of the second mesonic component ($\pi\pi/\pi\eta$) are the remaining pieces in the puzzle of understanding the inner structures of these states.

¹The occurring flavour traces in the tetraquark kernel diagrams are identical for both isospin configurations. The second mesonic configuration would show a isospin difference as well ($\pi\pi$ vs. $\pi\eta$), but we explicitly excluded this component for technical reasons, as explained above.

²As stated before, the scalar RL $q\bar{q}$ state with $q = u/d$ is way too light.

f_0	a_0	setup	$M - i \cdot \Gamma/2$ [MeV]	
			RL	BRL model
✓		$s\bar{s}$	1073(10)	1479(39)
✓	✓	$s\bar{s}q\bar{q}$	1001(4) - i · 24(16)	1001(4) - i · 24(16)
✓		fully mixed	915(20)	994(7)

Table 5.7: Results for different setups (pure $s\bar{s}$ two-quark, pure $s\bar{s}q\bar{q}$ four-quark and fully mixed $s\bar{s}q\bar{q} + s\bar{s}$) in a pure RL calculation in contrast to a calculation where BRL effects for the $s\bar{s}$ state are modeled in a simple way as described in the text. Checkmarks (✓) indicate whether a state is a potential f_0 or a_0 candidate similar to Tab. 5.6.

“BRL model”

For energetic reasons, it is reasonable to believe that an $s\bar{s}$ state becomes less important, if a BRL coupling would be implemented into the equation, although we are currently unable to perform calculations like this due to technical limitations. Furthermore, it would make us capable of including a meaningful light $q\bar{q}$ component into the equations for the a_0 and the f_0 . For that reason, we exploratively lower our RL coupling by attaching a factor $c < 1$ to the occurring RL diagrams of type (3) and (4) (cf. Fig. 4.3), which should model BRL effects in a very simple way. We did two calculations:

- one for a mixed $s\bar{s} + s\bar{s}q\bar{q}$ candidate with a factor $c = 0.5$ and
- one for a mixed $q\bar{q} + q\bar{q}s\bar{s}$ candidate with a factor $c = 0.2$.

As a result, the masses of the scalar $s\bar{s}$ and $q\bar{q}$ states get pushed into a reasonable region: the $s\bar{s}$ gets a mass of 1.4 – 1.5 GeV and the $q\bar{q}$ is lying at around 1.3 GeV. Although these are not precise values motivated by a true BRL calculation, they seem reasonable to us, since the two-quark σ candidate has a BRL mass of 1.1(1) GeV in [102] and we expect realistic scalar $q\bar{q}$ states to have an even higher mass. We substantiate that by looking at the potential quarkonium candidates that were seen by experiment: candidates for the pure $q\bar{q}$ state would be the $f_0(1370)$ or the $a_0(1450)$, which finds further support by linear sigma model studies [61]; correspondingly, the scalar $s\bar{s}$ would have an even higher mass. Findings in an effective description of QCD strengthen our assumptions [56].

Modified $s\bar{s}$. The results for the $s\bar{s}(q\bar{q})$ candidate are shown in Tab. 5.7. In course of the modification, the $s\bar{s}$ state increases by roughly 400 MeV (1073 → 1479 MeV). Thereby, the mixed state mass shifts close to the four-quark mass (915 → 994 MeV), such that the two setups have an overlap in terms of error bars (994(7) vs. 1001(4) MeV).

Modified $q\bar{q}$. We show the results in Tab. 5.8. By looking at the RL result we see that the pure $q\bar{q}$ state and the mixed state are in a similar region (661 vs. 644 MeV), whereas the pure $q\bar{q}s\bar{s}$ state is far off with the mass we already know from previous calculations (1001 MeV). This indicates that the two-quark state clearly dominates the mixed one, which we expected beforehand. When we apply the BRL model, the pure $q\bar{q}$ mass almost doubles to a value of 1288 MeV, whereas the pure $q\bar{q}s\bar{s}$ state remains the same since the associated diagrams are not modified as in the $s\bar{s}$ modification. Contrary, the mass of the

f_0	a_0	setup	$M - i \cdot \Gamma/2$ [MeV]	
			RL	BRL model
✓	✓	$q\bar{q}$	661(8)	1288(38)
✓	✓	$q\bar{q}s\bar{s}$	1001(4) - i · 24(16)	1001(4) - i · 24(16)
✓	✓	fully mixed	644(6)	999(4) - i · 17(8)

Table 5.8: Results for different setups (pure $q\bar{q}$ two-quark, pure $q\bar{q}s\bar{s}$ four-quark and fully mixed $q\bar{q}s\bar{s} + q\bar{q}$) in a pure RL calculation in contrast to a calculation where BRL effects for the $q\bar{q}$ state are modeled in a simple way as described in the text. Checkmarks (✓) indicate whether a state is a potential f_0 or a_0 candidate similar to Tab. 5.6.

fully mixed state strongly shifts towards the pure four-quark mass ($644 \rightarrow 999$ MeV); the two states are now in fact overlapping within error bars ($999(4)$ vs. $1001(4)$ MeV).

For being able to compare with the lattice studies from [36] which used a pion mass of around 300 MeV, we set our light quark mass to 20 MeV which yields a pion mass of $m_\pi = 328$ MeV. Our statements by using the BRL model remained the same: the mixed state is still dominated by the $K\bar{K}$. The mass and width increase in this process so that we arrive at the following values for the fully mixed state consisting of $K\bar{K} + SS + q\bar{q}$:

$$(M - i \Gamma/2)_{m_\pi=328 \text{ MeV}} = 1090(3) - i 55(21) \text{ MeV} \quad (5.15)$$

Conclusions and Interpretations. For both modifications we observe the effects that we expected beforehand: the mixed states become heavier and shift closer to the corresponding pure four-quark states. We conclude that the quarkonium components therefore do not play an important role in the description of fully mixed states as the inclusion and exclusion of the $q\bar{q}/s\bar{s}$ components does not change the masses significantly – we observe only small effects of the order of 1%. Interestingly, the modification of the pure $q\bar{q}$ state brings the mixed state closer towards the four-quark state than the modification of the $s\bar{s}$ component although the latter one is considerably heavier. We trace that back to our model and the small factor of $c = 0.2$ (vs. $c = 0.5$ for the $s\bar{s}$ modification) which might result in a stronger suppression of the mixing diagrams.

However, our findings here yield the suspicion that the calculated masses for the mixed RL-states given in Tab. 5.6 should receive a correction which favours a four-quark interpretation of the $f_0(980)$ and the $a_0(980)$ over a two-quark or mixed one when real BRL effects are considered.

5.3 All-Charm Four-Quark Resonances

In order to investigate the nature of four-quark resonances consisting of $c\bar{c}c\bar{c}$, we first have to recall the properties of the only observed one, the X(6900). It is a narrow state which was discovered above the di- J/ψ threshold with a Breit-Wigner mass and width of [13]

$$\begin{aligned} M(X(6900)) &= 6905 \pm 11 \pm 7 \text{ MeV} \\ \Gamma(X(6900)) &= 80 \pm 19 \pm 33 \text{ MeV.} \end{aligned} \quad (5.16)$$

Its quantum numbers are yet unknown which motivates an investigation of putative states in various channels. We do this for four different possible configurations,

1. 0^+ with internal $\eta_c\eta_c + AA$
2. 0^+ with internal $J/\psi J/\psi + AA$
3. 1^+ with internal $\eta_c J/\psi + AA$
4. 1^+ with internal $J/\psi J/\psi + AA$

where A stands for an axialvector cc (anti-)diquark. Quantum numbers different from AA are forbidden because we use diquarks from the colour (anti-)triplet, see appendix C. Due to the observation of the X(6900) in the invariant mass spectrum of J/ψ pairs, the candidates 2 and 4 which have the corresponding content are particularly interesting ones. To get a proper description of the J/ψ meson, we use a current charm quark mass of $m_c = 845$ MeV as input. The corresponding RL masses for η_c , J/ψ and the axialvector cc_A diquark are given in Tab. 5.9.

We solve the pure two-body four-quark BSE and omit mixing with ordinary quarkonia since physical quark masses are not indicating that a state with that energy is a $c\bar{c}$ or $b\bar{b}$ state. For being able to extract a whole spectrum, we exploit the fortunate circumstance that we have equal mass content. That implies comparably small extrapolations and the possibility of an extraction of the masses of excited states, similar to the investigation of the $f_0(500)$ on the real axis in section 5.2. First, we will stick to determinations of masses on the real axis in order to extract a spectrum. We postpone the investigation of certain states in the complex plane to a later calculation.

The results for the mass spectrum for different configurations is shown in Fig. 5.15. Shaped rectangles denote states which are predominately meson-meson states and filled rectangles are states with significant diquark-antidiquark components. The height of the rectangles indicates the error which results from extrapolations via SPM and model variations. We did not apply a dynamic interaction model as detailed as in Tab. 3.2 here, but only vary the model parameter η within the range [1.6, 2.0] instead.

$J^P = 0^+$

The values for the masses of the scalar candidates are given in the upper row of Tab. 5.10. We see a light and strongly bound ground state which essentially consists of two (pseudoscalar) η_c mesons and has a mass of 5.34(2) GeV. Keeping this configuration, we see one

state	η_c	J/ψ	cc_A
mass [GeV]	2.92	3.10	3.54

Table 5.9: The RL masses of the two-quark states that we used as ingredients in order to describe all-charm tetraquark candidates. All numerical values are given in GeV.

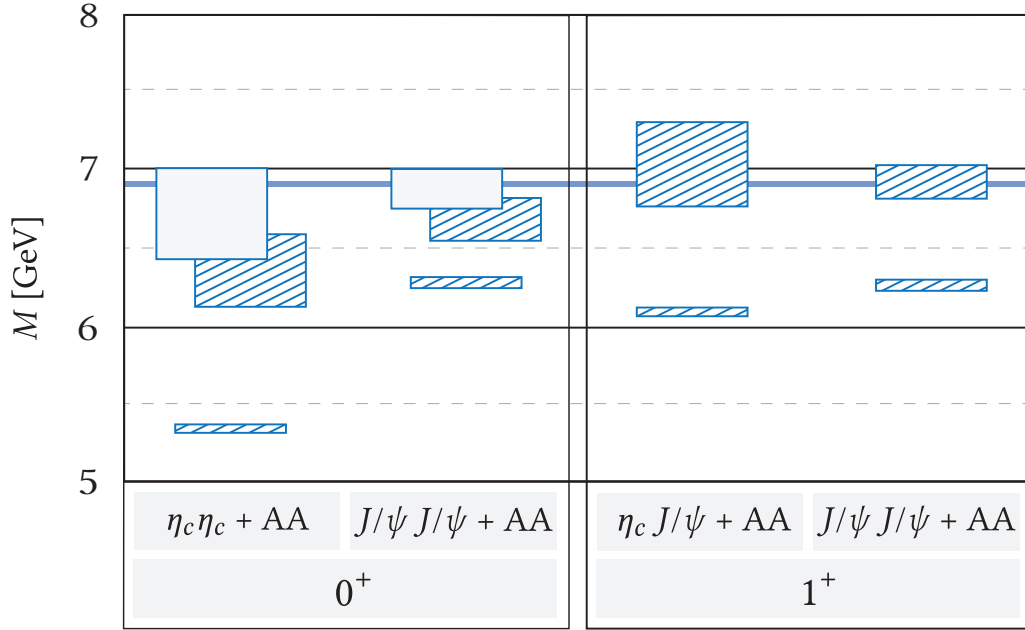


Figure 5.15: The calculated all-charm spectrum for different quantum numbers and setups. Shaded rectangles denote meson-meson dominated states, whereas filled ones stand for states with explicit diquark-antidiquark corrections. Dashed lines denote steps of 0.5 GeV on the mass axis and the continuous blue line slightly below 7 GeV denotes the mass of the X(6900) (with errors), taken from [13] and stated numerically in (5.16).

J^P	meson/diquark content	ground state	1st excited	2nd excited
0^+	$\eta_c \eta_c + AA$	5.34(2)	6.30(13)	6.70(30)
	$J/\psi J/\psi + AA$	6.30(3)	6.71(14)	6.87(12)
1^+	$\eta_c J/\psi + AA$	6.07(2)	7.03(26)	–
	$J/\psi J/\psi + AA$	6.28(4)	6.92(12)	–

Table 5.10: The results for the ground states and excited states for scalar (0^+) and axialvector (1^+) all-charm tetraquarks for different meson/diquark content.

excited mesonic resonance at 6.30(13) GeV and another second excitation at 6.70(30) GeV with small diquark-antidiquark corrections.¹ If we enforce the meson-meson part to be $J/\psi J/\psi$, a slightly different picture emerges. A resonant mesonic ground state is obtained just little *above* the two- J/ψ threshold at 6.30(3) GeV and we obtain two excited states at 6.71(14) and 6.87(12) GeV. As in the case with di- η_c meson input, the first excited state is a pure mesonic one and the second excitation includes small diquark corrections.

$J^P = 1^+$

For the axial-vector channel we show the numerical results in the lower row of Tab. 5.10. We see a ground state consisting of $\eta_c J/\psi$ at 6.30(3) GeV and an excited state at 6.71(14) GeV, both dominated by the mesonic content of $\eta_c J/\psi$. Specifying the meson content to $J/\psi J/\psi$, the same picture emerges. A light ground state resonance occurs at 6.28(4) GeV and we find the first excitation at 6.87(12) GeV; both states are dominated by the mesonic content. Diquark-antidiquark contributions seem completely irrelevant for the lowest-lying states, although it is worth to note that the eigenvalue spectrum indicates that higher excited states *do* have diquark contributions, similar to the 0^+ case. For technical reasons² it was not possible to extract masses for these higher states which include diquark corrections, which is why we only show the first excitations.

Summary

We see that the ground states we observe are not suitable candidates for the X(6900). In both the scalar and the axialvector channel, they appear too light as they all have a mass much lower than 6.5 GeV and the scalar $\eta_c \eta_c$ ground state is even strongly bound. The excited states however are lying in a proper ballpark, which could be seen in comparison with the dark blue bar which spans the whole diagram (Fig. 5.15) and denotes the Breit-Wigner mass for the X(6900) extracted by the LHCb collaboration including systematic and statistical errors [13].

In the 0^+ case, the states that fit the experimental candidate the most are the second excitations of the (di- $\eta_c + AA$) and (di- $J/\psi + AA$) configurations with diquark-antidiquark components and masses of 6.70(30) and 6.87(12) GeV. Note that the two setups differ regarding the mesonic content, but share the same diquark input. This indicates that diquark-antidiquark states gain relevance especially near their corresponding threshold.

The 1^+ case also shows too light ground states, but in contrast to that, the first excitations are in the correct ballpark. Here, both configurations, the first excitations of $\eta_c J/\psi$ and $J/\psi J/\psi$, share their error bars with the experimental one. Thus, one could speculate that both excitations together could correspond to just one state which is an overlap of $\eta_c J/\psi$ and $J/\psi J/\psi$, although this assumption would have to withstand a theoretical analysis that mixes those states together in a BSE. We did not do this yet because it would require a massive effort to adjust the program code that is used to solve

¹We could not do a statement about how much percent the diquark-antidiquark component contributes to the state; we conclude the non-negligibility from discrepancies between the meson-only and the fully-mixed calculations on the level of eigenvalues curves.

²far extrapolations and thus, unreasonably large error bars.

the two-body tetraquark BSE.¹

Our findings could be compared with numerous model calculations from the last years around this topic which assume a diquark-antidiquark structure [148–152]. These model calculations are mostly in agreement with each other that the most promising X(6900) candidates are not the ground states, but the first radial excitations of the s-wave solutions (2S states). In our equations, we also see an excitation in the 0^+ channels with small diquark corrections, but a corresponding lower-lying diquark-dominated ground state is missing. Therefore, we could not confirm the existence of those states in our model, but in turn see possible candidates for the X(6900) in the scalar and the axialvector channel, which are rather mesonic. Our findings partly agree with very recent calculations in a non-relativistic quark model that uses a spin-independent Cornell potential based on lattice calculations to investigate meson-meson resonances [153]; the agreements are especially present in the 1^+ channel, where the J/ψ J/ψ ground and excited state are in a very similar mass region, which supports the interpretation of an axialvector di- J/ψ resonance.

Complex energies. For the states with equal-meson content, namely for di- η_c and di- J/ψ , we could also investigate the eigenvalue curves in the complex plane. Using the path deformation specified in (4.49), we could go a little above the two-meson threshold to continue the eigenvalue curve into the complex plane to explore the respective ground states as done in section 5.2. The di- η_c ground state is bound and thus, there is no need to make further investigations here, but the di- J/ψ states in the scalar and axialvector channels are located slightly above threshold and thus, are suitable candidates. The calculations in the complex plane entail that for both states we find the following solutions:

$$(M - i\Gamma/2)_{0^+} = 6.26(2) + i \cdot 0.014(16) \text{ GeV} \quad (5.17)$$

$$(M - i\Gamma/2)_{1^+} = 6.24(2) + i \cdot 0.011(9) \text{ GeV} \quad (5.18)$$

Note the plus sign of the imaginary part which denotes that we find the average solutions in the *first* Riemann sheet. Whereas the error bar of the scalar state has a small overlap with the second Riemann sheet, the one from the axialvector state doesn't. This indicates that the states we observe are not necessarily physical. However, we want to stress that the eigenvalue curves are very sensitive to details. The fact that our equations are heavily truncated – for example, we only take into account one single meson/diquark Dirac tensor structure – makes a definite statement about whether the state is physical or not very vague. It is definitely conceivable that a slight modification of the model or the inclusion of one more tensor structure shifts the pole position back into the second sheet. For that reason, we will keep this result in mind but not attribute too much explanatory power to it.

¹It would particularly require that the M1 and M2 components contain *both*, the $\eta_c J/\psi$ and the $J/\psi J/\psi$ component. Right now, the code is constructed in a way that the M1 and M2 component merely describe only *one* configuration each.

CHAPTER 6

CONCLUSION AND OUTLOOK

Summary. In this work we explored the properties of potential four-quark states by using the framework of Dyson-Schwinger and Bethe-Salpeter equations (DSEs and BSEs). We did so by applying Rainbow-Ladder (RL) truncation along with an effective model to describe the interaction between the single quarks and by adopting a reduced two-body approximation of the full four-body BSE, firstly used in [120] in which we could describe meson-meson and diquark-antidiquark composite states. In the heavy-light sector (with quark content $Q\bar{Q}q\bar{q}$) a third setup is a hadro-charmonium configuration. We further extended this equation phenomenologically in order to couple it to two-quark states. Altogether, this provides a tool to describe mixed systems as overlaps of two and four-quark states with congruent quantum numbers. Beyond that, the coupled system of equations allows us to disable specific components in order to investigate whether certain internal configurations are dominant or not. We focused on different energy regions (light scalars ≤ 1 GeV, charmonium-like ~ 4 GeV, all-charm $\sim 6-7$ GeV) and probed a number of experimentally confirmed candidates. We found that a four-quark description of many states is appropriate, in some cases even compulsory.

We obtained that the $f_0(500)$ can only be described in a four-quark picture as a $\pi\pi$ resonance and showed that $q\bar{q}$ states are subleading components by coupling the four- with the two-quark BSE. We further showed that this four-quark dominance is an effect of dynamical chiral symmetry breaking: it turns into a two-quark dominance once we increase the quark masses systematically towards the ones of heavier quarks such as the strange quark. We further used the coupled equation in order to describe the heavy-light four-quark candidates $f_0/a_0(980)$. Using RL truncation, we observed that the states are very well described in a pure four-quark picture as we observe an overlap of error bars with the experimental ones by using kaons and diquarks as effective degrees of freedom. Once we enable the $s\bar{s}$ component for a mixed description of the $f_0(980)$, it lowers the mass significantly, but a simple model of beyond RL (BRL) effects indicates that the significance of the $s\bar{s}$ component might be overestimated, here. The BRL model further indicates that the coupling to the light $q\bar{q}$ with $q \in \{u, d\}$ is small. Without exceptions, diquark-antidiquark components only yield negligible corrections.

In the charmonium sector we were able to extract a whole spectrum of hidden- and open-charm candidates and described the $\chi_{c1}(3872)$ and the $Z_c(3900)$ very well as molecular four-quark states consisting of $D\bar{D}^*$. A comparison of the spectra entails that

the open-charm states are lower in mass than the hidden-charm ones in our model. The dominance of the heavy-light mesonic component is ubiquitous; hadro-charmonium components only gain relevance for isovectors. Except for the scalar isoscalar state with hidden charm, diquark-antidiquark components are also negligible in every channel. Coupling the isoscalar four-quark candidates to ordinary charmonia was not done for technical reasons.

For the recently discovered X(6900) we also calculated a whole all-charm spectrum for 0^+ and 1^+ candidates with η_c and J/ψ mesons and axialvector diquarks as ingredients. The meson-meson dominated ground states are too light for a suitable description of the X(6900) in every channel. By contrast, we find possible candidates in the excitation spectra which indicates that the measured resonance corresponds to an excited meson-meson state consisting of η_c and/or J/ψ mesons. Diquark-antidiquark components are only significant in the 0^+ channel.

Uncertainties. Our results in this work are without exceptions qualitative. Concerning this, we should record a few important reasons which we classify as “systematic” and “numerical”.

Let us first turn our attention to the *systematic* uncertainties in the two-body BSE employed in this work. As the foundation of the whole two-body approximation which we apply, we irrevocably omit the irreducible three- and four-body forces of the full four-quark scattering kernel completely. Because of that, an important class of potential components is missing: the ones of tightly arranged quarks whose structure could not be divided into two-quark clusters. Furthermore, the two-body equation is heavily truncated the way we use it since we only consider the leading components of the Bethe-Salpeter amplitudes of the constituent mesons and diquarks. That omits the dynamics of the sub-leading components of the constituent BSAs completely. Although Ref. [126] showed that the effects of including the first sub-leading basis element are small for four-quark states which are effectively consisting of pseudoscalar mesons, we did not do this check for vector mesons and rely on the fact that the leading tensor structure already yields good approximations of the meson properties in the respective channels, cf. Fig. 3.8. The error that results from those systematic simplifications is hardly estimable and because of that, we restrict the results within this work to be qualitative only.

Besides that, there are *numerical* uncertainties such as the extrapolation of eigenvalue curves and BSAs. Also, meson and diquark propagators are fitted in order to be able to compute them efficiently within the diagrams. These numerical approaches together introduce an additional error which is yet controllable and nowhere near as uncertain as the systematic ones for the following reasons: the applied fits are particularly appropriate and based on direct calculations (see e.g. Fig. 3.12) and the extrapolations were done by varying the input points randomly in order to obtain a reliable statistical error.

Altogether, we expect all those uncertainties together not to affect the results on a qualitative level. With regard to this work, this is the case for statements about dominant and sub-dominant components of a physical, mixed state. In fact, the results in this thesis validate our expectation – for example, our findings that the four-quark dominance of the $f_0(500)$ is only present in the energy region where chiral effects dominate are physically meaningful. However, the (seemingly) good accordance of the calculated mass of the

$\chi_{c1}(3872)$ candidate with the experimental value is surely unstable.

Outlook. The calculations we did in this thesis could be considered as groundwork for further research because at quite a few points there is room for further development. For the heavy-light charmonium-like candidates, it will be reasonable to improve the technical treatment of integrals so that it is possible to reduce the length of the extrapolation path. This however is connected to the difficulty of determining the D and D^* amplitudes in the complex plane. With that however, it is technically possible to mix charmonium-like exotics, e.g. the $\chi_{c1}(3872)$, with ordinary charmonia. Together with a description in the complex plane, this would open up the possibility to make first steps towards a description of the width of this fascinating state.

For the spectrum of light scalars an implementation of the (as of yet missing) $\pi\eta$ component will provide the possibility to compare to studies that underline its importance for the $a_0(980)$. The same holds for a proper inclusion of physical (scalar) $q\bar{q}$ components which is directly connected to an improvement of the interaction and/or the consideration of BRL diagrams that push the masses into the right direction. Our results for the “modified Rainbow-Ladder” in section 5.2 are pointing the way ahead, but its implementation is too naive to lead to strong conclusions.

For getting quantitative results, there is no way to bypass the four-body equation. Only *it* includes the dynamics apart from two-body correlations that describe a potential compact tetraquark component of tightly arranged quarks. Therefore, sooner or later, it will be a mandatory step to cross-check the calculations in this work by a four-body calculation as we did in reverse order in this work; in particular, we confirmed most of the the four-body results of [46, 91] in the charmonium sector qualitatively. The comparison with this work would require a consistent implementation of $q\bar{q}$ couplings and complex integrals, but since the two-body equation is derivable from the (truncated) four-body one, a similar approach is imaginable.

Conclusively, this work demonstrated the potential of non-perturbative, functional methods in order to describe physics on the level of exotic four-quark hadrons. We were able to describe a variety of spectra with plausible mass orderings and consistently produced physically meaningful results. With the novel possibilities of coupling four- and two-quark states and the possibility even to describe them in the complex plane as dynamic resonances, the framework of DSEs/BSEs represents an encouraging approach to decode the nature of several exotic hadrons that puzzled the minds of elementary particle physicists for so long.

APPENDIX A

CONVENTIONS

Notations. We consistently use Einstein's sum convention in this thesis, in which one sums over all indices which appear in pairs:

$$a_i b_i = \sum_i a_i b_i \quad (\text{A.1})$$

The contraction of a four vector with the Dirac matrices defines the Feynman slash:

$$\not{p} = \gamma_\mu p^\mu \quad (\text{A.2})$$

Integrals are performed in Euclidean hyperspherical coordinates. For that, we frequently use the shorthand

$$\int_q := \int \frac{d^4 q}{(2\pi)^4} = \frac{1}{(2\pi)^4} \int_0^\infty dq^2 \frac{q^2}{2} \int_{-1}^1 dz \sqrt{1-z^2} \int_{-1}^1 dy \int_0^{2\pi} d\phi \quad (\text{A.3})$$

Euclidean space. In this thesis we consistently work in Euclidean metrics. That means, every four-vector gets redefined,

$$x_0 \rightarrow -ix_0, \quad (\text{A.4})$$

in order to ensure that scalar products are evaluated in a Euclidean way:

$$x_\mu y^\mu = - \sum_i x_i y_i =: -x \cdot y \quad (\text{A.5})$$

We see that the Euclidean scalar product then differs from the Minkowski one by a minus sign and entails that a four vector is spacelike, iff

$$x \cdot y > 0. \quad (\text{A.6})$$

Integrals get Wick rotated [155]:

$$\int_{-\infty(1+i\epsilon)}^{\infty(1+i\epsilon)} dx_0 \rightarrow -i \int_{-\infty}^{\infty} dx_0 \quad (\text{A.7})$$

With that, an integration in four-dimensional spherical coordinates, Eq. (A.3), is possible. Note that this merely corresponds to a relabelling of the zeroth coordinate and does not flaw any calculation. Consistency with calculations in Minkowski space is preserved via the corresponding back-transformations.

Dirac matrices. We have to work with a Euclidean representation of the Dirac matrices in order to not having to redefine the Dirac slash. This concerns the spherical ones, $\mu = 1, 2, 3$. The matrices are given by

$$\gamma_0 = \begin{pmatrix} \mathbb{1} & 0 \\ 0 & -\mathbb{1} \end{pmatrix} \quad \gamma_i = \begin{pmatrix} 0 & -i\sigma_i \\ i\sigma_i & 0 \end{pmatrix} \quad \gamma_5 = \begin{pmatrix} 0 & \mathbb{1} \\ \mathbb{1} & 0 \end{pmatrix} \quad (\text{A.8})$$

where $\mathbb{1} = \mathbb{1}_{2 \times 2}$ and σ_i are the Pauli spin matrices, defined by

$$\sigma_1 = \begin{pmatrix} 0 & 1 \\ 1 & 0 \end{pmatrix} \quad \sigma_2 = \begin{pmatrix} 0 & -i \\ i & 0 \end{pmatrix} \quad \sigma_3 = \begin{pmatrix} 1 & 0 \\ 0 & -1 \end{pmatrix}. \quad (\text{A.9})$$

In that form, the Dirac matrices are Hermitian,

$$\gamma_\mu^\dagger = \gamma_\mu \quad (\text{A.10})$$

The Dirac matrices obey the Clifford algebra anti-commutation relation

$$\{\gamma_\mu, \gamma_\nu\} = 2\delta_{\mu\nu}. \quad (\text{A.11})$$

Slashed expressions are a shorthand for a contraction of a Dirac matrix with a four vector:

$$\not{p} = \gamma_\mu p_\mu \quad (\text{A.12})$$

The four Dirac matrices anti-commute with the fifth Dirac matrix:

$$\{\gamma_\mu, \gamma_5\} = 0 \quad (\text{A.13})$$

Dirac matrices transform as follows under usual transformations:

Transposition.

- $\gamma_\mu^T = (\gamma_0^T, \gamma_1^T, \gamma_2^T, \gamma_3^T) = (\gamma_0, -\gamma_1, \gamma_2, -\gamma_3)$
- $\gamma_5^T = \gamma_5$

Parity transformation.

- $\gamma_\mu \rightarrow \gamma_0(\gamma_0, \gamma_1, \gamma_2, \gamma_3)\gamma_0 = (\gamma_0, -\gamma_1, -\gamma_2, -\gamma_3) = (\Pi\gamma)_\mu$
- $\gamma_5 \rightarrow -\gamma_5$

Charge conjugation.

- $\gamma_\mu \rightarrow \gamma_0 \gamma_2 \gamma_\mu^T \gamma_2^T \gamma_0^T = \gamma_0 \gamma_2 (\gamma_0^T, \gamma_1^T, \gamma_2^T, \gamma_3^T) \gamma_2 \gamma_0 = (-\gamma_0, -\gamma_1, -\gamma_2, -\gamma_3) = -\gamma_\mu$
- $\gamma_5 \rightarrow \gamma_5$

Gell-Mann matrices. The Gell-Mann matrices are the generators of the SU(3) symmetry group. They are given by

$$\begin{aligned}
 \lambda_1 &= \begin{pmatrix} 0 & 1 & 0 \\ 1 & 0 & 0 \\ 0 & 0 & 0 \end{pmatrix} & \lambda_2 &= \begin{pmatrix} 0 & -i & 0 \\ i & 0 & 0 \\ 0 & 0 & 0 \end{pmatrix} & \lambda_3 &= \begin{pmatrix} 1 & 0 & 0 \\ 0 & -1 & 0 \\ 0 & 0 & 0 \end{pmatrix} \\
 \lambda_4 &= \begin{pmatrix} 0 & 0 & 1 \\ 0 & 0 & 0 \\ 1 & 0 & 0 \end{pmatrix} & \lambda_5 &= \begin{pmatrix} 0 & 0 & -i \\ 0 & 0 & 0 \\ i & 0 & 0 \end{pmatrix} & \lambda_6 &= \begin{pmatrix} 0 & 0 & 0 \\ 0 & 0 & 1 \\ 0 & 1 & 0 \end{pmatrix} \\
 \lambda_7 &= \begin{pmatrix} 0 & 0 & 0 \\ 0 & 0 & -i \\ 0 & i & 0 \end{pmatrix} & \lambda_8 &= \frac{1}{\sqrt{3}} \begin{pmatrix} 1 & 0 & 0 \\ 0 & 1 & 0 \\ 0 & 0 & -2 \end{pmatrix} & & (A.14)
 \end{aligned}$$

and define the colour structure of the gluons in the fundamental representation via $\tau_a = \lambda_a/2$ as already mentioned in chapter 3.

APPENDIX B

SOLVING THE QUARK DSE

This chapter includes details about the solution of a quark DSE. We do so for Maris-Tandy interaction, because then the quark DSE could be solved independently from other DSEs.

B.1 Solving on the Real Axis

To solve the quark propagator numerically, we have to determine the two dressing functions $A(p^2)$ and $B(p^2)$ separately. Thus, we project them out on the left side of Eq. (2.37), which looks like

$$\begin{aligned} i\not{p}A(p^2) + B(p^2) &= Z_2 (i\not{p} + Z_m m_{\text{ren}}) \\ &\quad - Z_2^2 C_F \int_q^\Lambda \frac{\mathcal{G}(k^2)}{k^2} \left(\delta_{\mu\nu} - \frac{k_\mu k_\nu}{k^2} \right) \gamma^\mu (-i\not{q}\sigma_\nu(q^2) + \sigma_s(q^2)) \gamma^\nu \\ &=: S_0(p) + c \int^\Lambda R(q, p^2). \quad (c = \text{const.}) \end{aligned} \quad (\text{B.1})$$

Determination of projectors. The set of projectors P_i^{ab} corresponding to a basis $\mathcal{B} = \{b_i^{ab}\}_{1 \leq i \leq n}$ is defined by

$$P_i^{ab} b_j^{ba} = \delta_{ij}. \quad (\text{B.2})$$

Because the dressing functions A and B are scalars, we have to project them out of the tensor structures by performing a Dirac trace. Furthermore, the inner tensor structure of the projector (let's call it p_i) should only depend on the inner structure of the expression that has to be projected. To be more precise, we define projection functions

$$P_i^{ab} x^{ba} = \sum_k \alpha_{ik} b_k^{ab} x^{ba}. \quad (\text{B.3})$$

Combining this with Eq. B.2 and making use of the linearity of the trace operator leads to

$$P_i^{ab} b_j^{ba} = \sum_k b_k^{ab} b_j^{ba} \alpha_{ik} \stackrel{!}{=} \delta_{ij} \quad (\text{B.4})$$

or, equivalently, $B\alpha_i = \delta_i$ with $B_{ij} := \text{tr}(b_j b_i)$, α_{ij} and δ_{ij} as before. This is equivalent to a system of linear equations:

$$\begin{pmatrix} b_1^{ab} b_1^{ba} & b_2^{ab} b_1^{ba} & \dots & b_n^{ab} b_1^{ba} \\ b_1^{ab} b_2^{ba} & b_2^{ab} b_2^{ba} & \dots & b_n^{ab} b_2^{ba} \\ \vdots & \vdots & \ddots & \vdots \\ b_1^{ab} b_n^{ba} & b_2^{ab} b_n^{ba} & \dots & b_n^{ab} b_n^{ba} \end{pmatrix} \begin{pmatrix} \alpha_{i1} \\ \alpha_{i2} \\ \vdots \\ \alpha_{in} \end{pmatrix} = \begin{pmatrix} \delta_{i1} \\ \delta_{i2} \\ \vdots \\ \delta_{in} \end{pmatrix} \quad (\text{B.5})$$

Solving this for the quark DSE with the basis $\mathcal{B} = \{ \mathbf{i}p, \mathbb{1} \}$ yields

$$\begin{aligned} \alpha_1 &= \begin{pmatrix} -1/4p^2 \\ 0 \end{pmatrix} \Rightarrow P_1^{ab} = -\frac{\mathbf{i}p^{ab}}{4p^2} \\ \alpha_2 &= \begin{pmatrix} 0 \\ 1/4 \end{pmatrix} \Rightarrow P_2^{ab} = \frac{\mathbb{1}^{ab}}{4}. \end{aligned} \quad (\text{B.6})$$

Note that this procedure is generally applicable for the determination of projectors, e.g. those for the Bethe-Salpeter amplitudes.

Scalar valued equations. Performing the traces can be done by an algebra evaluation program, e.g. FORM [156] or Mathematica, or by hand using the Dirac trace rules. A suitable Mathematica package for a CPU supported evaluation is given by FeynCalc [157, 158].

With that, the dressing functions can be computed:

$$\begin{aligned} A(p^2, \mu^2) &= Z_2 + Z_2^2 \cdot \frac{1}{3p^2 \pi^3} \int_{q^2, z} \frac{\mathcal{G}(k^2)}{k^2} \left(\frac{2(k \cdot p)(k \cdot q)}{k^2} + (p \cdot q) \right) \sigma_v(q^2, \mu^2) \\ &=: Z_2 + Z_2^2 \cdot \Sigma_A(p^2, \mu^2) \end{aligned} \quad (\text{B.7})$$

$$\begin{aligned} B(p^2, \mu^2) &= Z_2 Z_m m_{\text{ren}}(\mu^2) + Z_2^2 \cdot \frac{1}{\pi^3} \int_{q^2, z} \frac{\mathcal{G}(k^2)}{k^2} \sigma_s(q^2, \mu^2) \\ &=: Z_2 Z_m m_{\text{ren}}(\mu^2) + Z_2^2 \cdot \Sigma_B(p^2, \mu^2) \end{aligned} \quad (\text{B.8})$$

$$Z_2(\mu^2, \Lambda^2) = \frac{1}{1 + Z_2 \cdot \Sigma_A(\mu^2, \mu^2)} \quad (\text{B.9})$$

$$Z_m(\mu^2, \Lambda^2) = \frac{1}{Z_2} - \frac{Z_2 \cdot \Sigma_B(\mu^2, \mu^2)}{m_{\text{ren}}(\mu^2)}. \quad (\text{B.10})$$

Note that in the chiral limit, $m_{\text{ren}}(\mu^2) \rightarrow 0$, the right hand side of Eq. (B.10) is not defined. It is then recommended to calculate the cutoff dependent bare mass $m(\Lambda^2) = Z_m(\mu^2, \Lambda^2) m_{\text{ren}}(\mu^2)$ instead, for which the divergence cancels out.

Once the renormalization constants are determined completely, the functions A and B themselves are determined by the following subtractions of the self energy integral:

$$A(p^2, \mu^2) = 1 + Z_2^2 \cdot (\Sigma_A(p^2, \mu^2) - \Sigma_A(\mu^2, \mu^2)) \quad (\text{B.11})$$

$$B(p^2, \mu^2) = m_{\text{ren}}(\mu^2) + Z_2^2 \cdot (\Sigma_B(p^2, \mu^2) - \Sigma_B(\mu^2, \mu^2)) \quad (\text{B.12})$$

B.2 Continuation into the Complex Plane: The “Shell Method”

As described in the main text, we have a few problems with the quark momentum as the integration momentum in the quark DSE, namely

- the effective coupling \mathcal{G} is constructed for being meaningful on the real axis only, but would be required in the complex plane and
- branch cuts are arising from the angular integral because of singularities in the self energy integrand.

In the Maris-Tandy model for example, the effective coupling and thus, the self energy integral gets singular for

$$e^2 - 1 + \left(1 + \frac{k^2}{\Lambda_{\text{QCD}}^2}\right)^2 = 0. \quad (\text{B.13})$$

The idea is to iterate on shells and use the gluon momentum k as a (real) integration momentum. Given that we know the quark propagator on the real axis, we “open a shell parabola” around the real axis, see the innermost parabola in Fig. B.1. This parabola is characterized by its apex Δ^2 and the condition

$$q^2 = (k \pm \Delta)^2 = k^2 + \Delta^2 \pm 2\sqrt{k^2}\sqrt{\Delta^2}. \quad (\text{B.14})$$

One can easily verify (e.g. with Mathematica) that for any point on this parabola, we only need information from *inside* the parabola itself. Given that, we proceed as follows:

1. We start by setting up the first shell grid. My choice was to characterise any grid point via its shell apex and the contraction in real q^2 direction:

$$q^2 = (k + i\Delta)^2 = k^2 - \Delta^2 + 2i\sqrt{k^2}\sqrt{\Delta^2} \quad (\text{B.15})$$

After some algebra we come to conditions for the apex Δ^2 and the gluon momentum k^2 :

$$\Delta^2 = \frac{1}{2} (|q^2| - \text{Re } q^2) \quad (\text{B.16})$$

$$k^2 = \text{Re } q^2 + \Delta^2 \quad (\text{B.17})$$

This provides the transformation $(\text{Re } q^2, \text{Im } q^2) \rightarrow (\Delta^2, k^2)$ which will be vital for the necessary interpolations. As a cross-check: if we set $\text{Im } q^2 = 0$ we obtain $\Delta^2 = 0$. Thus, the “real” grid is in the correct form and does not have to be transformed, which corresponds to our original DSE solution on the real axis – great!

2. From now on, the iteration momenta are (assuming a numerical calculation) on a 2D grid (Δ^2, k^2) :
 - the k^2 grid can follow a simple quadrature rule

- the Λ^2 grid could e.g. be $\sim i^3$. A linear grid $\sim i$ is not a clever choice since we need to start with very small shells, characterised by very small apices.
3. After extending the grid to a larger Λ^2 , our start guess of the dressing functions on the parabola will be identical to the values of the former one. In the calculation, we only focus on the upper half plane and use $A^*(q^*) = A(q)$ and $B^*(q^*) = B(q)$ afterwards to obtain the values on the lower half plane.
 4. The iteration goes on and we arrive at a function on a (Λ^2, k^2) grid on which we could easily interpolate. If we, for instance, are interested in the function $A(q^2)$ for some $q^2 \in \mathbb{C}$, we must transform q^2 into the 2-tuple (Λ^2, k^2) via Eqs. B.16 and B.17.

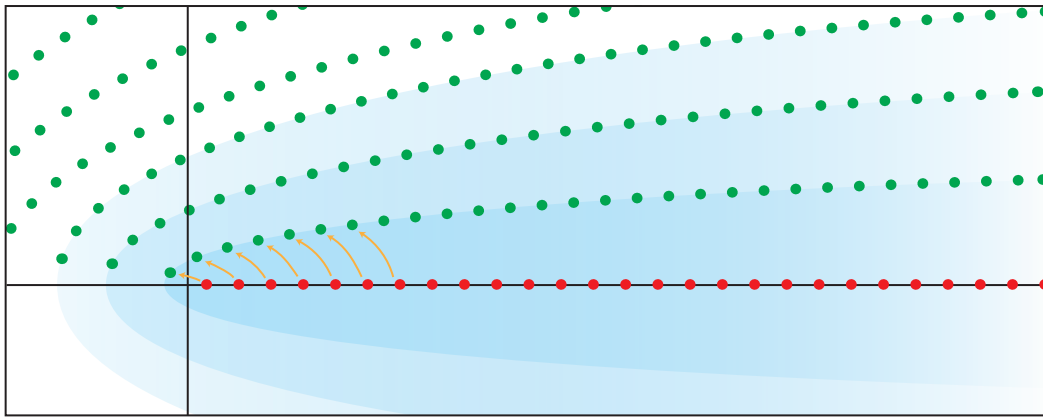


Figure B.1: The principle of the shell method visualized in the complex q^2 plane. From the known solution on the positive real axis we continue into the complex plane by spanning shell parabolas (green dots) around.

APPENDIX C

BSEs

C.1 Two-Quark Case

Similar to the section before, we will now focus on a solution of BSEs using Maris-Tandy interaction.

C.1.1 Index Structure of a Two-Quark BSE

To solve a two-quark Bethe-Salpeter equation, one has to handle the indices correctly. Basically, the quantities inside the BSE are the interaction kernel K (and its rainbow-ladder ingredients Γ_{qg} and D), the quark propagators and the Bethe-Salpeter amplitude. They carry lots of indices, which are summarized in table C.1.

In the following, Dirac indices are given by italic Greek letters (α, β, \dots), colour indices by capital Roman letters (A, B, \dots), flavour indices by small roman letters (a, b, \dots) and Lorentz-indices by upright Greek letters (μ, ν, \dots). Another index, here e is an isospin index. Lorentz-indices of the bound state amplitudes will be suppressed. The BSE index structure is then given by the following equation:

$$\Gamma_{\alpha A a, \beta B b}^e = K_{\alpha A a, \beta B b}^{\sigma S s, \gamma C c} \underbrace{S_{\gamma C c}^{\delta D d} \Gamma_{\delta D d, \rho R r}^e S_{\sigma S s}^{\rho R r}}_{\Psi_{\gamma C c, \sigma S s}^e}, \quad (\text{C.1})$$

whereas

$$\Psi_{\gamma C c, \sigma S s}^e = S_{\gamma}^{\delta} \Gamma_{\delta C c, \rho S s}^e S_{\sigma}^{\rho} = (S \Gamma S)_{\gamma \sigma} \otimes \Gamma_{C S} \otimes \Gamma_{c s}^e. \quad (\text{C.2})$$

quantity	symbol	#Dirac ind.	#colour ind.	#flavour ind.	#Lorentz ind.
interaction kernel	K	4	4	4	0
quark-gluon vertex	Γ^{qg}	2	2	3	1
gluon propagator	D	0	0	2	2
quark propagator	S	2	2	2	0
bound state amplitude	Γ	2	2	3	$n \in \mathbb{N}_0$

Table C.1: All quantities inside the Bethe-Salpeter equation with the number of Dirac-, colour-, flavour- and Lorentz indices.

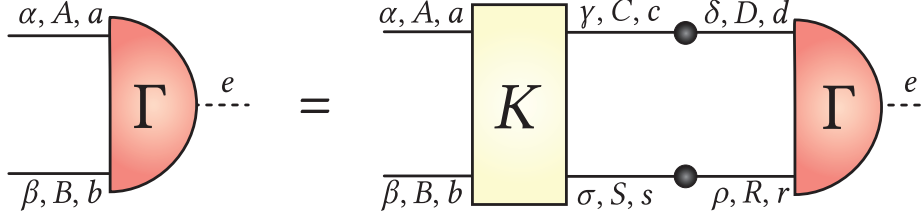


Figure C.1: The index structure of the BSE in a graphical form. The Lorentz indices of the bound state amplitudes are suppressed. Greek letters denote Dirac-, capital roman letters colour and small roman letters flavour indices.

The latter term is the decomposition of Dirac-, flavour and colour index structure. Specifying the kernel to be truncated by Rainbow-Ladder, it is given by

$$\begin{aligned}
K_{\alpha A a, \beta B b}^{\sigma S s, \gamma C c} &= g^2 \left(\Gamma_{\mu}^{\text{qg, bare}} \right)_{\beta B b, i}^{\sigma S s} (D^{\mu\nu})^{ij} \left(\Gamma_{\nu}^{\text{qg}} \right)_{\alpha A a, j}^{\gamma C c} \\
&= g^2 \left(i\gamma_{\mu} \right)_{\beta}^{\sigma} (\tau_i)_B^S \delta_b^s D^{\mu\nu} \delta^{ij} \left(\Gamma_{\nu}^{\text{qg}} \right)_{\alpha}^{\gamma} (\tau_j)_A^C \delta_a^c \\
&= g^2 \left(i\gamma_{\mu} \right)_{\beta}^{\sigma} D^{\mu\nu} \left(\Gamma_{\nu}^{\text{qg}} \right)_{\alpha}^{\gamma} \otimes (\tau_i)_B^S (\tau^i)_A^C \otimes \delta_b^s \delta_a^c \quad (\text{C.3})
\end{aligned}$$

Closing two open quark legs by multiplying $\chi_{\gamma C c, \sigma S s}^e$ leads consequently to the full right hand side of the BSE in Eq. (C.1). We apply the colour and flavour structure of the pion at this point, which means $\Gamma_{CS} = \delta_{CS}$ and $\Gamma_{cs}^e = r_{cs}^e$.

$$\begin{aligned}
\Gamma_{\alpha A a, \beta B b}^e &= K_{\alpha A a, \beta B b}^{\sigma S s, \gamma C c} \chi_{\gamma C c, \sigma S s}^e = g^2 \left(i\gamma_{\mu} \right)_{\beta}^{\sigma} D^{\mu\nu} \left(\Gamma_{\nu}^{\text{qg}} \right)_{\alpha}^{\gamma} (\text{STS})_{\gamma\sigma} \otimes (\tau_i)_B^S (\tau^i)_A^C \delta_{CS} \otimes \delta_b^s \delta_a^c r_{cs}^e \\
&= ig^2 D^{\mu\nu} \left(\Gamma_{\nu}^{\text{qg}} \text{STS} \gamma_{\mu} \right)_{\alpha\beta} \otimes (\tau_i \tau^i)_{AB} \otimes r_{ab}^e \quad (\text{C.4})
\end{aligned}$$

The first structure in Eq. (C.4) is the Dirac part of the BSE and given by a simple matrix multiplication. The second structure is the colour part, which is in the pion case given by $(\tau_i \tau^i)_{AB} = \frac{4}{3} \cdot \delta_{AB}$, reflecting the typical colour trace factor $C_F = \frac{4}{3}$ in front of the left side of the meson BSE. We see, that the flavour structure is completely unaffected by the quark loop, so we do not get a flavour-prefactor.

For convenience, it is often the case that one applies calligraphic superindices $\mathcal{A}, \mathcal{B}, \dots$ to shorten expressions like the bound state amplitude in the following way:

$$\Gamma_{\alpha A a, \beta B b}^e = \Gamma_{\mathcal{A}\mathcal{B}}^e$$

C.1.2 Flavour- and Colour-Space Conventions

A Bethe-Salpeter amplitude as the main part of the wave function has the following space decomposition:

$$\Gamma = \Gamma_{\text{Dirac}} \otimes \Gamma_{\text{Colour}} \otimes \Gamma_{\text{Flavour}} \quad (\text{C.5})$$

The Dirac structure includes its spin and determines its behaviour under parity transformation. If the state is an eigenstate of the charge conjugation operator, it also determines

these properties together with the momentum-dependent coefficients, the dressing functions. The colour- and flavour structure only denote the strong charge and the quark content of a state and could be normalized arbitrarily – in a normalization procedure as described in chapter 3, all conventional prefactors get absorbed within the dressing functions. For flavour part of the two-quark meson amplitudes, we always use the normalization criterion

$$\text{tr} \{ \bar{\Gamma}_{\text{Flavour}} \Gamma_{\text{Flavour}} \} = 2, \quad (\text{C.6})$$

whose choice is motivated by pion physics, where $N_f = 2$ holds. To prevent confusions and to retain comparability, we will use this factor even if $N_f = 2$ does not hold any more. The colour part of mesons however is always normalized by

$$\text{tr} \{ \bar{\Gamma}_{\text{Colour}} \Gamma_{\text{Colour}} \} = N_c = 3. \quad (\text{C.7})$$

It follows that $\Gamma_{\text{Colour}} = \mathbb{1}$ holds in that case. This is not true for diquarks in the antisymmetric colour triplet, which is described by the antisymmetric tensor ε_{ABX} . Here, the colour parts trace out via

$$\varepsilon_{ABX} \varepsilon_{ABY} = 2\delta_{XY}. \quad (\text{C.8})$$

C.1.3 Solving the Two-Quark BSE in Maris-Tandy Interaction

Similar to the quark DSE, the BSEs for pseudoscalar and vector mesons are solved by an iterative procedure as well. This section serves as a brief summary of how to solve the two-quark BSE; further details, also on the quark propagator and baryon BSEs with potential non-RL interactions could be found in [154]. Looking at the Feynman diagram tells us, on what vectors the involved quantities can depend. So, naively assumed, the BSA depends on three four momenta due to the presence of three external legs, namely the total momentum P and the two quark momenta p_{\pm} . Due to momentum conservation at any vertex, and the BSA is one, one degree of freedom is killed and the BSA only depends on two four vectors, for instance the total momentum P and the relative momentum p , which is given by the momentum conservation condition

$$\begin{cases} p_+ = p + \eta P \\ p_- = p + (\eta - 1)P. \end{cases} \quad (\text{C.9})$$

The relative momentum is consequently given by

$$p = \frac{p_+ + p_- - (2\eta - 1)P}{2}. \quad (\text{C.10})$$

In Maris-Tandy interaction, the observables do not depend on η , hence we set it 0.5 in almost every calculation.

Specifying the rest frame such that the BSA only depends on scalars, we obtain three of them, the absolute value of the meson momentum P^2 , the absolute value of the second momentum p^2 and the angle between them, \tilde{z} , such that

$$\Gamma = \Gamma(P^2, p^2, z_p).$$

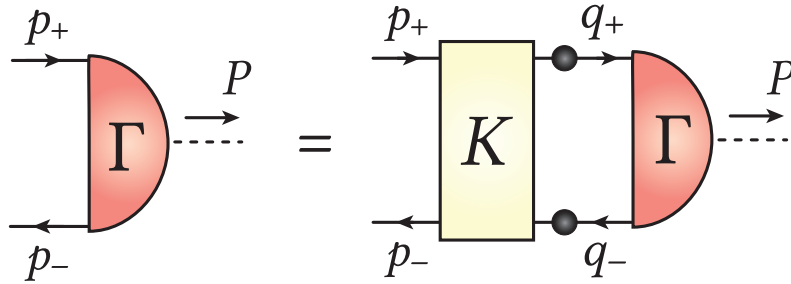


Figure C.2: The homogeneous Bethe-Salpeter equation including the relevant quark and meson momenta. The BSA and the kernel can only depend on the momenta they “feel” – to give an example, the pion BSA on the right hand side of the equation can not depend on p , because the kernel K “sits” between to manipulate the relative quark momentum, “before” the bound state is built. Black blobs denote fully dressed quark propagators.

We solve the mesons in the rest frame¹, hence we specify the total momentum $P = (iM, \mathbf{0})$ and the relative one $p = \sqrt{p^2} (z_p, \sqrt{1 - z_p}, 0, 0)$.² The right hand side of the BSE includes, besides the BSA, the kernel K and a loop, thus we have to introduce a new degree of freedom due to the indeterminate loop momentum q . Due to momentum conservation, the BSA now depends on q and P , while the kernel depends on three momenta, q , p and P . This additional momentum q contributes three additional scalars into the kernel, the loop momentum q^2 and two angles z_q and y_q , such that

$$K = K(P^2, p^2, z_p, q^2, z_q, y_q).$$

These dependencies can also be understood intuitively by looking at Fig. C.2.

In practice, we compute this equation by a matrix multiplication procedure and iterate in course of a power iteration until a convergence criterion is satisfied. As we have done by solving the quark DSE, we calculate the projectors in the same way. This is possible because the equation has a similar form:

$$\begin{aligned} \sum_{i=1}^4 b_i(P, p) F_i(P^2, p^2, z_p) &= \Gamma(P^2, p^2, z_p) \\ &= \sum_{i=1}^4 \int_q K(P^2, p^2, z_p, q^2, z_q, y_q) S(q_+) b_i(P, q) F_i(P^2, q^2, z_q) S(q_-) \end{aligned} \quad (\text{C.11})$$

¹Calculating the moving frame mesons is completely similar to the procedure presented here. The only difference is the higher number of arguments in the functions and consequently the higher numerical effort. We did the calculations for the pion in the moving frame and found no notable deviations from the solutions in the rest frame. The same holds for the leptonic decay constant.

²The other two components of the three momenta are suppressed, because they vanish by a suitable rotation of the coordinate system, as mentioned in chapter 3.

Applying the projectors on both sides yields equations of the form

$$F_i = \sum_{j=1}^4 \int_q \mathcal{K}_{ij} F_j \approx \sum_{j=1}^4 \overline{\sum} \underbrace{(\text{Weights} \times \text{Jacobians} \times \mathcal{K}_{ij})}_{=: K_{ij}} F_j. \quad (\text{C.12})$$

The kernel elements \mathcal{K}_{ij} are now the “traced” quantities with respect to one basis element each and can be calculated/stored separately. Eq. (C.12) shows, how the analytic equation transitions into a numerical one.¹ In practice, one evaluates the integral corresponding to the inner angle y inside the kernel, because the BSA does not depend on this quantity.

Mass iteration procedure. The iteration can be done with the power iteration procedure. In general, we look for the eigenvalue of the BSE for some P^2 . First, we discuss the procedure for a general eigenvalue equation.

Let $f : \mathbb{S} \rightarrow \mathbb{S}$ be an operator and X an element of some algebraic structure \mathbb{S} , e. g. \mathbb{C}^n . X is defined to be an eigenstate of f , if $\exists \lambda \in \mathbb{C}$ such that

$$fX = \lambda X. \quad (\text{C.13})$$

Moreover, let $\|\cdot\| : \mathbb{S} \rightarrow \mathbb{R}_0^+$ be a norm. Then, the recursive sequence $(X_n)_{n \in \mathbb{N}}$ defined by

$$X_n = \frac{fX_{n-1}}{\|fX_{n-1}\|}$$

usually² converges to an eigenstate \hat{X} corresponding to the largest eigenvalue λ_{\max} .³ The eigenvalue is then determined by the eigenvalue equation (C.13) itself. Treating the BSE, $\overline{\sum} K_{ij}$ is equivalent to the operator f and Γ_j is equivalent to the state X . A possible choice for a norm is to set $\|\Gamma\| := |F_1(P^2, p^2 = 1 \text{ GeV}, z = 0)|$.

The convergence criterion is defined by the comparison of the values of F_i before and after one iteration step by a division. Here, we compute the quotient $\lambda = (f \mathcal{K} \Gamma) / \Gamma_i$ for every grid point and put them into a new set $\mathcal{S} := \{ \lambda_i \}$. If

$$\sigma_{\mathcal{S}} := \sqrt{\langle \lambda^2 \rangle - \langle \lambda \rangle^2} < \varepsilon$$

for some small $\varepsilon > 0$, the convergence is defined to be satisfied and $\langle \lambda \rangle$ is the corresponding eigenvalue. A state $\Gamma(P^2)$ can be interpreted as a bound state with mass $M^2 = -P^2$, if $\langle \lambda(P^2) \rangle = 1$. Hence, it is recommended to implement a root finding method for the

¹The overlined sum sign denotes a numerical sum over the integration variables, here $\overline{\sum} = 2\pi \sum_q \sum_z \sum_y$. The factor 2π stems from the fact that we can evaluate one angle trivially.

²The *usual* case is when there is *one* largest eigenvalue in the sense that there are no other ones in the spectrum of f with the same absolute value, i.e. $\exists \lambda_i \in \text{spec}(f) \wedge \nexists \lambda_j \in \text{spec}(f) : |\lambda_j| \geq |\lambda_i|$. Then, only an unfortunate choice of the starting vector X_0 inhibits the convergence.

³Here, a complex value λ_1 is defined to be larger than λ_2 , if $|\lambda_1| > |\lambda_2|$.

function $f(P^2) = \langle \lambda(P^2) - 1 \rangle$, e. g. Newton's method, in which the sequence $(x_n)_n$ with

$$x_n = x_{n-1} - \frac{f(x_{n-1})}{f'(x_{n-1})}$$

converges, if it does, to a root of f . f' denotes the derivative of f , which can be computed numerically with a simple, symmetric difference quotient.

Normalization. The normalization is done by setting $\Gamma(P, p) = \mathcal{N} \Gamma_{\text{norm}}$. Schematically, one can evaluate then the integral

$$\text{tr} \frac{d}{dP^2} \int \bar{\Gamma}(-K, q) S(q_+) \Gamma(K, q) S(q_-) = \mathcal{N}^2 \underbrace{\frac{d}{dP^2} \text{tr} \int \bar{\Gamma}_{\text{norm}} S \Gamma_{\text{norm}} S}_{=1} = \mathcal{N}^2 \quad (\text{C.14})$$

and divide the BSA by the normalization constant \mathcal{N} , which yields the normalized BSA. The charge conjugated BSA is given by Eq. (3.36), e.g. for a pseudoscalar:

$$\bar{\Gamma}(-K, q) = C \Gamma(-K, -q) C^T \quad (\text{C.15})$$

Specifying the basis elements and the dressing functions as $b_i(K, q)$ and $F_i(K, q)$ leads with some calculus to

$$\bar{\Gamma}(-K, q) = C \underbrace{b_i(-K, -q)}_{=b_i(-K, q)} C^T \underbrace{F_i(-K, -q)}_{=F_i(K, q)} = b_i(-K, q) F_i(K, q). \quad (\text{C.16})$$

Transformations. Most generally, the two-body BSAs transform as follows under parity (\mathcal{P}) and charge conjugation (\mathcal{C}):

$$\mathcal{P} (\Gamma^{\mu\nu\dots}(P, p)) = (-1)^J \Pi_{\mu\alpha} \Pi_{\nu\beta} \dots \gamma_0 \Gamma^{\alpha\beta\dots}(\Pi P, \Pi p) \gamma_0 \quad (\text{C.17})$$

$$\mathcal{C} (\Gamma^{\mu\nu\dots}(P, p)) = \gamma_0 \gamma_2 \Gamma^{\mu\nu\dots}(P, -p) \gamma_2 \gamma_0 \quad (\text{C.18})$$

In appendix A we showed how the Dirac matrices transform under those transformations.

Diquarks and Pauli symmetry. Diquarks are coloured objects which could consist of two indistinguishable quarks. If that is the case, the diquark must fulfil Pauli (anti)symmetry. In this thesis, we only use the diquarks from the colour antitriplet coming from $3 \otimes 3 = 6 \oplus \bar{3}$ since two of those diquarks could form a colourless state: $3 \otimes \bar{3} = 8 \oplus \bar{1}$. Pauli symmetry imposes that the wave function must be antisymmetric under the exchange of identical particles. The general wave function consists of spin, colour and flavour, whereas the colour part is always antisymmetric by our choice. That implies that spin and flavour always have the same symmetry (or antisymmetry, respectively). That means that equal-mass diquarks which consist of non-light quarks, i.e. ss or cc , always carry the spin 1. For light quarks, the story is different to the approximate isospin symmetry. Here, it depends on the total isospin: $I = 0$ implies an antisymmetric flavour wave function

and thus a diquark with $J = 0$, whereas $I = 1$ enforces that the diquark has $S = 1$. That makes it directly plausible that the all-charm tetraquark candidate could only have AA as a diquark-antidiquark configuration.

C.2 Four-Quark Case

C.2.1 Precalculations

To be able to solve the four-quark equation in the two-body approximation, one needs the following precalculated quantities:

- quark propagators in the complex plane
- meson and diquark propagators in the complex plane
- meson and diquark Bethe-Salpeter amplitudes (in the complex plane, if mixed with quarkonia and/or described for complex total momenta Q^2)

Quark propagators. The quark propagators are calculated by using the techniques described in appendix B, i.e. the shell method. Here, one has to go as far as possible with the shell apex. When going from the up to the charm quark, possible apices for quarks in the Maris-Tandy model with the standard parameter set are:

quark mass [MeV]	3.8	20.0	50.0	85.5	150	210	350	500	650	795
shell apex [GeV ²]	0.25	0.31	0.39	0.49	0.69	0.85	1.32	1.90	2.45	3.10
M_{crit} [GeV]	2.00	2.23	2.50	2.80	3.32	3.69	4.60	5.51	6.26	7.04

Here, also the critical quark thresholds for the tetraquark masses are given in the last row via $M_{\text{crit}} = 4\sqrt{\Lambda^2}$, which provides information about how heavy the tetraquark could be until quark poles are problematic. We see directly that states like the $f_0(500)$ and $f_0/a_0(980)$ are not restricted by quark thresholds. This is not the case for heavy-light states in the charmonium region. The $\chi_{c1}(3872)$ for example is affected by the poles of the light quark and thus, 2.00 GeV is the limit.

Meson propagators. The meson and diquark propagators are already described in 3.11. Theoretically, it is possible to calculate the whole two-loop integral denoted by $nk^{-1}n$, but we will not do this here as it is connected to much effort. We rather apply the approach firstly applied in [118] to calculate a propagator:

$$D^{-1} = M^2 (nk^{-1}n - n). \quad (\text{C.19})$$

The one loop diagram n is nothing but the normalization integral multiplied with M^{-2} ensuring a dimensionless quantity. The inverse propagator has to behave as follows in the physical limit:

$$D^{-1}(P^2) \xrightarrow{P^2 \rightarrow -M^2} P^2 + M^2 \quad (\text{C.20})$$

Therefore, the derivative in this limit is also given by

$$\left. \frac{dD^{-1}}{dP^2} \right|_{P^2=-M^2} = 1. \quad (\text{C.21})$$

From this asymptotic behaviour we can extract two conditions for the loop integrals n and k :

$$n(-M^2) = k(-M^2) \quad \frac{dn}{dP^2}(-M^2) = M^{-2} + \frac{dk}{dP^2}(-M^2) \quad (\text{C.22})$$

We expand the two-loop integral around the physical point and shift the non-trivial content into an analytical ansatz function f :

$$nk^{-1}n(P^2) \rightarrow nk^{-1}n(-M^2) + \left. \frac{d(nk^{-1}n)}{dP^2} \right|_{P^2=-M^2} \cdot f(P^2) \quad (\text{C.23})$$

with

$$\left. \frac{d(nk^{-1}n)}{dP^2} \right|_{P^2=-M^2} = M^{-2} + \left. \frac{dn}{dP^2} \right|_{P^2=-M^2} =: \alpha \quad (\text{C.24})$$

and the boundary conditions

$$f(-M^2) = 0 \quad \text{and} \quad \left. \frac{df}{dP^2} \right|_{P^2=-M^2} = 1. \quad (\text{C.25})$$

Ref. [118] showed that the function

$$f(P^2) = \frac{M^2}{4} \left(1 + \frac{P^2}{M^2 (P^2/M^2 + 2)^3} \right) \quad (\text{C.26})$$

is a good choice for scalar diquarks and pseudoscalar mesons as well. Note that we differentiate the whole norm integral with respect to P^2 now, not only the quark propagators inside it as done in the normalization procedure. So, the inverse bound state propagator is modeled by

$$D^{-1}(P^2) = M^2 [n(-M^2) - n(P^2) + \alpha f(P^2)]. \quad (\text{C.27})$$

with the definitions above. Doing a cross-check and setting $P^2 = -M^2$ leads to the correct (pointwise) behaviour:

$$D^{-1}(-M^2) = 0 \quad \left. \frac{dD^{-1}}{dP^2} \right|_{P^2=-M^2} = 1. \quad (\text{C.28})$$

The symmetric momentum routing in the equation (see the section C.2.2) enforces that the meson threshold appears at a mass of

$$M_{\text{crit}} = 2 \cdot M. \quad (\text{C.29})$$

Thus, for pions as ingredients, the threshold is at about 0.28 GeV; for the ω we are at 1.5 GeV. The thresholds of other configurations could be calculated straightforwardly.

Meson and diquark amplitudes. The amplitudes are calculated as described in 3.12. For the standard momentum routing for the tetraquark BSE (see next section) on the real axis, the amplitudes are only required on the real axis. This is especially good if we could

easily access the physical solution of the two-quark BSE via iteration. For extrapolated amplitudes such as the D/D^* amplitudes and the ones of heavy-light scalar and axialvector diquarks it was the only possibility in this thesis to do the extrapolations on the real axis. In the complex plane one would have to deal with many more complexities.

C.2.2 Structure

The BSE kernel diagrams are structurally given by Fig. C.3 including the kinematics we choose. First, we focus only on the first diagram, which is in this form a meson-meson interaction kernel. We also denote loops by grey circle arrows and see immediately that the diagram is a two-loop one. As a term, it reads

$$\begin{aligned}
& S(l - Q/4) \Gamma_{11}(p + Q/2, l + p/2) S(l + p + Q/4) \Gamma_{22}(q - Q/2, l + p + q/2) \\
& \times S(l + p + q - Q/4) \Gamma_{12}(p - Q/2, l + p/2 + q) S(l + q + Q/4) \Gamma_{21}(q + Q/2, l + q/2) \\
& \times D_{21}(q + Q/2) D_{22}(q - Q/2) \\
& \times \Phi(Q, q). \tag{C.30}
\end{aligned}$$

One can see that the relative momenta of the amplitudes Γ_{ij} do not depend on the total momentum Q any more – thus, we only need those amplitudes on the real axis in this argument. This is a fortunate circumstance since a complex description is much more expensive than a real one for BSAs. This changes when we look at the other diagrams. The second one reads

$$S(q - Q/2) \Gamma_{12}(p - Q/2, q - p/2 - Q/4) S(q - p) \Gamma_{11}(p + Q/2, q - p/2 + Q/4) S(q + Q/2) \Gamma^*(Q, q), \tag{C.31}$$

and the third one

$$\begin{aligned}
& K(Q, p, l) \\
& \times S(l + Q/2) \Gamma_{21}(q + Q/2, l - q/2 + Q/4) S(l - q) \Gamma_{22}(q - Q/2, l - q/2 - Q/4) S(l - Q/2) \\
& \times D_{21}(q + Q/2) D_{22}(q - Q/2) \\
& \times \Phi(Q, q). \tag{C.32}
\end{aligned}$$

Here, the amplitudes Γ_{ij} are required in the complex plane since the relative momentum squared gets contributions from $Q^2 < 0$ (assuming physical, positive masses with $Q^2 = -M^2$).

Flavour. The flavour part of the diagrams is relatively easily constructed. It follows the same order as Eqs. (C.30–C.32). The flavour wave functions for the different mesons are given as follows:

$$\pi^0 = \begin{pmatrix} 1 & 0 \\ 0 & -1 \end{pmatrix} \quad \pi^+ = \sqrt{2} \begin{pmatrix} 0 & 1 \\ 0 & 0 \end{pmatrix} \quad \pi^- = (\pi^+)^T \tag{C.33}$$

$$K^+ = \sqrt{2} \begin{pmatrix} 0 & 0 & 1 \\ 0 & 0 & 0 \\ 0 & 0 & 0 \end{pmatrix} \quad K^0 = \sqrt{2} \begin{pmatrix} 0 & 0 & 0 \\ 0 & 0 & 1 \\ 0 & 0 & 0 \end{pmatrix} \quad K^- = (K^+)^T \quad \bar{K}^0 = (K^0)^T \tag{C.34}$$

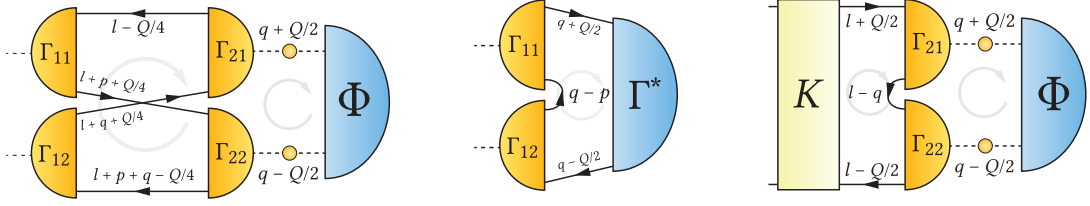


Figure C.3: The loop diagrams inside the (mixed) two-body tetraquark BSE. The leftmost diagram is the only one that contributes to the pure tetraquark BSE without mixing effects. The fourth diagram, which we not show here is only a simple meson BSE and adopts its kinematics, which are already discussed in the last section about two-quark BSEs.

The wave functions for the D/D^* mesons are similar to the ones of the K mesons, merely in a 4×4 dimensional space. The wave functions are normalized such that $\text{tr}(M_1 M_2) = 2$. Diquark wave functions are constructed analogously. With that, the flavour traces of the diagrams could be taken easily. Linear combinations of different four-quark amplitudes¹ have to be constructed such that the four-quark amplitudes are normalized via $\text{tr}(\Psi\bar{\Psi}) = 4$.

Colour. The colour structure is where mesons and diquarks differ. Mesons are in the colour singlet and diquarks are in the antisymmetric colour triplet with associated wave function of

$$M = \delta_{AB} \quad \text{and} \quad D = \varepsilon_{ABX}. \quad (\text{C.35})$$

With that, the diquark amplitude has an additional, third index X which gets contracted with the two-body amplitude Φ . It then has a colour wave function of

$$\Phi_{\text{col}} = \delta_{XY} \quad (\text{C.36})$$

to ensure a colourless (physical) configuration.

C.2.3 Complications

We have to deal with several complications here. In general, the first and obvious one is the location of poles in the integration region. When we are far below the meson threshold, this is not much of a problem, but going very close or even above the threshold induces numerical artefacts if one does not counter them in some sense. That means, in a practical calculation one should not evaluate the eigenvalue curve directly below the threshold, but a bit more below. This is a numerical issue because the functions in the proximity of poles in the integration region are not slowly varying. Since the handling of the number of integration points is always an economic choice, one does not simply increase the number of points arbitrarily, but stays away from the questionable region.

When we go above the threshold, we have to do the path deformation. In principle, this is simple to do, but one has to take care about the influence on other poles in the

¹e.g. $D^0(\bar{D}^*)^0 + D^+(\bar{D}^*)^- + D^-(\bar{D}^*)^+$ for the $\chi_{c1}(3872)$

equation. If we avoid meson poles with a path deformation, it is possible that we catch other poles, such as those coming from diquarks. This is shown in Fig. 4.5 where the effective integration domain for q_{\pm} goes into a region where other poles might lie. It has to be checked in every case if that's a problem. If we enable quarkonium mixing, one would have to check as well if quark poles are hit. Also, the meson propagators should be well-defined in the area left from the meson pole in Fig. 4.5. If this is not the case from the fit functions (which are constructed in a way that it yields good results in the space-like region), it is always a possibility to switch to bare propagators. Usually, they deliver also good results since the non-trivial corrections are suppressed by the UV-behaviour of the BSAs inside the diagrams (cf. Fig. C.3).

APPENDIX D

NUMERICAL TOOLKIT

Gauß Quadrature

In order to evaluate integrals in this work, we use the numerical method of Gauß Quadrature in which one first assumes that an integral over a function $f(x)$ could be expressed via a weight function $\omega(x)$ and a remainder $g(x)$:

$$\int_a^b dx f(x) = \int_a^b \omega(x)g(x) dx \quad (\text{D.1})$$

The quadrature rule is always connected to a specific set of orthogonal polynomials, where the associated inner product is defined via the characteristic weight function $\omega(x)$ in the following sense:

$$(f, g)_\omega = \int_a^b \omega(x)f(x)g(x) dx \quad (\text{D.2})$$

This leads to a sophisticated approximation of one-dimensional integrals by a weighted sum:

$$\int_a^b f(x) dx \approx \sum_i w_i f(x_i) \quad (\text{D.3})$$

With this description it is possible to evaluate integrals over polynomials with degree $2n - 1$ exactly by using only n sampling points [159]. The weights w_i and the sampling points x_i are determined by properties of the chosen polynomial. In this work we always use the Legendre polynomials to do so, unless we evaluate angular integrals which go like $f(z) = \sqrt{1 - z^2} \cdot g(z)$; in this case, we use Chebyshev polynomials since in this case, the weight function $\omega_{\text{cheby}} = (1 - z^2)^{-1/2}$ cancels this factor. The sampling points of an integration rule of a polynomial $p(x)$ are given by its zeroes:

$$\{x_i : p(x_i) = 0\} \quad (\text{D.4})$$

The weights are calculated via [160]

$$w_i = \frac{a_n}{a_{n-1}} \frac{\int_a^b \omega(x)p_{n-1}(x)^2 dx}{p'_n(x_i)p_{n-1}(x_i)} \quad (\text{D.5})$$

where a_j is the coefficient of the highest order term of a polynomial of degree j . p_n denotes the polynomial of degree n and p' is the derivative.

For the Gauß-Legendre integration we used a C routine which is given in [161].

Newton's method

For root-finding, we use Newton's method. The idea is to approximate a zero of a function $f(x)$ by generating tangents iteratively and subsequently searching the zeroes of this tangent. If we start at some guess value x_0 , the sequence $(x_i)_{i \geq 0}$ is defined recursively via

$$x_i = x_{i-1} - \frac{f(x_{i-1})}{f'(x_{i-1})} \quad (\text{D.6})$$

where the prime symbol denotes the first derivative. Numerically, we could iterate the values x_i until a convergence criterion, e.g. $f(x_i) < \varepsilon$ for some small $\varepsilon > 0$ is satisfied. Other than the bisection method for example, Newton's is not necessarily converging.

Solving for Eigenvalues

For solving for eigenvalues in this work, we used the power method if we are only interested in the largest eigenvalue and the Eigen library [162] for C++ if we need to get knowledge about the subleading eigenvalues as well. The power method is described already in appendix C and for the methods used in the Eigen library we refer to the documentation [162].

Interpolation

For the interpolations used in this work we used one- and two-dimensional cubic Hermite spline interpolations. All interpolation routines were coded by myself in course of this project. The associated mathematical description could be taken e.g. from [163] or from various textbooks about numerical mathematics.

Schlessinger-Point Method

The Schlessinger-Point method (SPM) is an interpolation method with continued fractions with which it is possible to continue functions analytically which are only given at specific points [125]. If we have a set of n data points we interpolate between those points by using a rational function

$$f(x) = \frac{p(x)}{q(x)} = \frac{f_1}{1 + \frac{a_1(x-x_1)}{1 + \frac{a_2(x-x_2)}{1 + \dots}}} \quad (\text{D.7})$$

The coefficients are determined recursively via

$$a_1 = \frac{f_1/f_2 - 1}{x_2 - x_1} \quad (\text{D.8})$$

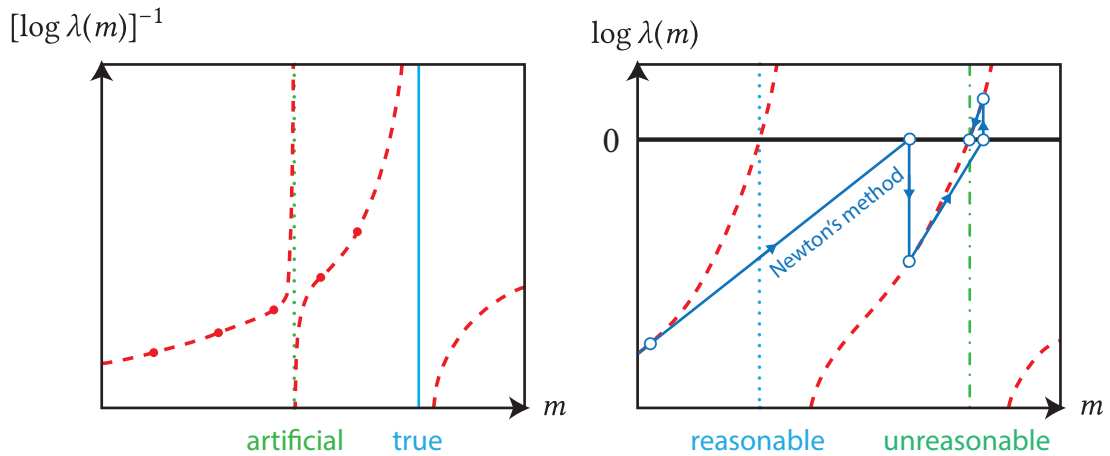


Figure D.1: We show possible issues by using the SPM. *Left hand side:* The big red dots are the input points, the red (dashed) line is the resulting rational function from the SPM. The green (dotted) line is the artificial pole that appears due to numerical inaccuracies. The blue (solid) line denotes the true pole which corresponds to a solution of the eigenvalue curve (where $\log \lambda(m) = 0$). *Right hand side:* We show the possible overstepping of a reasonable solution (denoted by the blue, dotted line) and as a result, an unreasonable solution (blue, erratic dashed/dotted line) which was obtained by an unfit starting point of the Newton's method (dark blue, solid line).

and

$$a_i = \frac{1}{x_i - x_{i+1}} \left(1 + \frac{a_{i-1}(x_{i+1} - x_{i-1})}{1+} \frac{a_{i-2}(x_{i+1} - x_{i-2})}{1+} \dots \frac{a_1(x_{i+1} - x_1)}{1 - f_1/f_{i+1}} \right). \quad (\text{D.9})$$

A very nice overview of what is possible with this method on the basis of spectral functions is given in [164].

Artificial poles. Mostly, we use this continuation for eigenvalue curves $\lambda(m)$ so that we search for the value $\lambda(m) = 1$. Then, it is advisable to transform the input tuples (m_i, λ_i) where $\lambda_i := \lambda(m_i)$ to tuples like $(m_i, 1/\log(\lambda_i))$. Then, it is possible to search for the solution by looking for poles. However, we should distinguish between *true* and *artificial* poles. This distinction could be understood easily: the SPM is an interpolation and not a fit that assumes a certain structure and minimizes errors of fit parameters. Conversely, it generates a (rational) function where all points are truly lying on the function itself. In numerical calculations, we are technically restricted in evaluating mathematical expressions – we generally have to assume that not a single point is evaluated exactly – at least, the 64 bit architecture of our CPU only makes it possible to describe real numbers in a certain precision. The SPM produces rational functions which establish a number of *artificial* poles; these poles will compensate the inaccuracy of our numerics and are only providing corrections. The corresponding residues are small, but non-zero and might lead to *artificial* solutions when applying a numerical pole finder. Therefore, these poles have to be excluded, e.g. by setting an acceptance threshold for residues, i.e. all poles will be accepted by the algorithm which have a residue larger than some $\text{Res}_{\text{threshold}} > 0$. The distinction between artificial and real poles is shown

graphically on the left side of Fig. D.1.

Wrong solutions. A further point is the localization of unreasonable poles. This could be understood by the following: the easiest way of locating poles is to invert the function and to look for zeroes. The residue is then given by the inverse slope of the function at the zero of interest. By implementing a Newton's root-finding method, we iteratively estimate the location of a zero of the function step by step by looking for the zero of a tangent. If the first derivative is not slowly varying, the root-finder might skip the pole of interest and finds a pole which is lying in an unreasonable region. We will therefore do a further restriction besides the one about residues: we will only accept poles in a specific interval $[m_{\min}, m_{\max}]$, where this region is chosen generously around the point where we expect the pole to be roughly. This position could be estimated e.g. by using a polynomial fit of the function. The problem of overstepping the *reasonable* pole by applying Newton's method on the curve $\log \lambda(m)$ is visualized on the right hand side of Fig. D.1.

Error estimation. We use this method also to perform an error estimation. Say we have n input points from a direct calculation of a function f which make a set of 2-tuples,

$$\mathcal{S}_n = \{ (m_i, \lambda_i) : i \in \mathbb{N}, i \leq n \}. \quad (\text{D.10})$$

Then, we choose a number j with $0 < j \leq n$ and generate a set of all subsets of \mathcal{S}_n with cardinality j :

$$\mathcal{S}_j := \{ \mathcal{S}_j : \mathcal{S}_j \subseteq \mathcal{S}_n, |\mathcal{S}_j| = j \} \quad (\text{D.11})$$

From that, we define vectors whose elements are 2-tuples and which span a set of all possible permutations of all elements of the subsets \mathcal{S}_m as follows:

$$\Omega_j := \{ x : x \in (\mathbb{C} \times \mathbb{C})^j, x_i \in X \in \mathcal{S}_j, x_i \neq x_k \forall i \neq k \} \quad (\text{D.12})$$

Then, we condense many sets of the kind (D.12), viz.

$$\Omega = \bigcup_{j=j_{\min}}^n \Omega_j \quad (\text{D.13})$$

for $j_{\min} \gg 0$ in order to vary the number of input points as well. Ω then contains all possible permutations of $j \geq j_{\min}$ input points which are part of \mathcal{S}_j , in every possible order. For every of those permutations, each represented by a vector x we apply the SPM in order to search for a BSE solution. Thus, we would have to perform

$$N = \sum_{j=j_{\min}}^n \binom{n}{j} \cdot j! \quad (\text{D.14})$$

continuations. From each of those continuations we obtain a solution for a certain mass m . If this solution satisfies the conditions (sufficiently large residue and within the

acceptance interval) we put the corresponding masses into a solution set

$$\mathcal{M} := \{ m : m \text{ corresponds to an accepted solution} \}. \quad (\text{D.15})$$

From that we define the mean value \bar{m} and the standard deviation $\sigma_{\mathcal{M}}$ from this set in order to obtain an extrapolated solution and a corresponding error:

$$M = \bar{m} \pm \sigma_{\mathcal{M}} \quad (\text{D.16})$$

The N from Eq. (D.14) is usually a very large number due to the factorial of j . In practice, the effects of these reorderings on the results are very small. Thus, it is sufficient to consider only the different (unordered) sets within S_j , counted by the binomial coefficient.

APPENDIX E

TECHNICAL TOOLS

Programming

By solving the tetraquark BSE, it is necessary to apply an efficient way of performing numerical calculations. For this work, we used *C++* as a programming language by using the *GNU Compiler Collection* (GCC) [165]. Various scripts were written in *Python 3* [166].

Algebra Calculus

Much algebra was done by dedicated evaluation programs. We recommend *Wolfram Mathematica* [167], especially the package *FeynCalc* [157, 158] to determine the BSA basis elements, the projectors and to simplify the algebraic expressions in order to implement them into the program code. We wish to emphasize the efficient optimization features of *FORM* [156], which saved us a factor of 8 in terms of CPU time for solving the tetraquark BSE.

Plotting and Graphics

We consistently used *gnuplot* for data plots in this work [168]. For embedding the plots into this work, we used the terminals *tikz* and *epslatex*. For figures which serve as an illustration of several things we used *Inkscape* [169] and *Adobe Illustrator* [170].

Typesetting

This work was written in \LaTeX [171] using the \TeX Live setup [172].

BIBLIOGRAPHY

- [1] F. Guo, C. Hanhart, U. Meißner, Q. Wang, Q. Zhao and B. Zou, *Rev. Mod. Phys.* **90** 015004 (2018), arXiv:1705.00141 [hep-ph]  
- [2] A. Esposito, A. Pilloni and A. D. Polosa, *Phys. Rept.* **668** 1–97 (2017), arXiv:1611.07920 [hep-ph]  
- [3] J. Goldstone, S. Abdus and S. Weinberg, *Phys. Rev.* **127** 965–970 (1962)  
- [4] R. J. Jaffe, *Phys. Rev. D* **15** 0 (1977) 
- [5] J. D. Weinstein and N. Isgur, *Phys. Rev. D* **41** 2236 (1990) 
- [6] S. Choi and others, *Phys. Rev. Lett.* **91** 262001 (2003), arXiv:hep-ex/0309032  
- [7] N. Brambilla, S. Eidelman, C. Hanhart, A. Nefediev, C. Shen, C. E. Thomas, A. Vairo and C. Yuan, *Phys. Rept.* **873** 1–154 (2020), arXiv:1907.07583 [hep-ex]  
- [8] A. Esposito, A. L. Guerrieri, F. Piccinini, A. Pilloni and A. D. Polosa, *Int. J. Mod. Phys. A* **30** 1530002 (2015), arXiv:1411.5997 [hep-ph]  
- [9] H. Chen, W. Chen, X. Liu and S. Zhu, *Phys. Rept.* **639** 1–121 (2016), arXiv:1601.02092 [hep-ph]  
- [10] M. B. Voloshin, *Prog. Part. Nucl. Phys.* **61** 455–511 (2008), arXiv:0711.4556 [hep-ph]  
- [11] S. L. Olsen, T. Skwarnicki and D. Zieminska, *Rev. Mod. Phys.* **90** 015003 (2018), arXiv:1708.04012 [hep-ph]  
- [12] M. F. M. Lutz and others, arXiv:0903.3905 [hep-ex] 
- [13] R. Aaij and others, *Sci. Bull.* **65** 1983–1993 (2020), arXiv:2006.16957 [hep-ex]  
- [14] A. Hosaka, T. Iijima, K. Miyabayashi, Y. Sakai and S. Yasui, *PTEP* **2016** 062C01 (2016), arXiv:1603.09229 [hep-ph]  
- [15] X. Dong, F. Guo and B. Zou, *Progr. Phys.* **41** 65–93 (2021), arXiv:2101.01021 [hep-ph]  
- [16] S. Dubynskiy and M. B. Voloshin, *Phys. Lett. B* **666** 344–346 (2008), arXiv:0803.2224 [hep-ph]  
- [17] R. L. Jaffe, *Phys. Rept.* **409** 1–45 (2005), arXiv:hep-ph/0409065  
- [18] A. Ali, J. S. Lange and S. Stone, *Prog. Part. Nucl. Phys.* **97** 123–198 (2017), arXiv:1706.00610 [hep-ph]  

- [19] E. Klempt and A. Zaitsev, *Phys. Rept.* **454** 1–202 (2007), arXiv:0708.4016 [hep-ph]  
- [20] D. Horn and J. Mandula, *Phys. Rev. D* **17** 898 (1978) 
- [21] L. Maiani, F. Piccinini, A. Polosa and V. Riquer, *Phys. Rev. D* **71** 014028 (2005), arXiv:hep-ph/0412098  
- [22] Y. Cui, X. Chen, W. Deng and S. Zhu, *HEP NP* **31** 7–13 (2007), arXiv:hep-ph/0607226 
- [23] P. Shi, F. Huang and W. Wang, *Phys. Rev. D* **103** 094038 (2021), arXiv:2105.02397 [hep-ph]  
- [24] K. G. Wilson, *Phys. Rev. D* **10** 8 (1974) 
- [25] Z. Fodor and C. Hoelbling, *Rev. Mod. Phys.* **84** 449 (2012), arXiv:1203.4789 [hep-lat]  
- [26] G. Colangelo and others, *Eur. Phys. J. C* **71** 1695 (2011), arXiv:1011.4408 [hep-lat]  
- [27] S. Prelovsek, T. Draper, C. B. Lang, M. Limmer, K. Liu, N. Mathur and D. Mohler, *Phys. Rev. D* **82** 094507 (2010), arXiv:1005.0948 [hep-lat]  
- [28] S. Prelovsek and L. Leskovec, *Phys. Rev. Lett.* **111** 192001 (2013), arXiv:1307.5172 [hep-lat]  
- [29] S. Prelovsek, C. B. Lang, L. Leskovec and D. Mohler, *Phys. Rev. D* **91** 014504 (2015), arXiv:1405.7623 [hep-lat]  
- [30] P. Bicudo and M. Wagner, *Phys. Rev. D* **87** 114511 (2013), arXiv:1209.6274 [hep-ph]  
- [31] P. Bicudo, K. Cichy, A. Peters and M. Wagner, *Phys. Rev. D* **93** 034501 (2016), arXiv:1510.03441 [hep-lat]  
- [32] P. Bicudo, M. Cardoso, A. Peters, M. Pflaumer and M. Wagner, *Phys. Rev. D* **96** 054510 (2017), arXiv:1704.02383 [hep-lat]  
- [33] A. Francis, R. J. Hudspith, R. Lewis and K. Maltman, *Phys. Rev. Lett.* **118** 142001 (2017), arXiv:1607.05214 [hep-lat]  
- [34] L. Leskovec, S. Meinel, M. Pflaumer and M. Wagner, *Phys. Rev. D* **100** 014503 (2019), arXiv:1904.04197 [hep-lat]  
- [35] M. Padmanath, C. B. Lang and S. Prelovsek, *Phys. Rev. D* **92** 034501 (2015), arXiv:1503.03257 [hep-lat]  
- [36] C. Alexandrou, J. Berlin, B. M. Dalla, J. Finkenrath, T. Leontiou and M. Wagner, *Phys. Rev. D* **97** 034506 (2018), arXiv:1711.09815 [hep-lat]  
- [37] A. Francis, R. J. Hudspith, R. Lewis and K. Maltman, *Phys. Rev. D* **99** 054505 (2019), arXiv:1810.10550 [hep-lat]  
- [38] G. Eichmann, H. Sanchis-Alepuz, R. Williams, R. Alkofer and C. S. Fischer, *Prog. Part. Nucl. Phys.* **91** 1–100 (2016), arXiv:1606.09602 [hep-ph]  
- [39] C. D. Roberts and A. G. Williams, *Prog. Part. Nucl. Phys.* **33** 477–575 (1994), arXiv:hep-ph/9403224  

- [40] C. S. Fischer, *J. Phys. G* **32** R253–R291 (2006), arXiv:hep-ph/0605173  
- [41] P. Maris and C. D. Roberts, *Int. J. Mod. Phys. E* **12** 297–365 (2003), arXiv:nucl-th/0301049  
- [42] A. Bashir, L. Chang, I. C. Cloet, B. El-Bennich, Y. Liu, C. D. Roberts and P. C. Tandy, *Commun. Theor. Phys.* **58** 79–134 (2012), arXiv:1201.3366 [nucl-th]  
- [43] P. Maris, C. D. Roberts and P. C. Tandy, *Phys. Lett. B* **420** 267–273 (1998), arXiv:nucl-th/9707003  
- [44] G. Eichmann, R. Alkofer, A. Krassnigg and D. Nicmorus, *Phys. Rev. Lett.* **104** 201601 (2010), arXiv:0912.2246 [hep-ph]  
- [45] R. Williams, *Phys. Lett. B* **798** 134943 (2019), arXiv:1804.11161 [hep-ph]  
- [46] P. C. Wallbott, G. Eichmann and C. S. Fischer, *Phys. Rev. D* **100** 014033 (2019), arXiv:1905.02615 [hep-ph]  
- [47] G. Eichmann, C. S. Fischer and W. Heupel, *Phys. Lett. B* **753** 282–287 (2016), arXiv:1508.07178 [hep-ph]  
- [48] M. Q. Huber, C. S. Fischer and H. Sanchis-Alepuz, *Eur. Phys. J. C* **80** 1077 (2020), arXiv:2004.00415 [hep-ph]  
- [49] S. Scherer, *Adv. Nucl. Phys.* **27** 277 (2003), arXiv:hep-ph/0210398 
- [50] C. Hanhart, F. Guo and U. Meissner, arXiv:0912.0435 [hep-ph] 
- [51] S. Weinberg, *Phys. Rev.* **130** 776–783 (1963) 
- [52] S. Weinberg, *Phys. Rev.* **137** B672–B678 (1965) 
- [53] H. G. t’Hooft, *Nucl. Phys. B* **72** 461 (1974) 
- [54] E. Witten, *Nucl. Phys. B* **160** 57–115 (1979) 
- [55] E. Witten, *Annals Phys.* **128** 363 (1980) 
- [56] F. Giacosa, *Phys. Rev. D* **75** 054007 (2007), arXiv:hep-ph/0611388  
- [57] F. Giacosa, *Phys. Rev. D* **74** 014028 (2006), arXiv:hep-ph/0605191  
- [58] J. R. Pelaez, *Phys. Rev. Lett.* **92** 102001 (2004), arXiv:hep-ph/0309292  
- [59] J. R. Pelaez and G. Rios, *Phys. Rev. Lett.* **97** 242002 (2006), arXiv:hep-ph/0610397  
- [60] F. E. Close and N. A. Tornqvist, *J. Phys. G* **28** R249–R267 (2002), arXiv:hep-ph/0204205  
- [61] D. Parganlija, F. Giacosa and D. H. Rischke, *Phys. Rev. D* **82** 054024 (2010), arXiv:1003.4934 [hep-ph]  
- [62] J. R. Pelaez, *Phys. Rept.* **658** 1 (2016), arXiv:1510.00653 [hep-ph]  

- [63] V. A. Novikov, L. B. Okun, M. A. Shifman, A. I. Vainshtein, M. B. Voloshin and V. I. Zakharov, Phys. Rev. Lett. **38** 626 (1977), [↗](#)
- [64] M. Nielsen, F. S. Navarra and S. H. Lee, Phys. Rept. **497** 41–83 (2010), arXiv:0911.1958 [hep-ph] [↗](#) [↗](#)
- [65] R. M. Albuquerque, J. M. Dias, K. P. Khemchandani, T. A. Martínez, F. S. Navarra, M. Nielsen and C. M. Zanetti, J. Phys. G **46** 093002 (2019), arXiv:1812.08207 [hep-ph] [↗](#) [↗](#)
- [66] A. Dobado and J. R. Pelaez, Phys. Rev. D **56** 3057–3073 (1997), arXiv:hep-ph/9604416 [↗](#) [↗](#)
- [67] M. R. Pennington and S. D. Protopopescu, Phys. Rev. D **7** 1429–1441 (1973), [↗](#)
- [68] S. M. Roy, Phys. Lett. B **36** 353–356 (1971) [↗](#)
- [69] J. A. A. Alves and others, JINST **3** S08005 (2008) [↗](#)
- [70] R. Aaij and others, Phys. Rev. D **95** 012002 (2017), arXiv:1606.07898 [hep-ex] [↗](#) [↗](#)
- [71] R. Aaij and others, Phys. Rev. Lett. **118** 022003 (2017), arXiv:1606.07895 [hep-ex] [↗](#) [↗](#)
- [72] R. Aaij and others, Phys. Rev. Lett. **115** 072001 (2015), arXiv:1507.03414 [hep-ex] [↗](#) [↗](#)
- [73] R. Aaij and others, Phys. Rev. Lett. **110** 222001 (2013), arXiv:1302.6269 [hep-ex] [↗](#) [↗](#)
- [74] R. Aaij and others, Phys. Rev. Lett. **125** 242001 (2020), arXiv:2009.00025 [hep-ex] [↗](#) [↗](#)
- [75] R. Aaij and others, Phys. Rev. D **102** 112003 (2020), arXiv:2009.00026 [hep-ex] [↗](#) [↗](#)
- [76] LHCb Collaboration, Website, http://lhcb.web.cern.ch/lhcb_page/collaboration/organization/lhcb-cb/default.htm (state: 19.07.2021)
- [77] BESIII Experiment: *Brief Introduction*, Website, <http://english.ihep.cas.cn/bes/doc/2124.html> (state: 19.07.2021)
- [78] D. Asner and others, Int. J. Mod. Phys. A **24** S1–794 (2009), arXiv:0809.1869 [hep-ex] [↗](#)
- [79] W. Altmannshofer and others, PTEP **2019** 123C01 (2019), arXiv:1808.10567 [hep-ex] [↗](#) [↗](#)
- [80] KEK, High Energy Accelerator Research Organization: *SuperKEKB collider achieves the world's highest luminosity*, blog article, <https://www.kek.jp/en/newsroom/2020/06/26/1400/> (state: 19.07.2021)
- [81] BELLE Collaboration, Website, <https://belle2.jp/the-collaboration/> (state: 19.07.2021)
- [82] K. Peters, L. Schmitt, T. Stockmanns and J. Messchendorp, Nucl. Phys. News **27** 24–28 (2017) [↗](#)
- [83] G. Barucca and others, Eur. Phys. J. A **55** 42 (2019), arXiv:1812.05132 [hep-ex] [↗](#) [↗](#)
- [84] H. A. Ahmed and C. W. Xiao, Phys. Rev. D **101** 094034 (2020), arXiv:2001.08141 [hep-ph] [↗](#) [↗](#)
- [85] S. S. Agaev, K. Azizi and H. Sundu, Phys. Lett. B **789** 405–412 (2019), arXiv:1804.02519 [hep-ph] [↗](#) [↗](#)

- [86] J. J. Dudek, R. G. Edwards and D. J. Wilson, Phys. Rev. D **93** 094506 (2016), arXiv:1602.05122 [hep-ph]  
- [87] L. Maiani, F. Piccinini, A. D. Polosa and V. Riquer, Phys. Rev. D **89** 114010 (2014), arXiv:1405.1551 [hep-ph]  
- [88] D. Ebert, R. N. Faustov and V. O. Galkin, Phys. Lett. B **634** 214–219 (2006), arXiv:hep-ph/0512230  
- [89] Z. Wang and T. Huang, Phys. Rev. D **89** 054019 (2014), arXiv:1310.2422 [hep-ph]  
- [90] S. H. Lee, K. Morita and M. Nielsen, Phys. Rev. D **78** 076001 (2008), arXiv:0808.3168 [hep-ph]  
- [91] P. C. Wallbott, G. Eichmann and C. S. Fischer, Phys. Rev. D **102** 051501 (2020), arXiv:2003.12407 [hep-ph]  
- [92] R. Alkofer and L. von Smekal, Phys. Rept. **353** 281 (2001), arXiv:hep-ph/0007355  
- [93] C. Itzykson and J. B. Zuber, *Quantum Field Theory*. International Series In Pure and Applied Physics, New York: McGraw-Hill, 1980
- [94] M. E. Peskin and D. V. Schroeder, *Introduction to Quantum Field Theory*, 1995
- [95] V. N. Gribov, Nucl. Phys. B **139** 1 (1978) 
- [96] P. J. Silva and O. Oliveira, Nucl. Phys. B **690** 177–198 (2004), arXiv:hep-lat/0403026  
- [97] A. Sternbeck, E. M. Ilgenfritz, M. Muller-Preussker and A. Schiller, Phys. Rev. D **72** 014507 (2005), arXiv:hep-lat/0506007  
- [98] H. G. 't Hooft and M. J. G. Veltman, Nucl. Phys. B **44** 189–213 (1972) 
- [99] W. Pauli and F. Villars, Rev. Mod. Phys. **21** 434–444 (1949) 
- [100] C. S. Fischer, Prog. Part. Nucl. Phys. **105** 1–60 (2019), arXiv:1810.12938 [hep-ph]  
- [101] C. J. Burden, L. Qian, C. D. Roberts, P. C. Tandy and M. J. Thomson, Phys. Rev. C **55** 2649–2664 (1997), arXiv:nucl-th/9605027  
- [102] R. Williams, C. S. Fischer and W. Heupel, Phys. Rev. D **93** 034026 (2016), arXiv:1512.00455 [hep-ph]  
- [103] P. Maris and C. D. Roberts, Phys. Rev. C **56** 3369–3383 (1997), arXiv:nucl-th/9708029  
- [104] P. Maris and P. C. Tandy, Phys. Rev. C **60** 055214 (1999), arXiv:nucl-th/9905056  
- [105] R. Alkofer, C. S. Fischer and F. J. Llanes-Estrada, Phys. Lett. B **611** 279–288 (2005), arXiv:hep-th/0412330  
- [106] P. A. Zyla and others, PTEP **2020** 083C01 (2020)  
- [107] L. Chang and C. D. Roberts, Phys. Rev. Lett. **103** 081601 (2009), arXiv:0903.5461 [nucl-th]  

- [108] A. Windisch, M. Q. Huber and R. Alkofer, *Acta Phys. Polon. Supp.* **6** 887–892 (2013), arXiv:1304.3642 [hep-ph]  
- [109] C. S. Fischer, D. Nickel and R. Williams, *Eur. Phys. J. C* **60** 47–61 (2009), arXiv:0807.3486 [hep-ph]  
- [110] A. Krassnigg, *PoS CONFINEMENT8* 075 (2008), arXiv:0812.3073 [nucl-th]  
- [111] E. E. Salpeter and H. A. Bethe, *Phys. Rev.* **84** 1232–1242 (1951) 
- [112] G. Eichmann, *QCD and hadron physics*, Lecture notes, <http://cftp.ist.utl.pt/gernot.eichmann/lecture-notes> (state: 19.07.2021)
- [113] K. Huang and H. A. Weldon, *Phys. Rev. D* **11** 257 (1975) 
- [114] R. E. Cutkosky and M. Leon, *Phys. Rev.* **135** B1445 (1964) 
- [115] N. Nakanishi, *Phys. Rev.* **138** B1182–B1192 (1965) 
- [116] R. Williams, *EPJ Web Conf.* **3** 03005 (2010), arXiv:0912.3494 [hep-ph]  
- [117] M. Gell-Mann, R. J. Oakes and B. Renner, *Phys. Rev.* **175** 2195 (1968) 
- [118] G. Eichmann: *Hadron properties from QCD bound-state equations*, PhD thesis, (2009), arXiv:0909.0703 [hep-ph] 
- [119] L. D. Faddeev, *Sov. Phys. Dokl.* **6** 384–186 (1961)
- [120] W. Heupel, G. Eichmann and C. S. Fischer, *Phys. Lett. B* **718** 545–549 (2012), arXiv:1206.5129 [hep-ph]  
- [121] N. Ishii, W. Bentz and K. Yazaki, *Nucl. Phys. A* **587** 617–656 (1995) 
- [122] A. Windisch, *Phys. Rev. C* **95** 045204 (2017), arXiv:1612.06002 [hep-ph]  
- [123] S. M. Dorkin, L. P. Kaptari, T. Hilger and B. Kampfer, *Phys. Rev. C* **89** 034005 (2014), arXiv:1312.2721 [hep-ph]  
- [124] C. S. Fischer, S. Kubrak and R. Williams, *Eur. Phys. J. A* **51** 10 (2015), arXiv:1409.5076 [hep-ph]  
- [125] L. Schlessinger, *Phys. Rev.* **167** 1411 (1968) 
- [126] W. Heupel: *Tetraquark bound states in a Bethe-Salpeter approach*, MSc thesis (2011) 
- [127] A. M. Khvedelidze and A. N. Kvinikhidze, *Theor. Math. Phys.* **90** 62–74 (1992) 
- [128] G. Eichmann, C. S. Fischer and H. Sanchis-Alepuz, *Phys. Rev. D* **94** 094033 (2016), arXiv:1607.05748 [hep-ph]  
- [129] G. Eichmann, C. S. Fischer, W. Heupel, N. Santowsky and P. C. Wallbott, *Few Body Syst.* **61** 38 (2020), arXiv:2008.10240 [hep-ph]  
- [130] S. Yokojima, M. Komachiya and R. Fukuda, *Nuclear Physics B* **390** 319–352 (1993) 
- [131] B. Blankleider and A. N. Kvinikhidze, arXiv:2102.05818 [hep-ph] 

- [132] N. Santowsky, G. Eichmann, C. S. Fischer, P. C. Wallbott and R. Williams, arXiv:2103.14673 [hep-ph] 
- [133] A. N. Kvinikhidze and B. Blankleider, arXiv:2102.09558 [hep-th] 
- [134] A. N. Kvinikhidze and B. Blankleider, Phys. Rev. D **90** 045042 (2014), arXiv:1406.5599 [hep-ph]  
- [135] Ref. [106], chapter “Resonances”, 675–681.
- [136] A. V. Manohar and M. B. Wise, Nucl. Phys. B **399** 17–33 (1993), arXiv:hep-ph/9212236  
- [137] R. Garcia-Martin, R. Kaminski, J. R. Pelaez and d. E. J. Ruiz, Phys. Rev. Lett. **107** 072001 (2011), arXiv:1107.1635 [hep-ph]  
- [138] N. Santowsky, G. Eichmann, C. S. Fischer, P. C. Wallbott and R. Williams, Phys. Rev. D **102**, 056014 (2020), arXiv:2007.06495 [hep-ph]  
- [139] M. Wakayama, T. Kunihiro, S. Muroya, A. Nakamura, C. Nonaka, M. Sekiguchi and H. Wada, Phys. Rev. D **91** 094508 (2015), arXiv:1412.3909 [hep-lat]  
- [140] R. A. Briceno, J. J. Dudek, R. G. Edwards and D. J. Wilson, Phys. Rev. Lett. **118** 022002 (2017), arXiv:1607.05900 [hep-ph]  
- [141] R. A. Briceno, J. J. Dudek, R. G. Edwards and D. J. Wilson, Phys. Rev. D **97** 054513 (2018), arXiv:1708.06667 [hep-lat]  
- [142] J. T. Londergan, J. Nebreda, J. R. Pelaez and A. Szczepaniak, Phys. Lett. B **729** 9–14 (2014), arXiv:1311.7552 [hep-ph]  
- [143] H. G. 't Hooft, G. Isidori, L. Maiani, A. D. Polosa and V. Riquer, Phys. Lett. B **662** 424–430 (2008), arXiv:0801.2288 [hep-ph]  
- [144] D. Ebert, R. N. Faustov and V. O. Galkin, Eur. Phys. J. C **60** 273–278 (2009), arXiv:0812.2116 [hep-ph]  
- [145] S. Okubo, Phys. Lett. **5** 165–168 (1963) 
- [146] G. Zweig, *An SU(3) model for strong interaction symmetry and its breaking. Version 2*, 1964, published in Published in: Developments in the Quark Theory of Hadrons, Volume 1, 
- [147] J. Iizuka, Prog. Theor. Phys. Suppl. **37** 21–34 (1966) 
- [148] R. N. Faustov, V. O. Galkin and E. M. Savchenko, Phys. Rev. D **102** 114030 (2020), arXiv:2009.13237 [hep-ph]  
- [149] J. F. Giron and R. F. Lebed, Phys. Rev. D **102** 074003 (2020), arXiv:2008.01631 [hep-ph]  
- [150] J. Zhao, S. Shi and P. Zhuang, Phys. Rev. D **102** 114001 (2020), arXiv:2009.10319 [hep-ph]  
- [151] R. N. Faustov, V. O. Galkin and E. M. Savchenko, Universe **7** 94 (2021), arXiv:2103.01763 [hep-ph]  

- [152] C. Deng, H. Chen and J. Ping, Phys. Rev. D **103** 014001 (2021), arXiv:2003.05154 [hep-ph]  
- [153] G. Yang, J. Ping and J. Segovia, Phys. Rev. D **104** 014006 (2021), arXiv:2104.08814 [hep-ph]  
- [154] H. Sanchis-Alepuz and R. Williams, Comput. Phys. Commun. **232** 1–21 (2018), arXiv:1710.04903 [hep-ph]  
- [155] G. C. Wick, Phys. Rev. **96** 1124–1134 (1954) 
- [156] J. Vermaseren, (2000), arXiv:math-ph/0010025 
- [157] V. Shtabovenko, R. Mertig and F. Orellana, Comput. Phys. Commun. **207** 432–444 (2016), arXiv:1601.01167 [hep-ph]  
- [158] R. Mertig, M. Böhm, and A. Denner, Comput. Phys. Commun., 64, 345–359, 1991.
- [159] G. Bärwolff, *Numerik für Ingenieure, Physiker und Informatiker* (Springer Berlin Heidelberg, Berlin, Heidelberg, 2016) 
- [160] *Gaussian quadrature*, Wikipedia, https://en.wikipedia.org/wiki/Gaussian_quadrature (state: 25.07.2021)
- [161] W. H. Press, S. A. Teukolsky, W. T. Vetterling and B. P. Flannery, *Numerical Recipes in C*, Cambridge University Press, 
- [162] G. Guennebaud, B. Jacob and others, *Eigen v3*, 2010, <http://eigen.tuxfamily.org>  (state: 02.07.2021)
- [163] D. H. House, *Spline Curves*, <https://people.cs.clemson.edu/~dhouse/courses/405/notes/splines.pdf>  (state: 02.07.2021)
- [164] R. Tripolt, P. Gubler, M. Ulybyshev and L. von Smekal, Comput. Phys. Commun. **237** 129–142 (2019), arXiv:1801.10348 [hep-ph]  
- [165] GCC, the GNU Compiler Collection, <https://gcc.gnu.org> (state: 25.07.2021)
- [166] G. Van Rossum and F. L. Drake, *Python 3 Reference Manual*, CreateSpace, Scotts Valley, CA, 2009 
- [167] Wolfram Research, Inc., *Mathematica, Version 12.3.1*, Champaign, IL, 2021, <https://www.wolfram.com/mathematica> (state: 25.07.2021)
- [168] T. Williams, C. Kelley and many others, *Gnuplot 5.4: an interactive plotting program*, 2021, <http://gnuplot.sourceforge.net/> (state: 25.07.2021)
- [169] Inkscape Project, *Inkscape 0.92.5*, 2020, <https://inkscape.org> (state: 25.07.2021)
- [170] Adobe Inc., *Adobe Illustrator CC 2021*, <https://adobe.com/products/illustrator> (state: 25.07.2021)
- [171] L. Lamport, *LATEX: A Document Preparation System*, Addison, Wesley Publishing Co., Reading, Ma, 1986
- [172] *TeX Live*, <https://tug.org/texlive/> (state: 25.07.2021)

Acknowledgements / Danksagungen

First, I want to express my deep gratitude to my supervisor Prof. Dr. Christian Fischer who gave me the chance to work on this hot topic and who was always a patient and helpful contact person in various regards. Besides that, I thank Prof. Dr. Marc Wagner for being my second referee. Furthermore, I want to thank Dr. Richard Williams and Dr. Gernot Eichmann who provided competent support and guidance whenever it was required. Additional, many thanks go out to my colleagues at the institute – in particular Dr. Esther Weil, with whom I shared an office for most of the time – who were not only subject-specific partners, but also brought unforgettable and irreplaceable memories.

I thank the Helmholtz Graduate School for Hadron and Ion Research (HGS-HIRe) for providing access to helpful courses and for financial support during my time as a participant, and at this point, I also thank Prof. Dr. Sören Lange for being my associated, second supervisor. For supporting me with a stipend for 31 months, I want to give special thanks to the GSI Helmholtzzentrum für Schwerionenforschung.

Moreover, I want to thank my family and friends, in particular my parents, for providing further emotional support, and last but not least, profuse thanks go out to my fiancée Nina, who went through the most stressful phases and moments with me and was always the most reliable constant. It's the most valuable present to have you by my side.

Eigenständigkeitserklärung

Ich erkläre: Ich habe die vorgelegte Dissertation selbstständig und ohne unerlaubte fremde Hilfe und nur mit den Hilfen angefertigt, die ich in der Dissertation angegeben habe. Alle Textstellen, die wörtlich oder sinngemäß aus veröffentlichten Schriften entnommen sind, und alle Angaben, die auf mündlichen Auskünften beruhen, sind als solche kenntlich gemacht. Ich stimme einer evtl. Überprüfung meiner Dissertation durch eine Antiplagiat-Software zu. Bei den von mir durchgeführten und in der Dissertation erwähnten Untersuchungen habe ich die Grundsätze guter wissenschaftlicher Praxis, wie sie in der "Satzung der Justus-Liebig-Universität Gießen zur Sicherung guter wissenschaftlicher Praxis" niedergelegt sind, eingehalten.

Ort, Datum

Unterschrift (Nico Santowsky)